EXPERIMENTAL STUDY OF DENSITY FLUCTUATIONS IN THE STOR-M TOKAMAK BY SMALL-ANGLE MICROWAVE SCATTERING

A Thesis Submitted to the College of
Graduate Studies and Research
In Partial Fulfillment of the Requirements
For the Degree of Master of Science
In the
Department of Physics and Engineering Physics
University of Saskatchewan
Saskatoon

By
Stephen Jason Livingstone
Saskatoon, Saskatchewan
Canada

In presenting this thesis in partial fulfilment of the requirements for a Postgraduate degree from the University of Saskatchewan, I agree that the Libraries of this University may make it freely available for inspection. I further agree that permission for copying of this thesis in any manner, in whole or in part, for scholarly purposes may be granted by the professor or professors who supervised my thesis work or, in their absence, by the Head of the Department or the Dean of the College in which my thesis work was done. It is understood that any copying or publication or use of this thesis or parts thereof for financial gain shall not be allowed without my written permission. It is also understood that due recognition shall be given to me and to the University of Saskatchewan in any scholarly use which may be made of any material in my thesis.

Requests for permission to copy or to make other use of material in this thesis in whole or part should be addressed to:

Head of the Department of Physics and Engineering Physics
116 Science Place
University of Saskatchewan
Saskatoon, Saskatchewan
Canada
S7N 5E2

Dedicated to
Kate and Dad

Abstract

Density fluctuations in high temperature fusion plasmas have been a central challenge to the development of fusion power. They are the cause of excessive anomalous losses from the plasma and are still not fully understood. A microwave scattering experiment is performed on the Saskatchewan Torus-Modified (STOR-M) tokamak for the first time to study these density fluctuations with wave-numbers in the range $\left|\vec{k}\right|$ = 5 /cm to 10 /cm. The fluctuations are found to follow $k_\perp \rho_s$ scaling consistent with ion drift waves; signatures of the electron temperature gradient (ETG) mode connected with anomalous electron losses are not detected. The fluctuation level in the STOR-M is measured to be $\tilde{n}/n \approx 0.1$ at a mean perpendicular wave-number of $k_\perp \approx 7$ /cm and is reported for the first time. The fluctuation levels are inversely proportional to the energy confinement time suggesting that these fluctuations are driving anomalous particle and energy losses from the STOR-M. The system is now fully operational and this work paves the way for future experiments with this equipment.

Acknowledgments

I would like to express thanks and gratitude to a number of people and in particular my supervisor Prof. A. Hirose for enabling this work to become a success. I am also indebted to Dr. A. Singh for his invaluable expertise and cooperation in many technical aspects of this work. I would also like to thank Prof. C. Xiao for many insightful discussions and comments. A special note of thanks is made to Prof C.M. Surko for telephoning from the USA with assistance about a classic 30 year old scattering paper. Also, Dr. G. Conway's initial work and technical assistance was greatly appreciated.

Technical assistance was provided by Dave McColl, Perry Balon and Blair Chomyshen as required. Help was also graciously received from fellow graduate students Dazhi Lu and Geoffrey St. Germaine whenever needed.

This work was supported by funds from the Natural Sciences and Engineering Research Council of Canada and through financial aid from the University of Saskatchewan and the Naval Reserves of Canada.

Contents

List of Tables

List of Figures

Glossary of Abbreviations and Terms

STOR-M	Saskatchewan Torus-Modified
GOLA	Gaussian Optic Lens Antenna
ETG	Electron Temperature Gradient
ITG	Ion Temperature Gradient
FWHM	Full Width at Half Maximum
GUI	Graphical User Interface
CT	Compact Torus
MHD	Magnetohydrodynamics
FLR	Finite Larmor Radius
H-Mode	Improved confinement discharge
L-Mode	Normal discharge
TE	Transverse Electric mode
FEMLAB	Finite Element Modeling Laboratory computer software
MATLAB	MATrix LABoratory computer software for data processing
k_B	Boltzmann constant
ε_0, μ_0	Permittivity and permeability of free space
$\vec{k}$	Scattering wavevector
$k_\perp$	Perpendicular scattering wave number
$\vec{k}_r, \vec{k}_\theta$	Radial and poloidal wavevectors
ω	Frequency
$S(\vec{k}, \omega)$	Spectral density function
$a,\ R_0$	Minor and major radii
r, R	Minor and major radial coordinates
ε	Inverse aspect ratio ($\varepsilon = r / R_0$)
B_t	Toroidal magnetic field
I_p	Plasma current
$n_{\mathrm{i,e}}$	Plasma density of ions and electrons
$\tilde{n}_{i,e}$	Plasma density fluctuations

$m_{e,i}$	Electron and ion mass
e	Elementary charge
$T_{i,e}$	Ion and electron temperature
ω_{cj}	Cyclotron frequency, j is i for ions and e for electrons
ω_{pj}	Plasma frequency for species j
V_l	Loop voltage
τ_e	Energy confinement time
$\rho_{i,e}$	Ion/electron Larmor radius
ρ_s	Ion Larmor radius with electron temperature
χ_e	Electron thermal diffusivity
c	Speed of light in a vacuum
η_c	Neo-classical resistivity

Chapter 1

Introduction

1.1 Overview of Fusion Research

The elusive goal of research into thermonuclear fusion is to produce commercially viable sustainable energy. The realization of this goal requires that, in a laboratory environment, the reactions that power the stars are recreated. However, the massive gravitational forces present in a star cannot be recreated in a controlled manner on earth. Therefore one has to find a suitable technique to confine a much higher temperature plasma at lower pressures in order to create conditions suitable for fusion reactions. The most promising technology to date is confinement of a plasma by strong magnetic fields in a device known as a tokamak.

This concept was first proposed by the Russian scientists Sakharov and Tamm during the Cold War in the 1950's [1]. The work was originally kept highly classified as some believed the neutrons produced from a fusion reactor could be used to breed weapons grade plutonium. However, due to the low neutron flux and limited success with early experiments [2], power production became the main goal of fusion research. This was further emphasized during the Geneva conference of 1958 when all fusion related work was officially declassified.

In order to achieve a successful fusion reaction, light positively charged nuclei must be brought together with sufficient energy (on the order of 10 keV $\approx$ 100 million ^{o}C) to overcome columbic forces between them in order to successfully 'fuse' and form new particles and release energy. There are numerous possible fusion reactions, each with

their own advantages and disadvantages for fusion power production. One important property of these reactions is the cross-section σ (essentially the probability of the reaction occurring for specified conditions, it has units of area and represents the collision cross-section required for a reaction to occur), which can be averaged over a Maxwellian velocity distribution to calculate the average reaction rate for specified conditions

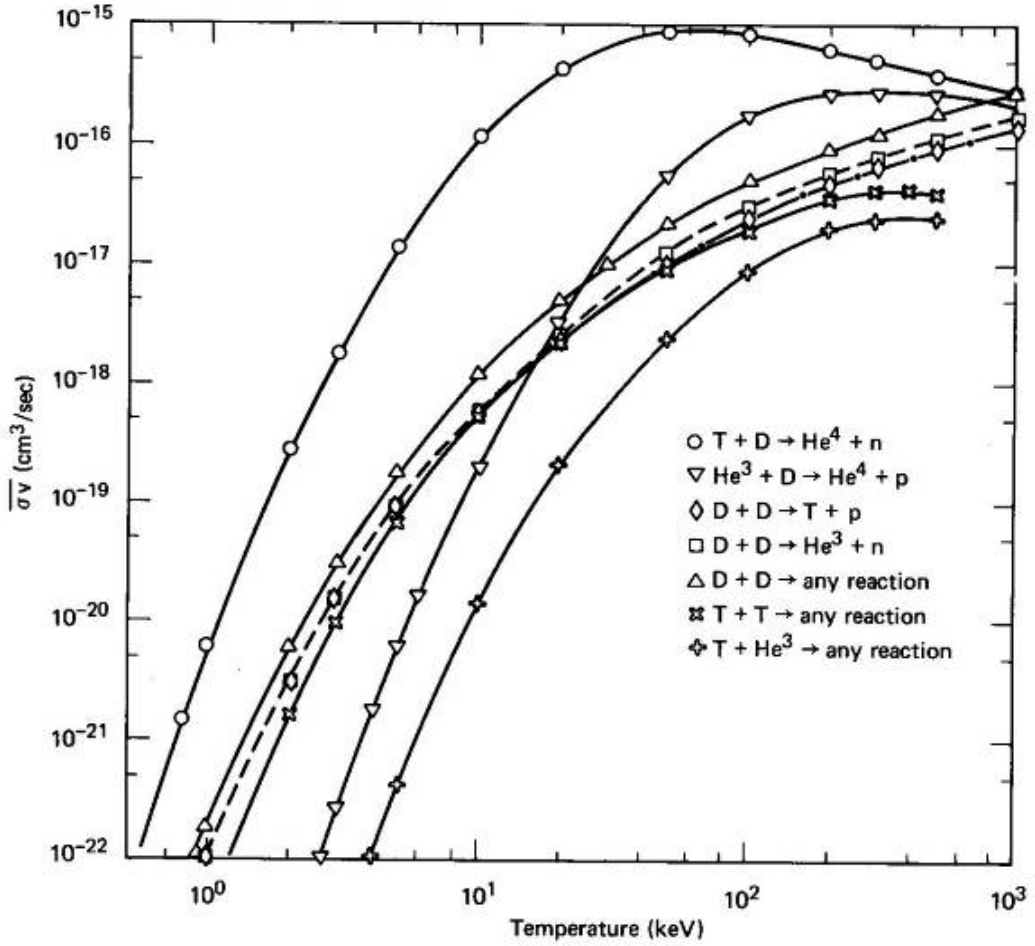

Figure 1-1: Maxwell averaged cross sections for several fusion reactions [E.Teller, *Fusion: Magnetic Confinement* (Academic Press, 1981)]

From Figure 1-1 it is clear that the following reaction has the largest reaction rate in all operating regimes

$$\text{Tritium (T)} + \text{Deuterium (D)} \rightarrow \text{He}^4\ (3.5\ \text{MeV}) + \text{neutron (14 MeV)}$$

where tritium is a hydrogen isotope with 2 neutrons and deuterium is hydrogen with 1 neutron. Other advantages of this reaction are its relatively high energy output, and it produces only singly charged nuclei and hence bremsstrahlung losses are minimized. Although deuterium is a naturally occurring substance, tritium (with a half-life of 12 years) must be bred if it is to be used as a fuel source. One technique is to wrap the D-T reaction with a lithium blanket (7.42% Li^6 and 92.58% Li^7) and use neutrons to breed tritium [3]:

$$Li^6 + n \rightarrow T + He^4 + 4.7\ MeV$$
$$Li^7 + n \rightarrow T + He^4 + n - 2.6\ MeV$$

As the initial D-T reaction produces a neutron with 14 MeV, both reactions are possible. With this technique, the production of the tritium fuel also generates heat which can be extracted and used to power turbines for electricity production through conventional means.

For a fusion power plant to be successful, there are several important criteria that must be met. The ultimate goal is to attain sustained power, which requires that a reactor must achieve ignition, this means that α-particle heating becomes sufficient to maintain the high fuel temperature without external heating (in analogy to a conventional fossil fuel plant). This requires sufficient temperature to overcome columbic forces coupled with a relatively high density for an adequate reaction rate and a high energy confinement time (τ_e = Plasma energy / Rate of energy loss). These characteristics must satisfy the following criterion:

$$\hat{n}\hat{T}\tau_e > 5\times10^{21}\,\mathrm{m^{-3}keV\,s} \qquad \textbf{1-1}$$

where $\hat{n}$ is the peak density and $\hat{T}$ is the peak temperature [3]. Relation 1-1 is a modified version of the Lawson criterion [4] taking into account α-particle heating and neglecting hydrogen bremsstrahlung radiation. Reactor performance has been progressing towards this level, as shown in Figure 1-2.

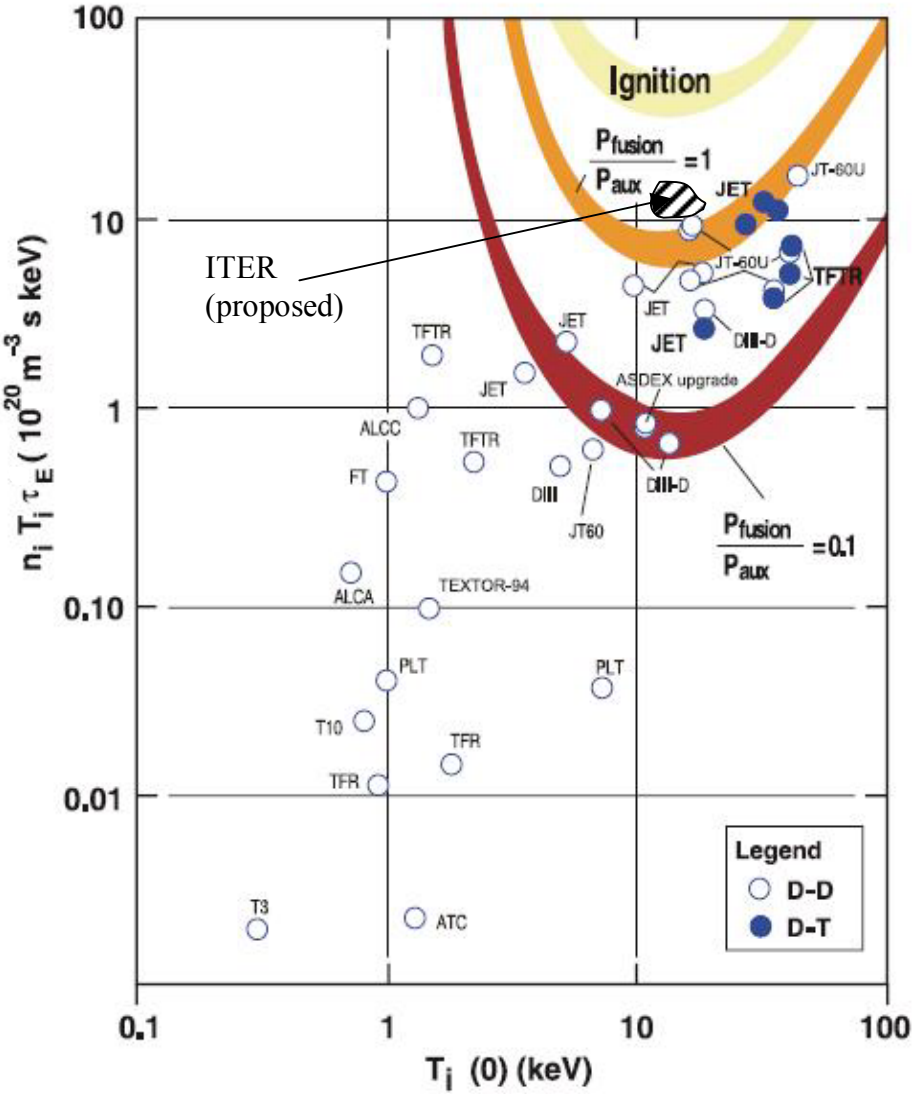

Figure 1-2: Fusion reactor progress; each successive machine moves closer to ignition conditions. Figure taken from [5] with ITER data from [11] added. Acronyms refer to specific tokamak devices.

Fusion reactor progress has been slow but successful, with each successive machine moving closer to ignition conditions. There are numerous small to medium size tokamaks in service today, and currently two large operating devices: JET (Joint European Torus) [6] and JT-60U (Japanese Tokamak Upgrade) [7]. In 1991 JET performed the first plasma discharge with tritium [8] producing an estimated 1.7 MW of fusion power with $Q \approx 0.15$ (Q is the ratio of fusion power output to auxiliary input heating power). JET

has also demonstrated the possibility of alpha particle heating of a plasma [9]. The JT-60U currently holds the world record Q-value at 1.25 set in 1998 [10].

The next large scale experiment is the ITER [11] project (meaning 'the way' in Latin). ITER is a multinational collaboration that aims to be the first fusion device to produce energy at the level of an electricity-producing power plant. The goal of ITER is to achieve $Q \approx 10$ with power production of 500 MW. Ignition is not possible with ITER and approximately 50 MW of heating power will be required. ITER is to be built in Cadarache France, with the first plasma expected in 2016.

Although this brief overview of fusion power looks promising, effective confinement of the high temperature plasma is exceedingly difficult. Abundant instabilities and turbulence make plasma confinement challenging, and typically confinement times are much shorter then expected. This observation has been confirmed by numerous experiments over decades of research that have indicated the existence of strong anomalous losses within the plasmas that greatly exceed, by varying orders of magnitude, those indicated by neo-classical theory based on columbic scattering. These anomalous losses and other technological challenges have prevented, until recently, the construction of a fusion reactor capable of producing commercially viable energy.

A full understanding of anomalous transport in fusion plasma research has still not been achieved. Many explanations of this phenomenon describe turbulence and micro-instabilities as the mechanism for this unexplained transport [12]. Modern experiments in advanced tokamaks have been able to suppress ion thermal diffusivity to the order predicated by neo-classical theory [13], however, anomalous electron diffusivity remains a problem.

One possible candidate for the unexplained high electron thermal diffusivity (χ_e) present in high temperature plasmas is the Electron Temperature Gradient (ETG) mode. This is a short wavelength, high frequency, turbulent instability believed to be capable of driving the anomalous electron losses observed in modern high temperature plasma devices.

Recent work predicts this mode to maximize on a scale length similar to the skin depth (c/ω_{pe}) of the plasma [14] [15], where $\omega_{pe} = \left(\frac{n_e e^2}{\varepsilon_0 m_e} \right)^{\frac{1}{2}}$ is the usual plasma frequency and c is the speed of light in a vacuum. One possible method to examine fluctuations in this regime is a scattering experiment, by which an incident electromagnetic wave is scattered by the plasma. Scattering experiments have always been a crucial diagnostic tool in high temperature plasma [16] as they allow probing of the hot dense plasma core without disturbing the plasma. Unlike some diagnostics, scattering does not require the placement of objects in the plasma, nor does it perturb the plasma.

The scattering system used in this study is capable of measuring fluctuations of the order of the skin depth; however, by coincidence in the STOR-M the skin depth is approximately equal to the ion Larmor radius with electron temperature: $\rho_s = \frac{1}{\omega_{ci}} \sqrt{\frac{T_e}{m_i}}$ where ω_{ci} is the ion cyclotron frequency. ρ_s is a mathematical construct and is the typical scale length for ion drift-waves and is approximately ~ 0.2 cm in the STOR-M. This means that the ETG and ion drift-wave modes maximize in the same region in the STOR-M, just outside the maximum range ($\left|\vec{k}\right| \approx 5 - 20$ /cm) of the scattering system.

In order to probe fluctuations in the STOR-M plasma of the order of the skin depth and modified ion Larmor radius ($\omega_{pe}/c \approx 1/\rho_s \approx 5$ /cm) a 13 W 140 GHz klystron source is employed. This allows density fluctuations to be studied in the range: $\left|\vec{k}\right| \approx 5 - 20$ /cm (limited by physical accessibility to the plasma) which is sufficient to cover the expected unstable range of the ETG or ion drift modes. Scattering in this frequency has been done before [17], but with a low power source (0.5 W) to study excited drift-wave-like modes. In order to examine the smaller ETG fluctuations a 13 W source is used in this experiment. This allows the measurement of very small scale density fluctuations $\tilde{n}/n \approx 10^{-4}$ in the centre of the plasma.

1.2 Tokamak Configuration

The word 'tokamak' is derived from the Russian words: "***tor***oidalnaya ***ka***mera" (toroidal chamber) and "***ma***gnitnaya ***k***atushka" (magnetic coil) and was invented by Russian scientists in the 1950's [1]. It is a toroidal (doughnut) shaped device with a strong toroidal magnetic confinement field. A generic ohmic heated tokamak is sketched in Figure 1-3.

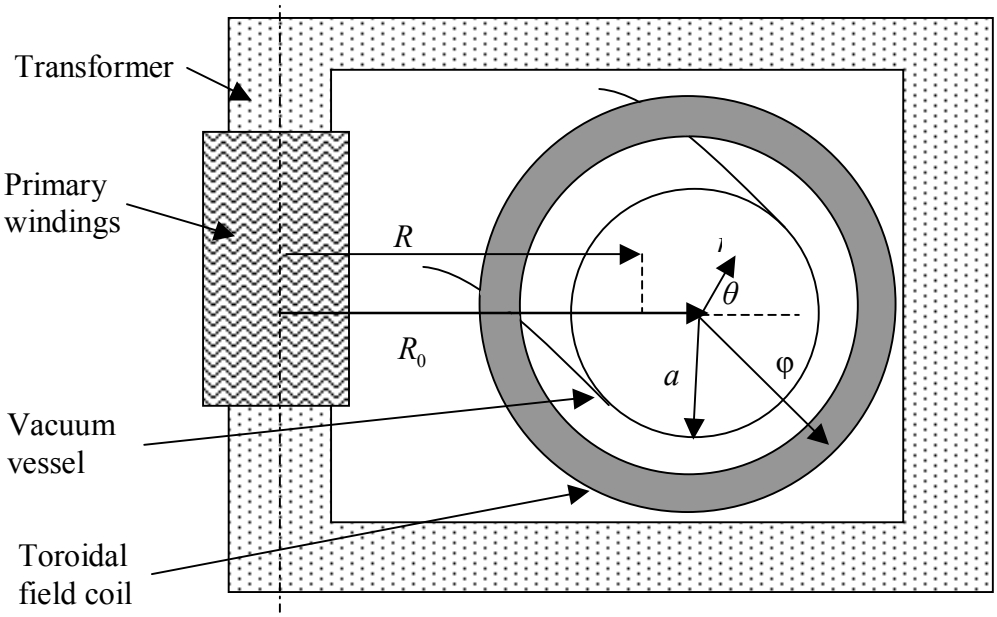

Figure 1-3: Simplified diagram of a generic ohmic heated tokamak. The plasma is maintained within the vacuum vessel.

In Figure 1-3, R_0 is the major radius, a is the minor radius, R is the major radius coordinate, r is the minor radius coordinate, φ is the toroidal coordinate and θ is the poloidal angle. The vacuum vessel circles completely around the primary windings in the shape of a torus. There are usually several toroidal field coils spaced evenly around the chamber and are used to generate the strong confining toroidal field (1-5 Tesla). The strong magnetic field is primarily used for plasma confinement as the charged particles will gyrate around this field. The primary windings and the transformer core are used to inductively drive a large current through the plasma along the toroidal direction to provide ohmic resistive heating, and additional poloidal magnetic fields along the θ direction (modern tokamaks have to rely on alternative heating schemes as the plasma

resistivity (η_c) becomes too low at higher temperatures: $\eta_c \propto \frac{1}{T_e^{3/2}}$, see Section 2.2.3). The combined toroidal and poloidal fields result in helical magnetic field lines.

1.3 Thesis goals and objectives

The main goals and objectives of this work are summarized below:

1) Bring the scattering system online, testing and characterizing all the necessary components, modifying and repairing the system as necessary.
2) Perform the first scattering experiment in the STOR-M tokamak and the first high power scattering experiment in a small tokamak.
3) Analyze the results looking for evidence of drift-waves and signatures of the elusive ETG mode. Fluctuation data can also be used to determine optimum operating regimes for the STOR-M.
4) Consider possible future experiments and upgrades to the existing scattering system.

1.4 Thesis outline

Having presented a brief overview of fusion progress, anomalous losses and the basic tokamak configuration, a detailed discussion of the subject matter can now be presented.

- Chapter 2 describes the STOR-M tokamak including diagnostics and specific modifications made for this experiment.

- Chapter 3 deals with the various theoretical aspects of this work and also reviews previous experimental results. 3.2 Briefly describes electromagnetic wave propagation in a magnetized plasma, Section 3.3 includes a complete derivation of the homodyne scattering theory used in this experiment. 3.4 introduces specific tokamak plasma physics. Section 3.5 portrays a simple fluid drift-wave theory and Section 3.6 shows the formulism for ETG modes from full kinetic theory.

- Chapter 4 explains the experimental apparatus used, 4.1 describes the system as a whole and demonstrates the custom Matlab™ GUI implemented to determine scattering geometries. 4.2 details the initial testing and characterization of the system, including interferometer results and initial MHD contamination. 4.3 discusses the design, construction and testing of low noise amplifiers.

- Chapter 5 presents the data analysis. Section 5.1 connects the raw data measured with physical quantities desired. 5.2 states the operating regimes used and 5.3 describes the data pipeline and techniques required to process the data.

- Chapter 6 presents the various relevant results. 6.1 discusses the density fluctuation levels compared to theory and previous independent experiments. 6.2 discusses the frequency spectra. 6.3 examines the spectral density function in the low k regime (5 - 10 /cm) and shows that the data qualitatively follows $k\rho_s$ normalization as predicted by drift-wave theory. Skin depth normalization of the ETG mode is not detected. 6.4 describes the inverse relationship between fluctuation level and energy confinement time and 6.5 discusses optimal STOR-M operating regimes.

- Chapter 7 summarizes the work and presents suggestions for future work, including H-mode operation, CT injection studies and improvements to the scattering system.

Chapter 2

Saskatchewan Torus-Modified (STOR-M)

2.1 STOR-M Overview

The Saskatchewan Torus-Modified (STOR-M) tokamak was completed in 1987 [18] and has been involved in numerous experiments: turbulent heating [19], AC operation [20], plasma biasing [21] and recently Langmuir probe experiments [22] and vertical Compact Torus (CT) injection [23]. The main characteristic parameters are: Major radius R = 0.46 m, minor radius a = 0.13 m, plasma current $I_p \approx$ 20-30 kA, density $n \approx 5\times10^{18}/\text{m}^3$, pulse duration ≈ 50 ms, electron temperature ≈ 200 eV, ion temperature ≈ 70 eV (approximated from the Artsimovich scaling law [24]), loop voltage $V_l \approx 3$ V and toroidal field $B_t \approx 0.7$ T. A 3D CAD model of the STOR-M is shown in Figure 2-1.

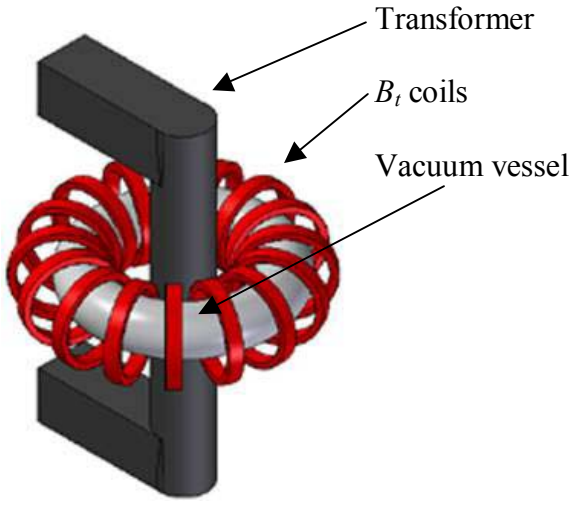

The 16 B_t coils are composed of 9 turns each and can generate up to a 1 Tesla field. The primary windings are located in two pairs above and below the vacuum chamber.

Figure 2-1: STOR-M 3D CAD model drawn to scale. The vacuum vessel has a major radius of 0.46 m to the centre of its circular cross-section.

The vacuum chamber is evacuated by a large turbomolecular pump (approx. 1000 L/s) backed by a rotary pump down to a base pressure of typically 1×10^{-7} Torr. The system is then filled to a pressure of 1.8-2.2$\times10^{-4}$ Torr using ultra pure Hydrogen (99.999%), and maintained by a Veeco Automatic Pressure Controller [25]. During the discharge, density loss is supplemented by puffing H_2 gas through a high speed piezoelectric PV-10 valve (response time ≈ 2 ms).

The STOR-M under normal operating conditions can achieve a discharge every 4-5 minutes. The currents necessary to provide B_t and induce I_p are provided by charging capacitor banks, and then discharging them in a precise time sequence. Each plasma pulse (shot) requires exact timing:

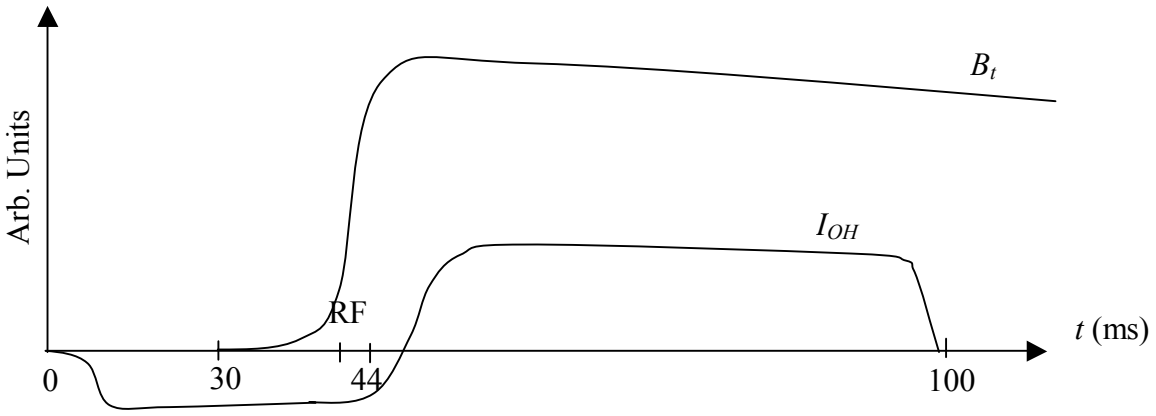

Figure 2-2: Timings used to correctly trigger a plasma discharge. Graphs indicate B_t and ohmic current (I_{OH}) waveforms.

Figure 2-2 shows the standard timings used for a STOR-M discharge. At t = 0 a small ohmic bias bank is discharged to the main transformer to magnetically saturate the core and maximize the magnetic flux available for the discharge. Next to trigger is the B_t bank (3-7 kV, 15 mF) through an ignitron delivering up to 12 kA to the toroidal field coils. At about 42 ms an RF (radiofrequency) system is triggered to assist the hot filament system in generating a low temperature RF plasma, this reduces the magnetic flux used during the current ramp-up. Then at 44 ms a 'fast' ohmic bank (200 mF at ≈ 140 V) is

discharged for current buildup, followed by a 'slow' bank (50 V, 10 F) for sustaining a clean flat plasma current profile that follows the I_{OH} profile.

2.2 STOR-M Diagnostics

STOR-M is equipped with a variety of diagnostic equipment for measuring discharge parameters:

Parameter	**Instrument**
Plasma Current (I_p), Toroidal field (B_t)	Rogowski Coils
Electron Density (n_e)	4-mm Homodyne interferometer (centre chord average), Langmuir probes (edge)
MHD Fluctuations	Mirnov coils (edge) (m = 2 and m = 3)
Loop voltage (V_l)	Pick up loop
Electron temperature (T_e)	Soft X-Ray (SXR) camera, Plasma resistivity.
Plasma position (ΔH)	Magnetic probes.

Table 2-1: List of available STOR-M diagnostics.

An important property of these diagnostics (except the Langmuir probes) is that they are completely passive and do not disturb the plasma. The Langmuir probes are kept near the edge region $r/a \approx 1$ (where a is the minor radius of the vacuum vessel) else they are destroyed by the plasma and introduce significant impurities into the vacuum chamber, resulting in disruptions and the need for cleaning discharges to slowly remove impurities.

2.2.1 Magnetic Coils

There are two types of magnetic coils on the STOR-M: Rogowski and Mirnov. A standard Rogowski coil is a solenoid curved into a torus as shown:

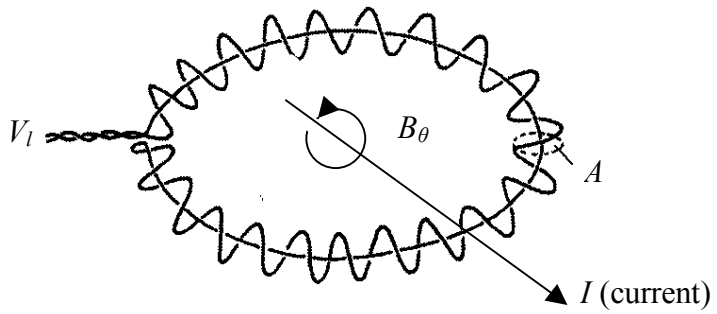

Figure 2-3: Typical Rogowski coil used for measuring current (adapted from Hutchinson [26]).

'A' is the surface area of the windings. Consider a current I passing through the centre of the coil; it generates a circular magnetic field B_θ perpendicular to the cross section A. From Faraday's law, integration around each loop of area A can be used to determine the rate of change of B_θ with respect to time:

$$\int_A \nabla \times \vec{E} \cdot d\vec{a} = \oint_A \vec{E} \cdot d\vec{l} = -\int_A \dot{\vec{B}}_\theta \cdot d\vec{a} \qquad \textbf{2-1}$$

$$V_l = -\int_A \dot{\vec{B}}_\theta \cdot d\vec{a} = -\oint_l A\dot{\vec{B}}_\theta \cdot d\vec{l} = nA\mu_0 \dot{I}_{enc} \qquad \textbf{2-2}$$

Therefore $V_l = nA\mu\,\dot{I}_{enc}$ where n is the number of turns, μ the permeability and $\dot{I}_{enc}$ is the rate of change of the current enclosed by the coil. The induced voltage (V_l) is then integrated to determine I_{enc}.

A Mirnov coil is a modified Rogowski coil with a variable winding density around the loop. This means the coil can be tailored to measure different modes of fluctuations in B_θ. This stems from the Fourier expansion of B_θ [26]

$$B_\theta(\theta) = B_0 + \sum_{m=1}^{\infty}\left(C_m \cos(m\theta) + S_m \sin(m\theta)\right) \qquad \textbf{2-3}$$

where B_0 is the unperturbed field. The periodicity in magnetic fluctuations is because the solution must be periodic around the poloidal angle θ, similarly the field is decomposed into $e^{in\varphi}$ components in the toroidal direction. The STOR-M has two sets of Mirnov coils for m = 2 and m = 3. The variable winding density is achieved by a step function

approximation by discrete uniform coils. The figures below show the sin(2θ) approximation and corresponding Fourier decomposition of the m = 2 Mirnov coil on the STOR-M:

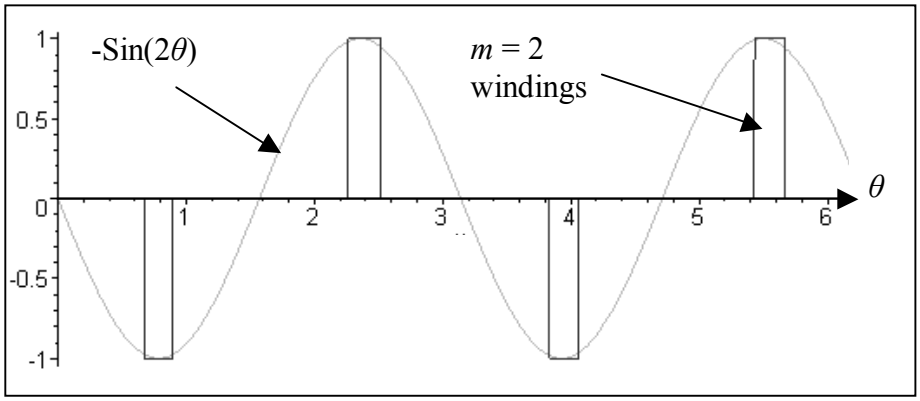

Figure 2-4: m = 2 Mirnov Coil windings are represented by the discrete rectangular winding density, a smooth fit is added for clarity.

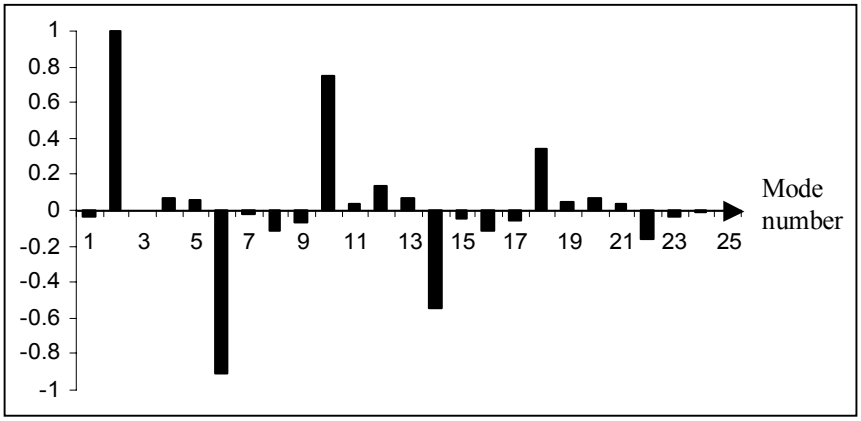

Figure 2-5: m = 2 Mirnov Coil fourier harmonics calculated from the fourier decomposition of the winding locations.

From Figure 2-5 one can see that m = 2 is the lowest high power mode, however, the m = 6 harmonic is measured with a similar power. This is not a problem as the higher order modes are much smaller components of B_θ [26]. The m = 3 coil can be described in a similar manner. On larger tokamaks it is common to surround the plasma with multiple magnetic probes (small winding sets), and then one can numerically correlate the data from each probe to generate arbitrary m number mode signals (up to $m = N/2$ where N is

the total number of probes). A 12 channel system using this technique is currently under development for the STOR-M.

2.2.2 Typical Discharge Characteristics

Typical discharge data collected from these diagnostics are shown.

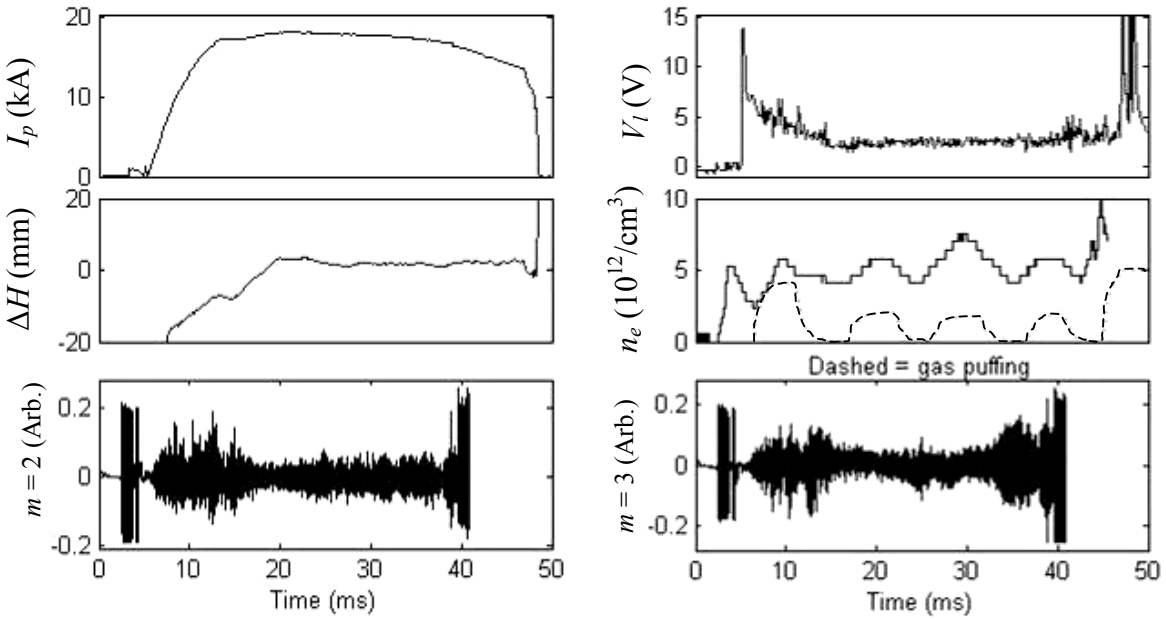

Figure 2-6: Graphs of STOR-M parameters routinely monitored for a typical discharge

The m = 2 and m = 3 magnetic fluctuation levels are shown in arbitrary units, I_p is the plasma current, ΔH is plasma position, V_l the loop voltage and the dashed line with the density (n_e) is the voltage applied to the piezoelectric gas puffing valve. ΔH represents the horizontal position of the plasma with respect to the centre of the vacuum vessel. V_l is the voltage around the torus and is induced across the plasma resulting in the plasma current (I_p). The oscillating density was the result of a poor gas valve, and hence constant density discharges were not possible during this experimental regiment. The data from the Mirnov coils are digitized by a Camac 264A module at 400 kHz, the other housekeeping data is sent to a Camac 212A module and sampled at 10 kHz. Both sets of data are then transferred by GPIB (General Purpose Interface Bus) to a single PC for storage and later analysis.

2.2.3 Temperature Calculation

The average temperature can be calculated from resistive heating using the neoclassical resistivity [28]:

$$\eta_c \approx \left(\frac{Z_{eff}\pi e^2 \sqrt{m_e}}{\left(4\pi\varepsilon_0\right)^2 \left(k_B T_e\right)^{3/2}} \ln\Lambda \right)_{sp} \frac{1}{\left(1-\sqrt{\varepsilon}\right)^2} \approx 5.8\times10^{-3} \frac{1}{T_e^{3/2}\left(\mathrm{eV}\right)} \qquad \textbf{2-4 (Neoclassical Resistivity)}$$

$$\Lambda = 12\pi n_e \left(\frac{\varepsilon_0 k_B T_e}{n_e e^2} \right)^{3/2} \qquad \textbf{2-5}$$

where $\varepsilon = r/R_0$ is the inverse aspect ratio, $Z_{\mathrm{eff}} \approx 1.5$ is the effective ion charge number (accounting for impurity ion concentrations expected in the STOR-M plasma), 'sp' refers to the classical Spitzer resistivity [27] based on Coulomb collisions, and the Coulomb logarithm ($\ln\Lambda$) accounts for the multiple small angle collisions and Debye shielding. As $\ln\Lambda$ is relatively insensitive to plasma temperature and density, it can be approximated as 17 ($n_e \approx 5\times10^{18}$ /m^3, $T_e \approx 200$ eV) to simplify the equation. The term involving the inverse aspect ratio (ε) is included to account for trapped electrons [28] which do not carry a current and therefore reduce the conductivity. In the STOR-M plasma, $\eta_c \approx 2\times10^{-6}$ Ω.m similar to that of the alloy Nichrome (common toaster heater wire).

The approximate temperature can be calculated assuming a simple solid plasma profile of resistance $\eta_c \times$(length of plasma column) / (cross-sectional area of plasma column) being heated by the current I_p

$$T_e\left(\mathrm{eV}\right) \approx \left(\frac{0.0116\, I_p R}{V_l a^2} \right)^{2/3} \qquad \textbf{2-6 (STOR-M Temperature)}$$

where R and a are the major and minor radii. For typical STOR-M parameters ($I_p \approx 25$ kA, $V_l \approx 3$ V) the temperature is approximately 190 eV. Although this is a crude approximation, absolute temperature measurements are not required for this experiment, only relative measurements; therefore Eq 2-6 is sufficient. Also, from Equation 2-4 one can see that $\eta_c \propto \frac{1}{T_e^{3/2}}$ and therefore resistive heating is not efficient at very high plasma temperatures.

2.2.4 Confinement Time

The rate of energy loss (P_L) from a high temperature plasma is characterized by $P_L = W/\tau_e$ where W is the thermal energy and τ_e is the energy confinement time. The particles in the plasma with temperature T have an average energy of 3/2 k_BT , ½ k_BT from each degree of freedom. Therefore the volume average is given by $3nk_BT$ (assuming $T_i \approx T_e$). In the STOR-M no fusion energy is produced, and therefore P_L must be maintained by the external source P_{OH} (ohmic heating), hence τ_e can be defined as W/P_{OH} and can be determined from experimental measurements:

$$\tau_e = \frac{W}{P_{OH}} = \frac{6nk_BT\pi^2Ra^2}{I_pV_l} \qquad \textbf{2-7 (Confinement Time)}$$

For a typical discharge ($I_p \approx 25$ kA, $V_l \approx 3$ V, $T \approx 190$ eV, $n \approx 5\text{x}10^{18}$ /m^3), $\tau \approx 1$ ms.

2.2.5 Interferometer Modifications

The STOR-M interferometer [29] uses a 76GHz 100mW IMPATT (IMPact ionization Avalanche Transit-Time) Oscillator [30] in the following microwave circuit:

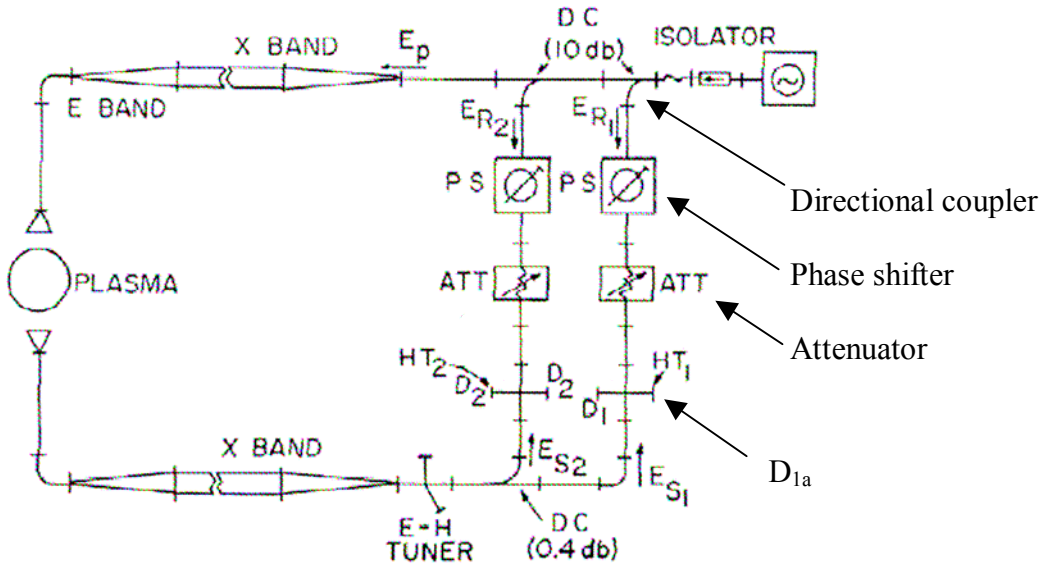

Figure 2-7: 4mm interferometer [29] used to measure chord averaged density in the STOR-M

The signal launched by the source is split into three components: E_p, E_{R1} and E_{R2}. E_p is transmitted through overmoded waveguides to minimize losses (see Section 4.2.4) and

then passes directly through the plasma (O-mode propagation), which generates a phase shift ($\Delta\varphi$) proportional to the density [29]. E_{R1} and E_{R2} are used as local oscillators to mix with E_{S1} and E_{S2}. Electromagnetic wave propagation through a magnetized plasma is discussed in detail in Section 3.3. D_1 and D_{1a} are configured in quadrature as follows

$$D_{1a} = E_{R2}^2 + E_{S2}^2 - 2E_{R2}E_{S2}\cos(\Delta\varphi) \quad \textbf{2-8}$$

$$D_1 = E_{R2}^2 + E_{S2}^2 + 2E_{R2}E_{S2}\cos(\Delta\varphi) \quad \textbf{2-9}$$

E_{R1} and E_{R2} are configured such that D_1 and D_2 are $\pi/2$ radians out of phase, therefore D_2 and D_{2a} measure the same values respectively as D_1 and D_{1a} but with E_{S1} and $\sin(\Delta\varphi)$ substituted for E_{S2} and $\cos(\Delta\varphi)$. One can see that $D_{1a} - D_1$ is proportional to $\cos(\Delta\varphi)$. To determine the phase shift ($\Delta\varphi$) of the wave by the plasma, one can use the WKB approximation (named after Wentzel, Kramers and Brillouin [31]). In this theory, one assumes that the properties of the plasma vary sufficiently slowly such that the wave can be considered as traveling through a uniform media. Therefore for any RF signal there is a local refractive index that defines the wave propagation in that region, and hence the chord averaged density can be determined from [26]

$$\Delta\varphi = \int k_{\text{plasma}}\,dl - \int k_{\text{o}}\,dl = \int (N-1)\frac{\omega}{c}\,dl \quad \textbf{2-10 (Phase Shift)}$$

$$N \equiv \frac{kc}{\omega} = \sqrt{1-\left(\frac{\omega_p}{\omega}\right)^2} \approx 1 - \frac{n_e}{2n_c} \quad \textbf{2-11 (Index of Refraction (O-Mode))}$$

$$n_c = \frac{m_e\varepsilon_0\omega^2}{e^2} \quad \textbf{2-12 (Cut-off Density)}$$

$$\overline{n} = \frac{1}{2a}\int n_e(r)\,dr = \frac{n_c c}{\omega a}\Delta\varphi \quad \textbf{2-13 (Chord Averaged Density)}$$

where ω is the microwave frequency and chord averaged means the average density of a chord through the centre of the plasma. Equation 2-11 assumes that n_e ($\approx 5\times10^{18}$ /m^3) is much less than n_c ($\approx 7\times10^{19}$ /m^3) which is reasonable. The cut-off density is the density at which the O-mode wave can no longer propagate, if $n > n_c$ the wave is reflected and absorbed by the plasma. n_c for 76 GHz is 7×10^{19} /m^3, 10 times greater then the STOR-M density. The phase shift is then determined by counting fringes between the $\cos(\Delta\varphi)$ and $\sin(\Delta\varphi)$ signals:

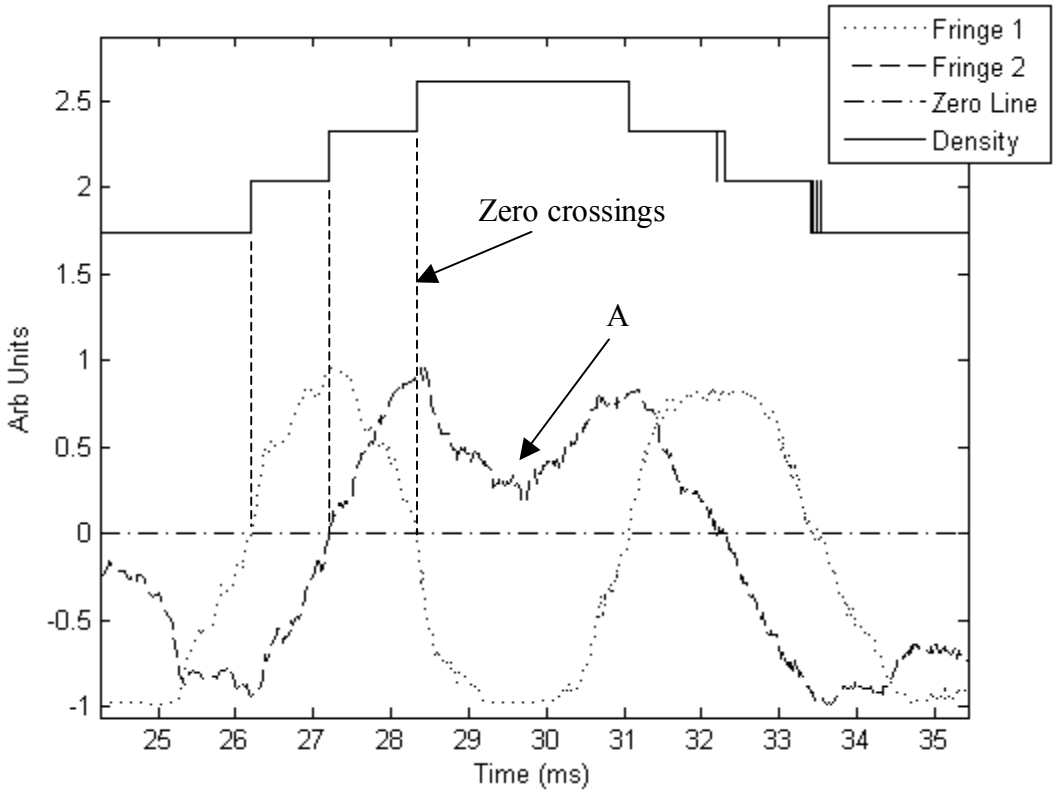

Figure 2-8: Demonstration of 'Fringe Counting' showing the importance of two signals to avoid saddle points

Referring to Figure 2-8, the 'Fringes' represent the sine and cosine functions and cross the 'Zero Line' when $\Delta\varphi$ has changed by $\pi/2$ radians, equivalent to a density change of 0.58×10^{12} /cm^3 as graphically represented by the steps in the 'Density' line. Two fringe signals are required to keep track of the sign of $d\varphi/dt$; point 'A' (known as a saddle point) for example represents a sign change in $d\varphi/dt$ that would not be detected if only 'Fringe 1' was measured. Two fringes also double the phase resolution for zero crossing to $\pi/2$ instead of π.

The original system on the STOR-M calculated the density directly using logic gates and high speed operational amplifiers. However, this system was prone to missing fringe points and having density step sizes of various values. As n_e is an important quantity for a scattering experiment, the density calculating circuitry was bypassed and the fringes were collected directly. A Matlab code was written to determine the density from the two fringe signals, this code was used to produce Figure 2-8.

Chapter 3

Theory

3.1 Theoretical Background

This chapter begins with a description of the propagation of the microwaves used in this experiment, both in the waveguides and in the plasma. The interaction between the wave and the plasma is then covered in detail providing a comprehensive understanding of the scattered signal. Finally the reader is introduced to basic tokamak physics, and a brief theoretical and experimental description of expected density fluctuations is provided.

3.2 Physics of guided waves in rectangular waveguides

Maxwell's equations in a source free region govern the physics of guided waves; the solution to these equations in a rectangular conducting waveguide is covered in various texts [32] [33] [34] and will not be repeated here. In this experiment the waves are guided in Standard Coin Silver (90% silver, 10% copper [35]) WR-8 rectangular waveguides (0.08"×0.04" inches ≈ 2×1 mm). The minimum cut-off frequency for WR-8 waveguide is 73.8 GHz (TE_{10}) with the next highest modes being the TE_{20} and TE_{01} at 147.5 GHz. Therefore the TE_{10} mode is propagated; the field arrangement of this mode is shown in WR-8 from a custom built FEMLAB (Finite Element Modeling Laboratory computer software) model:

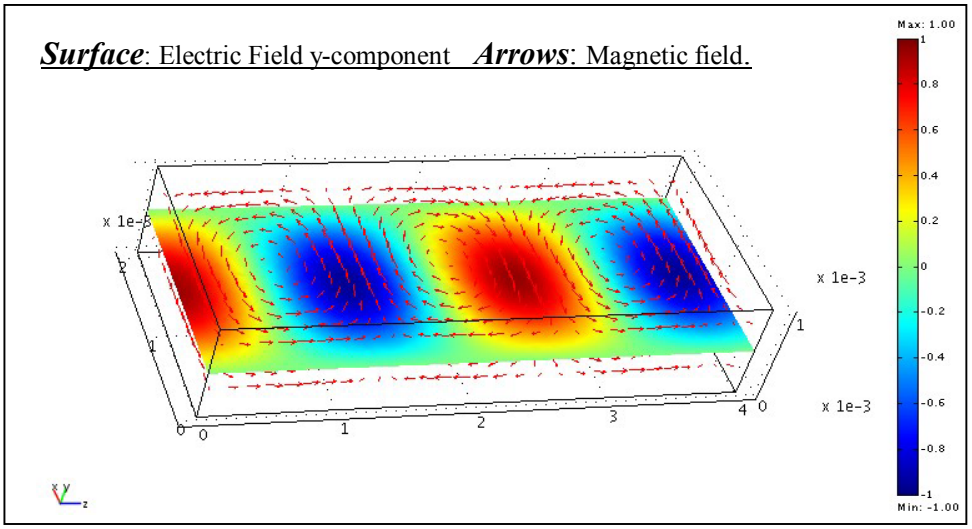

Figure 3-1: FEMLAB model showing TE_{10} mode wave propagation through a WR-8 rectangular waveguide.

It is important to note that the electric field is parallel to the shorter side of the waveguide, as the electric field direction defines the mode of the wave when passing through plasma immersed in a strong magnetic field. This concept is described in the following section.

3.3 Electromagnetic Wave Propagation in Plasma

Electromagnetic wave propagation in plasma is more complex than other media due to the existence of free charges. The propagation of the waves is governed by the following Maxwell's equations in a vacuum:

$$\nabla \times \vec{E} = -\frac{\partial \vec{B}}{\partial t} \qquad \textbf{3-1 (Maxwell's Equations in Vacuum)}$$

$$\nabla \times \vec{B} = \mu_0 \vec{j} + \mu_0 \varepsilon_0 \frac{\partial \vec{E}}{\partial t} \qquad \textbf{3-2}$$

The plasma properties are incorporated through the current term $\vec{j}$. One can treat the plasma as a continuous media with finite conductivity and define the current according to Ohm's Law. The magnetic field can be eliminated by taking the curl of 3-1 and the time derivative of 3-2. Then using a Fourier mode approach and Ohm's Law, 3-1 and 3-2 can be rewritten as:

$$\vec{k}\times\left(\vec{k}\times\vec{E}\right)+i\omega\left(\mu_0\ddot{\sigma}\cdot\vec{E}-i\omega\varepsilon_0\mu_0\vec{E}\right)=0 \qquad \textbf{3-3}$$

For a magnetized plasma the electric properties are not isotropic and the conductivity σ takes on a tensor form. Using the equation of motion for electrons in a fixed magnetic field one can determine the various possible solutions to 3-3. If the magnetic field $\vec{B}_0$ is taken to be along the *z*-axis and $\vec{k}$ is in the *y*-*z* plane, then the general dispersion equation can be described by the Appleton-Hartree refractive index formula (neglecting collisions and ions as the electromagnetic wave considered is high frequency at 140 GHz) [26]:

$$\frac{k^2c^2}{\omega^2}=N^2=1-\frac{X(1-X)}{1-X-\frac{1}{2}Y^2\sin^2\theta\pm\sqrt{\left(\frac{1}{2}Y^2\sin^2\theta\right)^2+(1-X)^2Y^2\cos^2\theta}}$$

3-4 (Appleton-Hartree refractive index)

Where ω is the frequency of the electromagnetic wave and the following relations are used:

$$X=\frac{\omega_{pe}^2}{\omega^2}\qquad Y=\frac{\omega_{ce}}{\omega} \qquad \textbf{3-5}$$

$$\omega_{pe}=electron\ plasma\ frequency=\sqrt{\frac{ne^2}{\varepsilon_0 m_e}} \qquad \textbf{3-6}$$

$$\omega_{ce}=electron\ cyclotron\ frequency=\frac{eB_0}{m_e} \qquad \textbf{3-7}$$

θ in 3-4 refers to the angle between $\vec{k}$ and $\vec{B}_0$ and is important in defining the mode of the wave, and *N* is the usual refractive index.. Equation 3-4 describes all possible dispersion relations that satisfy 3-3. Solutions using the positive sign from the Appleton-Hartree refractive index are commonly referred to as Ordinary waves ($\vec{E}\parallel\vec{B}$) and refer to situations when $\theta = \pi/2$; the minus sign indicates Extraordinary waves ($\vec{E}\perp\vec{B}$) and occurs when $\theta = 0$ [26].

In this experiment, the waveguide orientation is chosen such that $\vec{k}$ is perpendicular to the toroidal field ($\theta = \pi/2$) and $\vec{E}$ is parallel to $\vec{B}_t$. This results in Ordinary mode

($N^2 = 1-X$) propagation which has a cut-off if $\omega < \omega_p$ ($\approx$ 20 GHz in the STOR-M plasma). In this configuration the 140 GHz wave will propagate with minimum attenuation. Work performed by Shats *et al.* [17] shows that a 137 GHz O-mode wave is unaffected by a plasma with density $n_e \approx (5\text{-}10)\times 10^{18}$ /m^3; conditions very similar to the STOR-M plasma. If the orientation of the incident wave is incorrect, the other possible modes would not propagate through the STOR-M plasma and would be reflected and absorbed by the plasma when the density exceeds the critical density value for that respective mode.

3.4 Scattering Theory

The scattering of plane electromagnetic radiation from plasma is derived in numerous papers and books [16] [36] [37]. The derivation presented here does not follow any particular solution but uses components of them to guide the derivation. All work in this section is presented in SI units.

When a plane electromagnetic wave is incident upon a charged particle, it causes the particle to accelerate. The motion and acceleration of the charge causes it to emit scattered radiation. Radiation from a moving and accelerating charge is covered in numerous texts [32] and the result from *Jackson* [34], derived from the Liénard-Wiechert Potentials is presented below:

$$\vec{E}\left(\vec{R},t\right)=\frac{q_j}{4\pi\varepsilon}\left[\frac{\left(\hat{s}-\vec{\beta}\right)\left(1-\beta^2\right)}{\left(1-\hat{s}\cdot\vec{\beta}\right)^3\vec{R}'^2}\right]_{ret}+\frac{q_j}{4\pi}\eta\left[\frac{\hat{s}\times\left\{\left(\hat{s}-\vec{\beta}\right)\times\dot{\vec{\beta}}\right\}}{\left(1-\hat{s}\cdot\vec{\beta}\right)^3\vec{R}'}\right]_{ret} \qquad \textbf{3-8}$$

q_j = Charge of the particle

ε = Permittivity of the medium

c = Speed of light

$\eta = \sqrt{\frac{\mu_0}{\varepsilon_0}}$ = Intrinsic impedance

$\hat{s}$ = Unit normal in direction of scattered radiation

$\vec{\beta} = \vec{v}$ /c = Normalized velocity vector

$\vec{R}'$ = Vector from the retarded position to the field point

$\vec{R}$ = Field position

$[\ ]_{ret}$ = Equations within the brackets are evaluated at the retarded time

In scattering conditions the scale length L over which the interaction is studied is much smaller then $\vec{R}$ and $\vec{R}'$. This allows one to neglect the first term in Equation 3-8, set $\vec{R} \cong \vec{R}'$ and set $t' \cong t - \left(\frac{\left| \vec{R} - \hat{s} \cdot \vec{r} \right|}{c} \right)$. The thermal temperature of the STOR-M tokamak is approximately 200eV and 80eV for the electrons and ions, defining $\left| \vec{\beta} \right|$ as approximately 0.02 and 0.0003 respectively. Therefore Equation 3-8 can be re-written:

$$\vec{E}_s\left(\vec{R},t\right) = \frac{q_j}{4\pi R}\eta\left[\hat{s}\times\left(\hat{s}\times\dot{\vec{\beta}}\right)\right]_{ret} \qquad \textbf{3-9 (Scattered Electric Field)}$$

Consider a plane electromagnetic wave $\left(\vec{E}_i\left(\vec{r},t'\right) = \vec{E}_{i0}\exp\left(\vec{k}_i\cdot\vec{r} - \omega_i t'\right)\right)$ incident on a single free electron. The motion of the charge is governed by Newton's Second Law, where the $\vec{v}\times\vec{B}$ force term can be neglected assuming a non-relativistic case. The scattered radiation can be calculated assuming an unperturbed trajectory of the particle: $\vec{r}\,(t') = \vec{r}\,(0) + \vec{v}\,t'$:

$$\vec{E}_{sj}\left(\vec{R},t\right) = \frac{{q_e}^2}{4\pi R}\frac{\mu}{m_e}\left[\hat{s}\times\left(\hat{s}\times\vec{E}_{i0}\right)\right]\exp\left[i\left(\vec{k}_i\cdot\vec{r}\,(t') - \omega_i t'\right)\right]$$

$$= \left(\frac{\gamma_e}{R}\right)\left[\hat{s}\times\left(\hat{s}\times\vec{E}_{i0}\right)\right]\exp\left[i\left(k_i\frac{\left(1-\hat{i}\cdot\vec{\beta}\right)}{\left(1-\hat{s}\cdot\vec{\beta}\right)}R - \omega_i\frac{\left(1-\hat{i}\cdot\vec{\beta}\right)}{\left(1-\hat{s}\cdot\vec{\beta}\right)}t - k_i\frac{\left(1-\hat{i}\cdot\vec{\beta}\right)}{\left(1-\hat{s}\cdot\vec{\beta}\right)}\hat{s}\cdot\vec{r}(0) + \vec{k}_i\cdot\vec{r}(0)\right)\right]$$

$$= \left(\frac{\gamma_e}{R}\right)\left[\hat{s}\times\left(\hat{s}\times\vec{E}_{i0}\right)\right]\exp\left[i\left(k_s R - \omega_s t - \vec{k}\cdot\vec{r}\right)\right] \qquad \textbf{3-10}$$

$\vec{E}_{sj}$ is the scattering from a single electron, where $\vec{k}$ = $\vec{k}_s$ - $\vec{k}_i$ and γ_e is the classical electron radius. $\vec{k}$ can take both positive and negative values and represents the wavelength of the density fluctuation as will be shown. Figure 3-2 represents the scattering vectors.

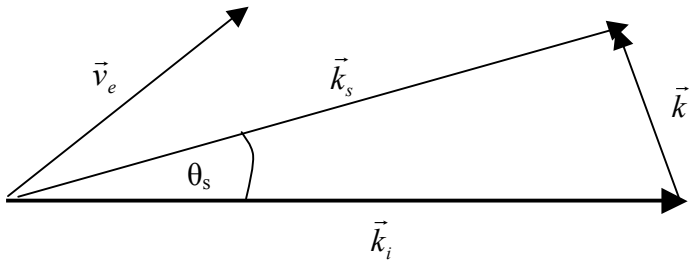

Figure 3-2: Scattering vector diagram illustrating the Bragg Condition: $k \approx 2k_i \sin\left(\frac{\theta_s}{2}\right)$ assuming $\left|\vec{k}_i\right| \approx \left|\vec{k}_s\right|$

Equation 3-10 describes the scattered radiation from a single electron. One may observe that the scattered radiation is slightly Doppler shifted from the incident radiation due to the motion of the electron ($\omega = \omega_s - \omega_i = \vec{k} \,.\, \vec{v}_e$). The power of the scattered signal is proportional to the electric field squared, this introduces a 1/mass^2 dependence and therefore radiation from ions in a plasma is negligible compared to that of the electrons.

There are two distinct ways that electromagnetic radiation can scatter from plasma: coherent and incoherent scattering. In tokamak plasmas the faster moving electrons will tend to form Debye shields around the more massive ions. If the phase difference between the electrons in the shield is sufficiently large, then scattering from these electrons will be incoherent. However, if there is negligible phase difference, then the scattered fields between the electrons will tend to sum coherently. This phase difference is frequently described through the dimensionless quantity α [37]:

$$\lambda_D = \sqrt{\frac{\varepsilon_0 k_B T}{ne^2}} \qquad \textbf{3-11 (Debye Length)}$$

$$\alpha = k\lambda_D = 2k_i \sin\left(\frac{\theta_s}{2}\right)\sqrt{\frac{\varepsilon_0 k_B T}{ne^2}} \qquad \textbf{3-12}$$

α >1 relates to the incoherent scattering case and α <1 represents a coherent scattering situation. The angular dependence in 3-12 is derived from Figure 3-2 assuming $\left|\vec{k}_s\right| \approx \left|\vec{k}_i\right|$. For the STOR-M plasma a 140 GHz incident wave has α ≈ 0.1/sin(θ_s/2) which is ~ 1 for the smallest scattering angle used ($\theta \approx 10^o$ for $\left|\vec{k}\right|$ = 5/cm) and < 1 for all the other

measurements. Therefore one must calculate the scattered signal based on a coherent approach, which is required as one is attempting to investigate the collective properties of the electrons.

The scattering occurs in a defined scattering volume and within this volume the electrons can be modeled by a Klimontovich distribution function [37].

$$F_e(\vec{r},\vec{v},t')=\sum_{j=1}^{N_e}\delta\left(\vec{r}-\vec{r}_j(t')\right)\delta\left(\vec{v}-\vec{v}_j(t')\right)\delta\left(t'-t+\frac{R}{c}-\frac{\hat{s}}{c}\cdot\vec{r}_j\right) \quad \textbf{3-13 (Klimontovich distribution function)}$$

where $\vec{r}$ and $\vec{v}$ are the position and velocity of particles in the system. The Klimontovich distribution allows calculation of the total scattered $\vec{E}_s^T(t)$ field from the scattering volume V with total electrons N_e. As it is the power of the scattered signal that will be measured, one must determine the total scattered power from the time averaged Poynting vector:

$$\vec{E}_s^T(\vec{R},t)=\int d\vec{r}\int d\vec{v}F_e(\vec{r},\vec{v},t')\vec{E}_{sj}\left(\vec{R},t'\right) \quad \textbf{3-14}$$

$$P_s(\vec{R})=R^2\Omega c\varepsilon_o\lim_{T\to\infty}\frac{1}{T}\int_{\frac{-T}{2}}^{\frac{T}{2}}dt\left|\vec{E}_s^T\left(\vec{R},t\right)\right|^2 \quad \textbf{3-15}$$

$$P_s\left(\vec{k}\right)=\frac{\gamma_e^2P_i\Omega}{A}N_e\left|\hat{s}\times\left(\hat{s}\times\hat{E}_{io}\right)\right|^2\int_{-\infty}^{\infty}S\left(\vec{k},\omega\right)d\omega \quad \textbf{3-16 (Scattered Power)}$$

P_i = Incident power

γ_e = Classical electron radius

A = Area of incident signal (known from horn radiation pattern, see Figure 4-7)

N_e = Number of electrons in the scattering volume

$$S\left(\vec{k},\omega\right)\equiv\lim_{T\to\infty,V\to\infty}\frac{1}{TV}\left\langle\frac{\left|n_e\left(\vec{k},\omega\right)\right|^2}{n_{eo}}\right\rangle \quad \textbf{3-17 (Spectral Density Function)}$$

$\omega = \omega_s \pm \omega_i$

n_{eo} = Average electron density

$\langle\ \rangle$ = Ensemble average as described in Appendix 1

Appendix 1 shows the complex derivation of 3-16 from 3-15. Equation 3-16 represents the power scattered from the plasma for a specific scattering vector $\vec{k}$. $S(\vec{k}, \omega)$ is the spectral density function and represents the density fluctuations of the system in terms of their wavelength and frequency. Usually $S(\vec{k}, \omega)$ is integrated over the frequency to determine $S(\vec{k})$; the total scattering cross section. $S(\vec{k}, \omega)$ measurements are the goal of this experiment.

3.5 Tokamak Physics

Consider a charged particle *j* with velocity $\vec{v}_j$ in the presence of a magnetic field B_z and an arbitrary force $\vec{F}$:

$$m_j \frac{d\vec{v}_j}{dt} = \vec{F} + q_j \vec{v}_j \times \vec{B} \qquad \textbf{3-18 (Equation of motion)}$$

where *m* and *q* are the mass and charge of the particle respectively. Motion along the magnetic field has a simple solution; however, motion in the *x*-*y* plane is solved from an ordinary first order differential equation:

$$v_{jz} = \frac{F}{m_j} t + v_{jzo}, \quad v_{jx} = v_\perp e^{i\omega_c t} + \frac{F_y}{q_j B}, \quad v_{jy} = v_\perp e^{i\omega_c t} - \frac{F_x}{q_j B} \qquad \textbf{3-19}$$

$$\vec{v}_{jgc} = \frac{\vec{F} \times \vec{B}}{q_j B^2} \qquad \textbf{3-20}$$

$v_\perp$ is the perpendicular velocity and $\omega_{cj} = \frac{q_j B}{m_j}$ is the cyclotron frequency. In the absence of an external force ($\vec{F} = 0$), equation 3-19 describes the usual helical motion of a charged particle in a magnetic field with Larmor radius $\rho_j = \frac{v_\perp}{\omega_{cj}}$. When an external force is present, the centre of gyration moves with velocity $\vec{v}_{gc}$ known as the guiding centre drift, and is shown as the second components of $\vec{v}_x$ and $\vec{v}_y$. If $\vec{F}$ is proportional to q_j then the resulting motion is charge independent, as is the case for an electric field causing collective $\vec{E} \times \vec{B}$ motion as $\vec{F} = q_j \vec{E}$.

Although the toroidal field (B_t) is the main method of confining the plasma, it also introduces numerous confinement problems. Two major reasons are the non-uniformity ($B_t \propto 1/R$) and curvature. The curvature introduces a centrifugal force in the radial direction, the $1/R$ dependence means that during a gyration the particle experiences a varying $\vec{B}$ field. These two forces combine to produce a curved vacuum field drift [27]

$$\vec{v}_{R+\nabla B} = \frac{m}{q}\left(v_{\parallel}^2 + \frac{v_{\perp}^2}{2}\right)\frac{\vec{R}\times\vec{B}}{R^2B^2} = \frac{v_{th}^2}{\omega_c}\frac{\vec{R}\times\vec{B}}{R^2B} \qquad \textbf{3-21}$$

with R the radius of curvature and $\vec{v}_{\parallel}$ the velocity parallel to $\vec{B}$. From 3-21 it is apparent that a toroidal magnetic field causes a vertical separation of the ions and electrons:

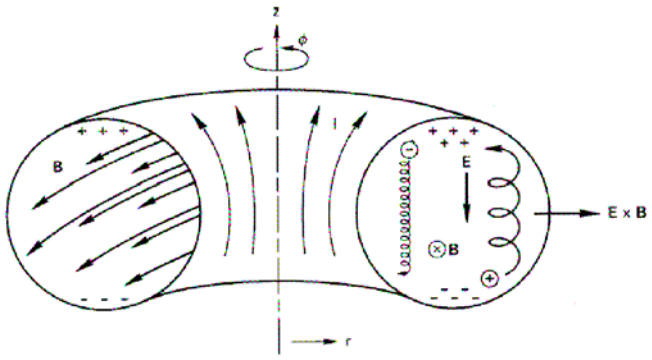

Figure 3-3: Particle motion in a toroidal field illustrating vertical charge separation, Chen [38]

The charge separation creates a vertical electric field which drives a strong $\vec{E}\times\vec{B}$ flow (charge independent) horizontally out of the plasma. These losses are prevented by introducing a small poloidal field (B_θ) from an induced plasma current. In the STOR-M this field is approximately 5% of B_t and results in a helical magnetic field. Therefore as the charges follow this helical field, charge separation from the non-uniform field is short circuited and these $\vec{E}\times\vec{B}$ losses are removed.

This helical field can be described as a nested set of helical magnetic surfaces. Often a safety factor q is used to describe the field [28]

$$q = \frac{\Delta\varphi}{2\pi} \approx \frac{rB_\phi}{R_0 B_\theta} \qquad \textbf{3-22 (Safety Factor)}$$

where $\Delta\varphi$ is the toroidal angle change (rotation around the torus) required for a magnetic field line to circulate around the torus before reconnection, the approximate solution is for a circular cross section with large inverse aspect ratio $\left(\varepsilon = r/R_0\right)$. q is known as the 'safety factor' for its common usage in MHD stability analysis [39], generally larger q leads to MHD stabilization. The variation of q with minor radius is used as a measure of magnetic shear:

$$s = \frac{r}{q}\frac{dq}{dr} \qquad \textbf{3-23 (Magnetic Shear)}$$

Now consider introducing a pressure gradient term ∇p into the equation of motion based on the fluid model:

$$mn\left[\frac{\partial \vec{v}}{\partial t} + (\vec{v}\cdot\nabla)\vec{v}\right] = qn\left(\vec{E} + \vec{v}\times\vec{B}\right) - \nabla p \qquad \textbf{3-24}$$

The ratio of the partial derivative term to $\vec{v}\times\vec{B}$ is approximately ω/ω_c (where ω is the perturbation fluctuation frequency), as ω_c is very large ($\approx$ 20 GHz) this term can be neglected for lower frequency terms. Also, as will be shown, $\vec{v}$ is perpendicular to its gradient ($(\vec{v}\cdot\nabla)\vec{v}$ =0) and therefore the left hand side of 3-24 is equal to zero. Therefore the velocity can be written:

$$\vec{v} = \frac{\vec{E}\times\vec{B}}{B^2} - \frac{\nabla p\times\vec{B}}{qnB^2} \equiv \vec{v}_E + \vec{v}_D \qquad \textbf{3-25}$$

where $\vec{v}_E$ is the $\vec{E}\times\vec{B}$ drift and $\vec{v}_D$ is the diamagnetic drift. The $\vec{E}\times\vec{B}$ flows play an important role in H-mode discharges [40]. H-mode refers to discharges with enhanced plasma confinement [41] where various techniques can be used to suppress density fluctuations in the plasma; these H-mode shots have been triggered in the STOR-M through turbulent heating [19], compact-torus injection [23] and electrode biasing [21].

The description above does not allow for variations of the electric field that are small compared to the Larmor radius, or a time dependant electric field. Finite Larmor radius (FLR) effects are important when the mode being studied has a wavelength smaller then the ion gyro-radius. To account for $\vec{E}(t)$, one simply solves the equation of motion 3-18, replacing $\vec{F}$ with $q\vec{E}(t)$.

$$\vec{v}_p = \frac{1}{\omega_c B}\frac{d\vec{E}(t)}{dt}$$ **3-26 (Polarization Drift)**

Accounting for FLR effects is more complicated but can be achieved by Taylor expanding a non-uniform electric field about the gyro-centre; assuming a field of the form: $E_\perp(\vec{r}) = E_o e^{i\vec{k}_\perp\cdot\vec{r}}$ this becomes [42]:

$$\begin{aligned} E_\perp\left(\vec{r}_g + \vec{\rho}(t)\right) &= E_\perp\left(\vec{r}_g\right) + \left(\vec{\rho}(t)\cdot\frac{\partial}{\partial\vec{r}_g}\right)E_\perp\left(\vec{r}_g\right) + \left(\vec{\rho}(t)\cdot\frac{\partial}{\partial\vec{r}_g}\right)^2\frac{E_\perp\left(\vec{r}_g\right)}{2} + \ldots \\ &= \left(1 + i\vec{k}_\perp\cdot\vec{\rho}(t) - \frac{1}{2}\left(\vec{k}_\perp\cdot\vec{\rho}(t)\right)^2 - \frac{i}{6}\left(\vec{k}_\perp\cdot\vec{\rho}(t)\right)^3 + \ldots\right)E_\perp\left(\vec{r}_g\right) \end{aligned}$$ **3-27**

where $\vec{\rho}(t) = \rho\left(\cos(\omega_c t)\hat{x} + \sin(\omega_c t)\hat{y}\right)$ is the Larmor orbit and $\vec{r}_g$ is the guiding centre location. It is not possible to fully solve the equation of motion for this situation; therefore the standard particle orbit in the absence of an electric field is used to determine the effective field seen by the gyrating particles. This is done by time averaging along the particle orbit to determine the effective field seen by the particle [43]

$$\begin{aligned} \left\langle E_\perp\left(\vec{r}_g\right)\right\rangle_{eff} &= \left(1 - \frac{1}{4}(k_\perp\rho)^2 + \frac{1}{64}(k_\perp\rho)^4 - \frac{1}{2304}(k_\perp\rho)^6 + \ldots\right)E_0 e^{ik_\perp\cdot\vec{r}_g} \\ &= J_0(k_\perp\rho)E_0 e^{ik_\perp\cdot\vec{r}_g} \end{aligned}$$ **3-28**

where J_0 is the Bessel function of the first kind. 3-28 is the average field seen by the gyrating particle along its orbit. The field experienced by the guiding centre is found by using the field of 3-30 at the gyro-radius of the particle orbit, and then using this field to determine the field at the guiding centre:

$$\left\langle\left\langle E_\perp\left(\vec{r}_g\right)\right\rangle\right\rangle_{eff} = J_0^2(k_\perp\rho)E_0 e^{ik_\perp\cdot\vec{r}_g}$$ **3-29**

The effective field seen by the particle fluid can be determined by averaging over the velocity with Maxwellian weighting:

$$\begin{aligned} E_{\perp eff} &= E_0 e^{i\vec{k}\cdot\vec{r}_g}\int_0^\infty\int_{-\infty}^\infty\left(\frac{m}{2\pi T}\right)^{\frac{3}{2}}J_0^2\left(k_\perp\rho_i\frac{v_\perp}{\rho_i\omega_{ci}}\right)e^{\frac{-m}{2T}\left(v_\perp^2+v_\parallel^2\right)}2\pi v_\perp dv_\perp dv_\parallel \\ &= e^{-(k_\perp\rho_i)^2}I_0\left(\left(k_\perp\rho_i\right)^2\right)E_0 e^{i\vec{k}\cdot\vec{r}_g} \end{aligned}$$ **3-30**

where I_0 is the modified Bessel function and the following identities were used

$$\int_0^\infty J_0^2\left(k_\perp \rho_i x\right) e^{\frac{-x^2}{2}} x dx = e^{-(k_\perp \rho_i)^2} I_0\left[\left(k_\perp \rho_i\right)^2\right] \qquad \textbf{3-31}$$

$$x = \frac{v_\perp}{\rho_i \omega_{ci}} \qquad \rho_i = \frac{\sqrt{T_i / m_i}}{\omega_{ci}} \qquad \textbf{3-32}$$

This results in a modified $\vec{E}\times\vec{B}$ velocity for arbitrary $k_\perp \rho_i$:

$$\vec{v}_E = e^{-(k_\perp \rho_i)^2} I_0\left[\left(k_\perp \rho_i\right)^2\right] \frac{\vec{E}\times\vec{B}}{B^2} \qquad \textbf{3-33}$$

Another important tokamak property due to the non-uniformity of the magnetic field is the presence of trapped particles. Consider a particle traveling in a magnetic field, it has a constant energy (KE $\propto v_\perp^2 + v_\parallel^2$) and magnetic moment ($\mu \equiv \frac{1}{2} m v_\perp^2 / B$). Therefore a particle orbiting outboard in a tokamak will experience an increasing magnetic field as it moves to lower *R*. In order to maintain μ, $v_\perp$ must decrease and if $v_\parallel$ is relatively small enough then the particle can be reflected by the increase in B_t. This results in a 'banana' orbit as shown in Figure 3-4 below:

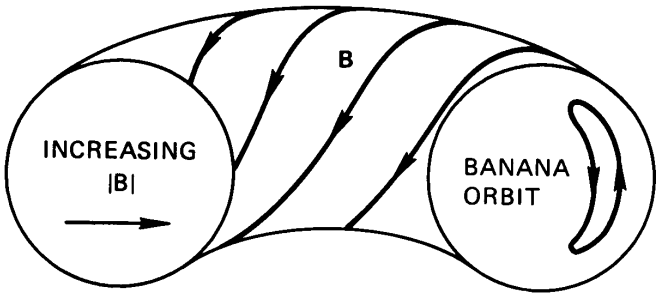

Figure 3-4: Banana orbit of trapped particles, Chen [38]

Particles within this orbit are known as trapped particles and remain within the banana orbit unless de-trapped through collisions. Particle trapping plays an important role in estimating the diffusion coefficient of the system and is strongly dependant on the collision frequency. Unlike circulating particles, trapped particles only experience

fractions of passing waves and as such are more susceptible to be driven from the system through instabilities and collisional processes [44] in anomalous transport.

3.6 Drift Waves

In tokamaks there are a large number of drift-type modes that are unstable [28]. A drift-type mode generically refers to drifts of the guiding centre of the particles. As a first approximation, consider a plasma slab in a uniform magnetic field ($\nabla\vec{B} = 0$), where $\vec{B}$ = B_z, $\vec{E}$ = E_y and there is a density and pressure gradient in the x direction. Assume electrons have a low inertia such that they flow quickly along the magnetic field lines in order to maintain a force balance:

$$F_{\|e} = -n_e e E_{\|} + \nabla_{\|} p_e = 0 \qquad \textbf{3-34}$$

Assuming no gradients in T_e and $n_e = n_{eo} + \tilde{n}_e$:

$$\tilde{n}_e = \frac{e\phi}{T_e} n_{e0} \qquad \textbf{3-35 (Boltzmann Distribution)}$$

which is the usual Boltzmann density distribution, where $E_{\|} = -\nabla_{\|}\phi$. As this work studies $\left(k_{\perp}\rho_i\right)^2$ up to ~ 1 (ρ_i ~ 0.1 cm and $\left|\vec{k}_{\max}\right|$ = 10 /cm) a kinetic approach must be used in order to determine the dispersion relation, as the fluid method used in section 3.5 assumes $\left(k\rho_i\right)^2 << 1$. This is done by equating the electron density fluctuation $\left(\tilde{n}_e\right)$ from Equation 3-35 with the kinetic ion density fluctuation [45]

$$\tilde{n}_i = \left(-1 + \frac{\omega + \hat{\omega}_{*i}}{\omega} e^{-bi} I_0\left(b_i\right) \right) \frac{e\phi}{T_i} n_{i0} \qquad \textbf{3-36}$$

$$\hat{\omega}_{*i} = \omega_{*i} + \omega_{*i}\eta_i b_i \frac{\partial}{\partial b_i} \qquad \textbf{3-37}$$

$$\eta_i = \frac{L_n}{L_{T_i}} \qquad \textbf{3-38 (Ion temperature gradient parameter)}$$

where $b_j = \left(k\rho_j\right)^2$, $L_j^{-1} = -\frac{1}{j}\frac{dj}{dx}$ is the gradient scale length of parameter 'j', $\omega_{*e(i)}$ = $-\frac{k_{\perp}T_{e(i)}}{eBn_{e(i)}}\frac{dn_{e(i)}}{dx}$ is the electron (ion) diamagnetic drift frequency and once again the

modified Bessel function (I_0) appears as seen in the fluid Equation 3-33. Equating 3-36 and 3-35 from quasi-neutrality in the plasma provides the following dispersion relation

$$\omega = \frac{\left(I_0(b_i) + \eta_i b_i \left(I_1(b_i) - I_0(b_i)\right)\right) e^{-b_i}}{1 + \tau - \tau I_0(b_i) e^{-b_i}} \omega_{*e} \qquad \textbf{3-39}$$

where $\tau = T_e / T_i$ is usual the temperature ratio. Using the identity $b_s = b_i \tau$, Equation 3-39 can be rewritten in terms of b_s, which will be shown to be the correct scaling length for ion drift wave turbulence [44]. Then a plot of ω/ω_{*e} versus $b_s = (k_\perp \rho_s)^2$ requires knowing only the temperature ratio ($\tau \approx 2.5$) and η_i. If one assumes parabolic profiles for n_i and T_i then it follows that $\eta_i = 1$ without the need to specify absolute values for the temperature or density.

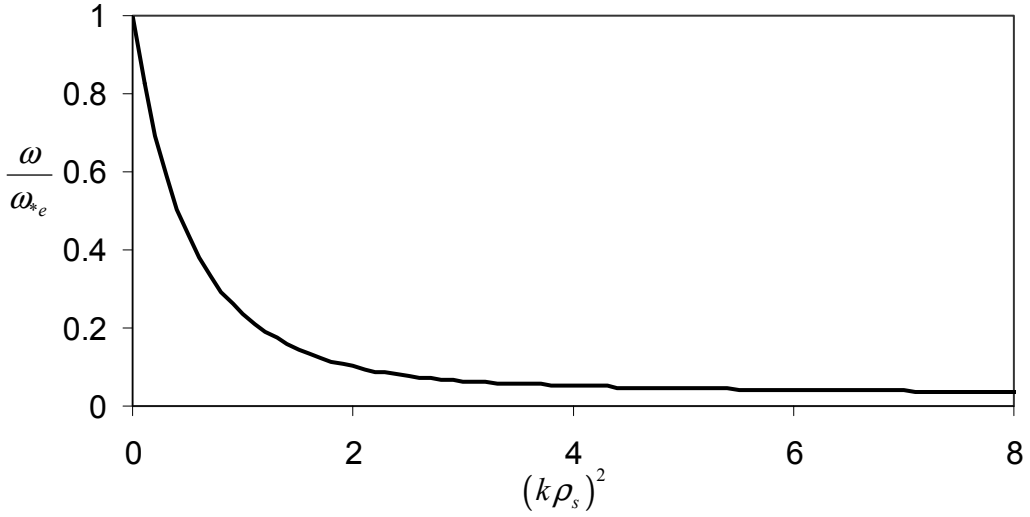

Figure 3-5: Kinetic ion drift wave model dispersion relation.

Figure 3-5 shows $\omega/\omega_{*e} \sim 0$ - 1, using parabolic approximations for n_e and T_e and averaging ω_{*e} with density weighting, an approximate electron diamagnetic frequency can be calculated for the STOR-M plasma

$$n_e = \frac{3}{2}\bar{n}_e \left(1 - \frac{r^2}{a^2}\right), \qquad T_e = \frac{3}{2}\bar{T}_e \left(1 - \frac{r^2}{a^2}\right) \qquad \textbf{3-40}$$

$$\frac{\bar{\omega}_{*e}}{2\pi} = \bar{f}_{*e} \approx \frac{\int_0^a \frac{k_\perp T_e(r)}{eBn_e(r)} \frac{dn_e(r)}{dr} \cdot n_e(r)\, dr}{2\pi \int_0^a n_e(r)\, dr} \approx 21{,}000\, k_\perp \qquad \textbf{3-41}$$

where $\overline{n}_e$ and $\overline{T}_e$ are the mean density and temperature respectively as measured by the diagnostic equipment, and $\overline{f}_{*e}$ is the mean electron diamagnetic frequency in Hertz. During the experiment $k_\perp$ is varied from 5 – 10 /cm indicating an expected mean frequency range of the order $\overline{f} \approx 105\,\text{kHz} \rightarrow 210\,\text{kHz}$. This is in agreement with experiments that roughly suggest [70]

$$\bar{f} \sim \frac{\rho_i}{L_n}\frac{\omega_{ci}}{2\pi} \qquad \textbf{3-42}$$

where $\bar{f}$ is the mean fluctuation frequency. Averaging $\bar{f}$ over the STOR-M parameters suggests $\bar{f} \approx$ 130 kHz in the plasma. Therefore as a first approximation, the kinetic model provides a reasonable estimate for the frequencies and behavior expected for drift waves. However, this model suggests no growth nor damping of the waves, this occurs through a non-adiabatic modification to 3-35 [46];

$$\frac{n_e}{n_0} = \frac{e\phi}{T_e} - i\delta\frac{e\phi}{T_e} \qquad \textbf{3-43}$$

The deviation from the Boltzmann distribution (iδ) can be caused by various factors not included in the first approximation: Landau damping, trapped electrons and collisions. The microinstability that results is known as the electron drift mode; originally thought to be unstable in all tokamaks and often referred to as the 'universal instability' [28].

As δ is generated from numerous sources, drift waves tend to be a coupling between several non-linear modes until some turbulence saturation level is reached. This is demonstrated by the broad frequency spectrum measured in specific spatial locations [47]

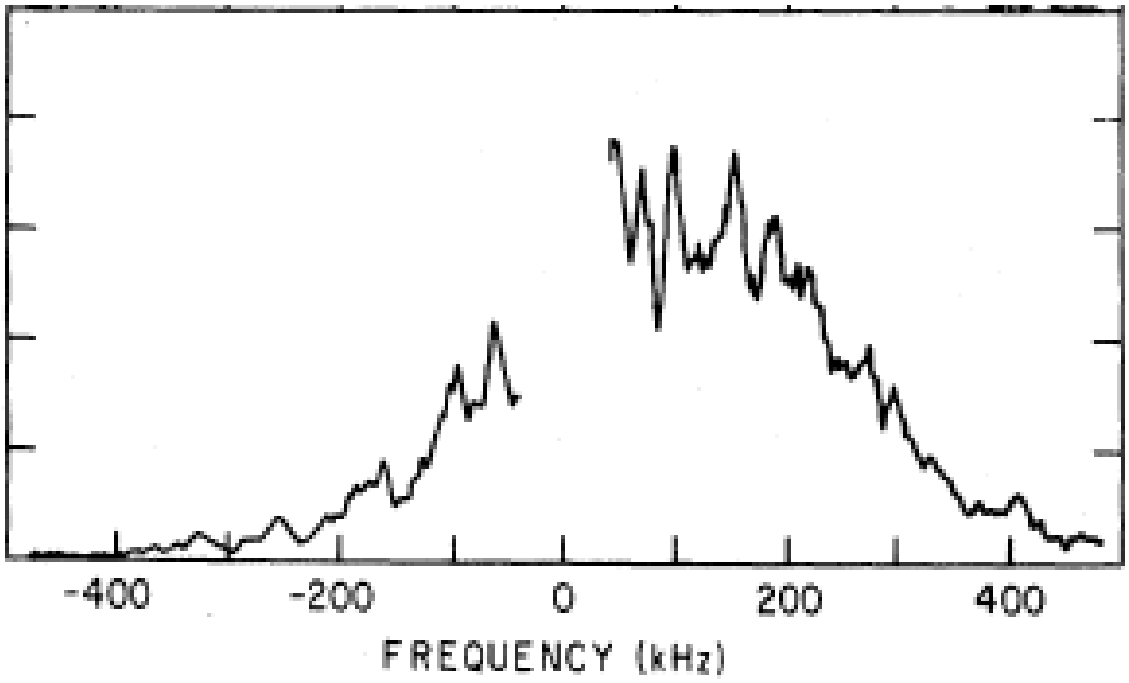

Figure 3-6: Broadband frequency density fluctuation spectra measured by Mazzucato [47] using a heterodyne microwave scattering system. The system is unable to measure frequencies near 0 kHz leaving a gap in the spectrum.

Figure 3-6 was measured on PLT (Princeton Large Tokamak) in a heterodyne microwave scattering experiment. Such broadband turbulence suggests that drift waves are in fact turbulent and not a superposition of linear modes. Furthermore this turbulence is experimentally found to maximize on the order $\tilde{n}/n \sim \left(\bar{k}_\perp L_n\right)^{-1}$ where $\bar{k}_\perp$ is the mean perpendicular wave vector and L_n is the density gradient scale length [70]. Non-linear theoretical models and scattering experiments point to this mode maximizing on the order of the ion Larmor radius with electron temperature [44]

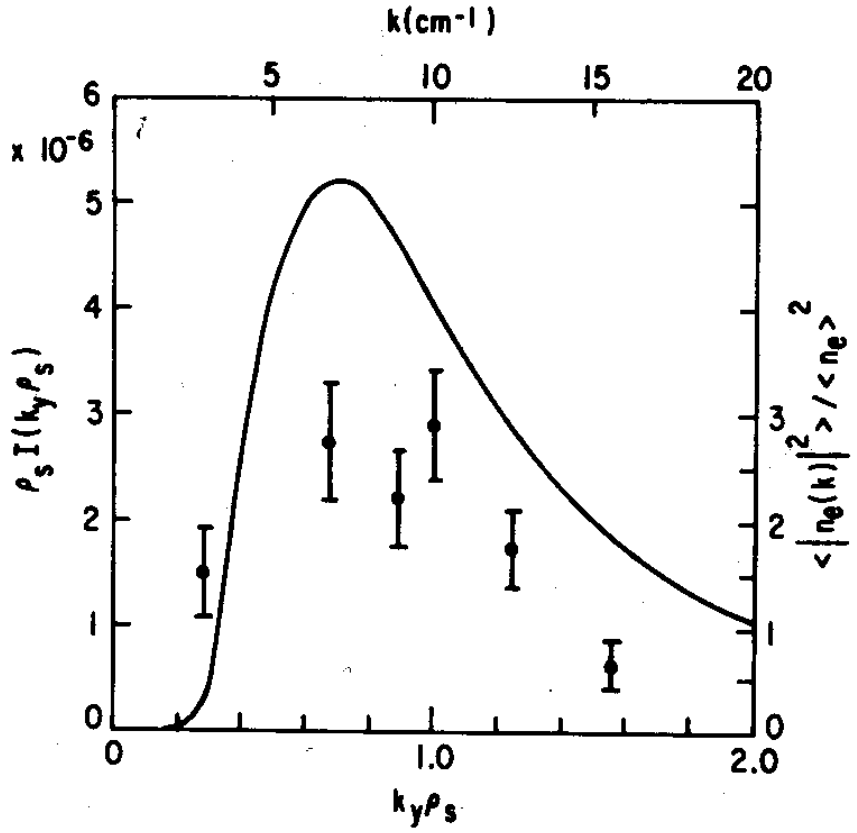

Figure 3-7: Comparison of a non-linear mode to scattering data of the fluctuation level, Tang [44]

Figure 3-7 compares an approximate non-linear model to microwave scattering data and demonstrates maximum fluctuations on the order $k_\perp \rho_s \sim 1$, defining the saturation level as:

$$\frac{\tilde{n}_e}{n_e} \sim \frac{1}{\bar{k}_\perp L_n} \sim \frac{\rho_s}{L_n} \qquad \textbf{3-44}$$

As ρ_s is proportional to $\sqrt{T_e}$ and B_t^{-1}, the fluctuation level can be examined by varying both T_e and B_t and looking for the $\sqrt{T_e}$ and B_t^{-1} behavior of the different density fluctuation levels for different plasma parameters, and maximization near $k_\perp \rho_s \sim 1$.

3.7 Electron Temperature Gradient (ETG) Mode

The ETG mode exists for much smaller wavelengths and higher frequencies than the ion drift-type modes, and can only be examined using full kinetic theory. This means that complete analytical results as derived for drift waves are not possible. As ETG signatures were not detected in this experiment, only a brief overview of this mode is presented to indicate its important characteristics for classifying this mode. In current modern tokamaks, drift modes can be suppressed in H-Mode type discharges (discharges with enhanced plasma confinement), leaving ETG modes as the prime candidate for the persistent anomalous electron losses [48].

At the simplest level, the ETG mode can be considered as an electrostatic perturbation and is formulated from first order perturbations [43]:

$$\begin{aligned} f &= f_0 + \tilde{f}_1 \\ \vec{E} &= \vec{E}_0 + \tilde{\vec{E}}_1 \\ \vec{B} &= \vec{B}_0 \end{aligned} \qquad \textbf{3-45}$$

where f is the particle distribution function, '$_0$' is the mean parameter level and '$_1$' is the first order fluctuation in the relevant parameter. The parameters of 3-45 are then placed into the kinetic Vlasov equation (Boltzmann equation with the collision operator set to zero):

$$\frac{\partial f}{\partial t} + \vec{v} \cdot \nabla f + \frac{q}{m}\left(\vec{E} + \vec{v} \times \vec{B}\right) \cdot \frac{\partial f}{\partial \vec{v}} = 0 \qquad \textbf{3-46 (Vlasov Equation)}$$

Substituting the first order perturbations gives:

$$-i\left(\omega - \vec{k} \cdot \vec{v}\right)\tilde{f}_1 - \omega_c \frac{\partial \tilde{f}_1}{\partial \alpha} + i\left(\vec{k} \cdot \vec{v} - \omega + \omega\right)\frac{e\phi}{T} f_M = 0 \qquad \textbf{3-47}$$

$$\tilde{f}_1 = \frac{e\phi}{T} f_M + g(\alpha) \qquad \textbf{3-48}$$

where α is the gyro-angle ($\alpha = \tan^{-1}(v_y/v_x)$) , the relationships $\frac{e}{m}\vec{v}_\perp \times \vec{B} \cdot \frac{\partial \tilde{f}_1}{\partial \vec{v}_\perp} = -\omega_c \frac{\partial \tilde{f}_1}{\partial \alpha}$ and $\frac{\partial f_0}{\partial \vec{v}} = -\frac{m}{T}\vec{v} f_M$ have been employed, $e^{i\omega t}$ perturbations are assumed and g(α) is the solution of the following first order differential equation:

$$\frac{\partial g(\alpha)}{\partial \alpha} + \frac{i}{\omega_c}\left(\omega - \vec{k}\cdot\vec{v}\right)g(\alpha) + i\frac{\omega}{\omega_c}\frac{e\phi}{T} f_M = 0 \qquad \textbf{3-49}$$

Equation 3-49 can be solved directly

$$g(\alpha) = -i\frac{\omega}{\omega_c}\frac{e\phi}{T} f_M \int e^{i\frac{\left(w\alpha - k_\parallel v_\parallel - k_\perp v_\perp \sin\alpha\right)}{\omega_c}} d\alpha \cdot e^{-i\frac{\left(w\alpha - k_\parallel v_\parallel - k_\perp v_\perp \sin\alpha\right)}{\omega_c}} \qquad \textbf{3-50}$$

$$\vec{k}\cdot\vec{v} = k_\perp v_\perp \cos\alpha + k_\parallel v_\parallel \qquad \textbf{3-51}$$

Then using the Bessel relation $e^{ix\sin\alpha} = \sum_n J_n(x) e^{inx}$, g(α) can be expressed as

$$g(\alpha) = \sum_{n,m} J_n\left(\frac{k_\perp v_\perp}{\omega_c}\right) J_m\left(\frac{k_\perp v_\perp}{\omega_c}\right) e^{i(m-n)\alpha} \frac{\omega}{\omega - k_\parallel v_\parallel - n\omega_c}\frac{e\phi}{T} f_M \qquad \textbf{3-52}$$

The solution so far has neglected the $\vec{E}\times\vec{B}$ drift and the ion magnetic drift present in a tokamak geometry. These appear as corrections to $\vec{v}$ in Equation 3-47 and carry directly through the derivation. Considering only low frequency modes with $\omega << \omega_c$ means only the lowest order harmonic remains and the desired perturbed distribution function is found:

$$\tilde{f}_\mu = -\frac{e_\mu\phi}{T_\mu} f_{M\mu} + \frac{\omega - \hat{\omega}_{*\mu}}{\omega + \hat{\omega}_{D\mu} - k_\parallel v_\parallel} J_o^2\left(\frac{k_\perp v_\perp}{\omega_{c\mu}}\right)\frac{e_\mu\phi}{T_\mu} f_{M\mu} \qquad \textbf{3-53 (Perturbed Distribution)}$$

$$\hat{\omega}_{*\mu} = \frac{T_\mu}{e_\mu}\vec{V}_{E\mu}\cdot\vec{k} \qquad \textbf{3-54 (Diamagnetic Frequency)}$$

$$\hat{\omega}_{D\mu} = -\vec{k}\cdot\vec{V}_{D\mu} \qquad \textbf{3-55 (Magnetic Drift Frequency)}$$

where μ indicates the particle species (electrons or ions). The mode behavior is then found by solving Poisson's equation and the parallel Ampere's Law:

$$\varepsilon_0 \nabla^2 \phi = -e \int (f_i - f_e)\, d\vec{v} \qquad \textbf{3-56}$$

$$\nabla_{\perp}^2 A_{\parallel} = -\mu_o \int v_{\parallel} (f_i - f_e)\, d\vec{v} \qquad \textbf{3-57}$$

The solution of the coupled equations 3-56 and 3-57 lead to an electromagnetic dispersion relation valid for arbitrary $k_{\perp}\rho_s$ [14]. Note that the application of Poisson's equation indicates the assumption of charge non-neutrality in the regime of interest. The complete dispersion equation can only be solved through complex numerical techniques beyond the scope of this work. Recent work by Hirose [15] using this technique shows that ETG modes do not scale with $(k_{\perp}\rho_e)^2$ (which would be expected if the electron drift modes were analogous to the ion drift modes with switching between ions and electrons), but instead $(k_{\perp}/k_{De})^2$ is the relevant parameter, where k_{De} is the wave number with Debye wavelength. A typical plot of this mode is shown in Figure 3-8 below

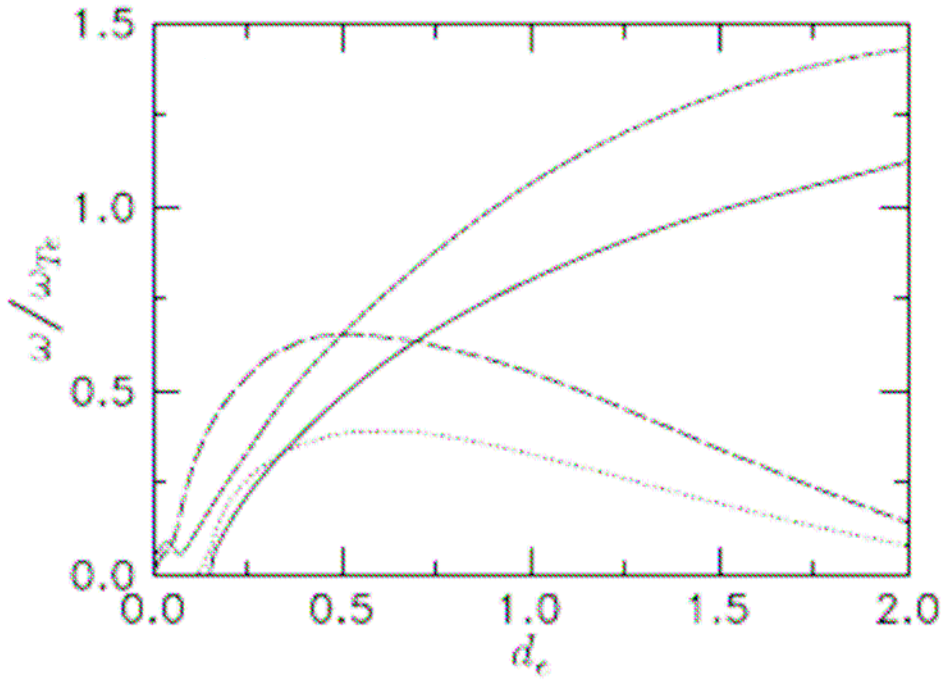

Figure 3-8: ETG dispersion relation from Hirose [15]

In Figure 3-8 solid and dotted lines show ω_r/ω_{Te} and γ/ω_{Te} where ($\omega = \omega_r + i\gamma$) for β_e = 0.2% (electron plasma beta), similarly dashed and long-dashed lines are β_e = 0.5%, d_e = $(k_\theta/k_{De})^2$, $T_e = T_i$ = 10 keV, q = 2, s = 1, $\varepsilon_n = L_n / R_0$ = 0.2, $\eta_{i,e}$ = 2, m_i/m_e = 1840 and ω_{Te} =

$(T_e/m_e)^{0.5}/(qR)$ is the electron transit frequency. The Figure clearly shows maximum growth rate at $d_e \approx 0.5$ which can be related to b_s through:

$$\left(\frac{k_\theta}{k_{De}}\right)^2 = (k_\theta \rho_s)^2 \frac{1}{\beta_e} \frac{T_e}{m_e c^2} \frac{m_e}{m_i} \qquad \textbf{3-58}$$

Therefore, $d_e = 0.5$ corresponds to $b_s \approx 1900$ (assuming $B_t \approx 0.7$ T and $n \approx 5\times10^{18}$ m^{-3}) showing maximization at much smaller wavelengths than expected for drift waves. Furthermore ω_{Te} in the STOR-M corresponds to a frequency of the order 1MHz indicating that a much higher frequency is expected for this mode. However, transport from this mode is shown to maximize on the order of the skin depth $(k_\theta c/\omega_{pe})^2 \sim 1$ which is similarly related to b_s:

$$\left(\frac{k_\theta c}{\omega_{pe}}\right)^2 = (k_\theta \rho_s)^2 \frac{1}{\beta_e} \frac{m_e}{m_i} \qquad \textbf{3-59}$$

Therefore maximum transport is expected for $b_s \approx 2$ and should scale as d_e with variations in T_e and B_t. Hence, by examining the dependence of the scattering data, mode classification should be possible.

The presence of ETG modes in the STOR-M is supported by both theoretical calculations and experimental measurements of a critical value for $(R/L_{Te})_c$ which is required for instability. Recent work by Dong *et al.* [49] calculates this critical parameter with gyrokinetic theory and compares with experimental results from 7 tokamaks: COMPASS-D, RTP, TCV, FT-U, AUG, Tore Supra and JET. Experimental results point to a critical parameter in the regime $(R/L_{Te})_c \approx 8 \sim 12$ which is supported by the gyrokinetic theory for relevant tokamak parameters. R/L_{Te} for the STOR-M can be crudely approximated as 5 assuming a parabolic temperature distribution or 9 using a Gaussian distribution. Therefore it is reasonable to assume that ETG type fluctuations are unstable in the STOR-M.

Chapter 4

Experiment

4.1 Introduction

The system was originally partially built by Dr. Conway in 1993 as a prototype system but was never tested. The equipment was carefully characterized and redesigned before successful operation. This section describes the equipment in its entirety including software code written to determine scattering geometries. There is also a description of initial experimental testing done using the system as an interferometer for density measurement and initial scattering data. Finally the data acquisition and electronics are presented in detail.

4.1.1 General Layout

Figure 4-1 (on the next page) is a block diagram of the final experiment setup. The RF signal launched by the klystron is split into two components: the reference arm and the transmission arm. The reference arm takes 10 dB of the launched power to the mixer to act as the local oscillator while the remainder of the signal is launched through the plasma. Scattering occurs in the "scattering volume" and produces a scattered signal that is received through the standard gain horn. The scattered signal is then mixed with the local oscillator to produce a signal that is proportional to the spectral density function.

The scattering volume is varied by adjusting the mirror angles and positions. Both mirrors are on finely adjustable ($\pm 0.5^{o}$ for the top mirror and $\pm 1^{o}$ for the bottom mount) mounts, the top mirror can be moved horizontally independent of the rest of the system and the lower mirror is moved horizontally by moving the entire system.

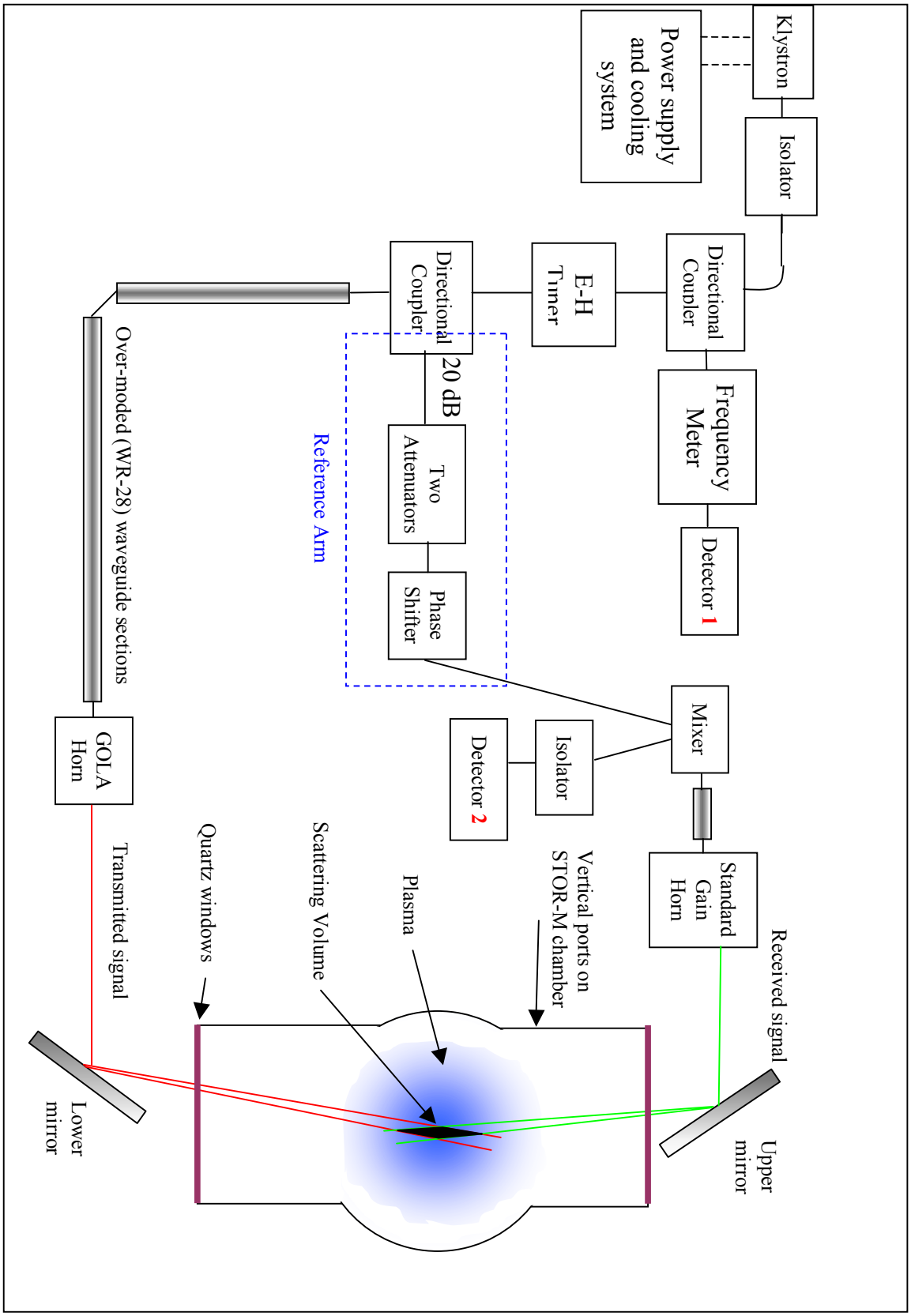

Figure 4-1: Block Diagram of the Apparatus

4.2 Equipment

4.2.1 Klystron Mounting System

The original klystron mounting system only allowed for horizontal movement of the klystron. This meant that constructing test circuits and modifying the original layout with the limited components available was impossible. A simple new mounting system was designed, built and used to allow 2-dimensional movement of the klystron in the vertical plane:

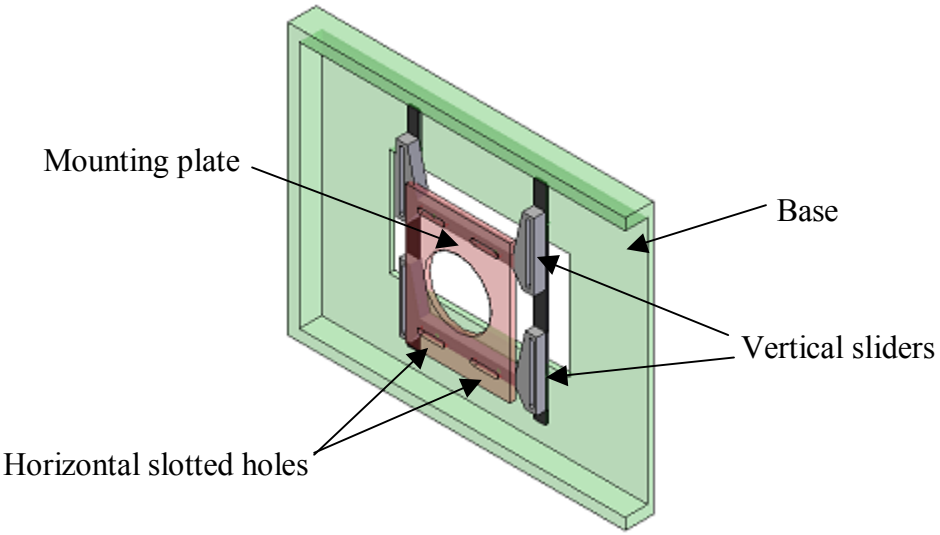

Figure 4-2: New klystron mounting system

The klystron body is cylindrical and slots into the cylindrical hole in the Mounting Plate. The mounting plate is from the original design that allowed for 1-dimensional horizontal movement through slotted holes, this movement is still allowed, but now the two vertical sliders have been added to the black rails to add another dimension of movement. The odd shape of the grey sliders is to allow maximum movement range; in the Figure the mount is moved all the way down, to move the mount all the way up the sliders have to be flipped 180^{o}. The total thickness of the rails, sliders and mount are exactly the same as the thickness of the original mounting design.

Modifications were also made to the klystron cooling water lines to maximize available motion within the limited size of the rectangular hole in the base. Using this new design, modifications to the microwave circuit and test circuits could be easily constructed and then the klystron moved to allow attachment of the source.

4.2.2 Klystron and Power Supply

The microwave signals are generated by a Varian CW EIO (Continuous Wave Extended Interaction Oscillator) VKT2427N1 klystron [50] capable of producing up to 13 W at 140 GHz (≈ 2 mm), with a beam current of 70 mA and cathode voltage of 9.7 kV. EIO klystrons are similar to conventional klystrons and operate by passing a confined electron beam through a series of resonant RF cavities. The cavities cause velocity bunching of the electrons, which interact with the RF output in the last cavity to generate amplification. Usually amplification is achieved through multiple cavities in a generic multi-stage klystron amplifier. However, due to design limitations in the mm regime [51], a single cavity is used with a ladder-like structure of smaller cavities to provide RF amplification:

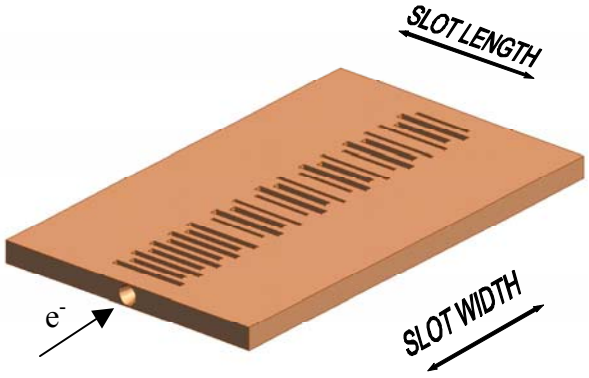

Figure 4-3: Extended Interation Oscillator (EIO) ladder structure, courtesy of Varian Canada [51]

The slots act as cavities for velocity bunching. Slot length and width are key design parameters. The klystron is powered by a Varian VPW2889E5 [52] power supply and cooled with a closed de-ionized water system that circulates around the body of the klystron. The water system is electrically insulated from the system and is powered by a FloJet 2100 electric pump and cooled through a forced air radiator. Electrical insulation means the cooling system can safely have its own ground and run independent of the

klystron. An external interlock from the klystron power supply is connected to a pressure sensor on the input cooling line, causing the klystron to be shut down in the event of a failure of the cooling system. 70 mA across 9.7 kV is 680 W, of which only a maximum of 13 W is converted to RF power; therefore failure of cooling without klystron shutdown would have catastrophic results. The klystron power supply is also fitted with several other internal and external interlocks that ensure the klystron shuts off if any currents or temperatures exceed operational values, or if any high voltage lines are exposed. An extra thermal couple is also attached to the klystron body for independent measurement. Under normal operating conditions the temperature would generally rise from 21^{o}C to 37^{o}C.

The klystron and power supply were rigorously tested before initial operation as they had been inoperative for about 10 years. The power supply was subjected to open voltage and full loading tests using various high power resistors, the interlocks were also individually tested and the power supply was 100% operational. The klystron was tested using a custom testing procedure specifically provided from the manufacturers. This tested the insulation, cathode, filament, anode and high voltage lines. The final test was to build a simple circuit and measure the power output. The klystron was attached to a water cooled load, and a directional coupler and attenuators were used to direct -35 dB of the signal to the FD detector (see Section 4.2.3). Figure 4-4 shows the klystron power characteristics:

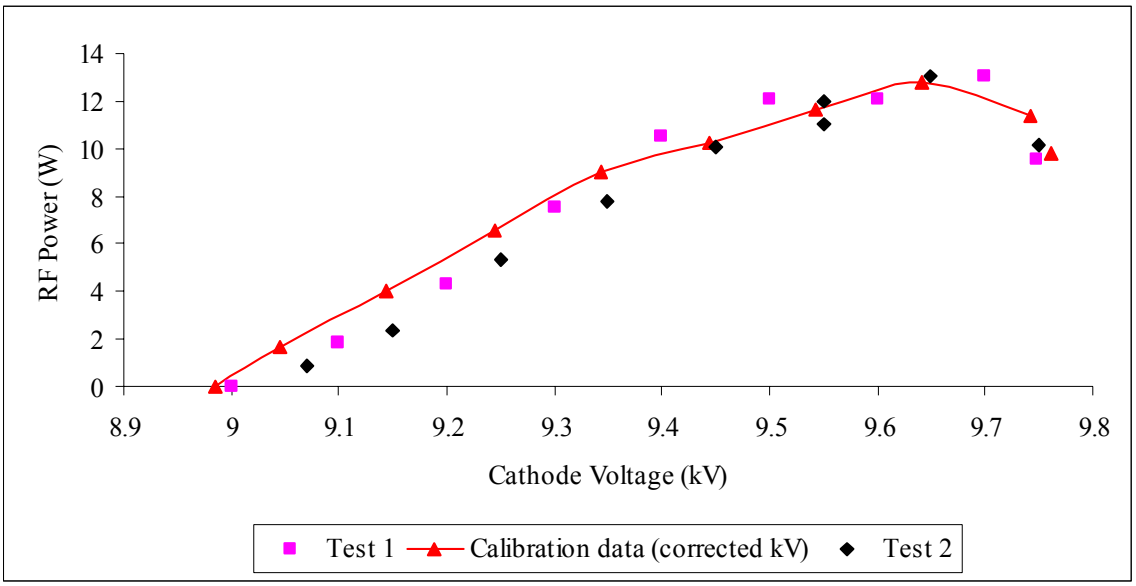

Figure 4-4: Klystron characterization results comparing in house testing to the calibration data.

'Test 1' and 'Test 2' correspond to different arrangements of components to build the test circuits. The voltmeters on the klystron were found to be out of calibration, therefore the calibration data was corrected to account for this.

4.2.3 Detector Diodes

Both diodes use Schottky-Barrier GaAs diodes that operate in a square law regime $V_{\text{out}} \propto P_{\text{RFin}}$. As depicted in Figure 4-1, "Detector 1" is a TRG Series 965D diode detector and "Detector 2" is a FD Series diode detector from Pacific Millimeter. The FD detector was purchased for this experiment and came with calibration data for 0-4 mW (as shown in Figure 4-5), the TRG detectors appeared to be at the end of their shelf life, as depicted by the following test:

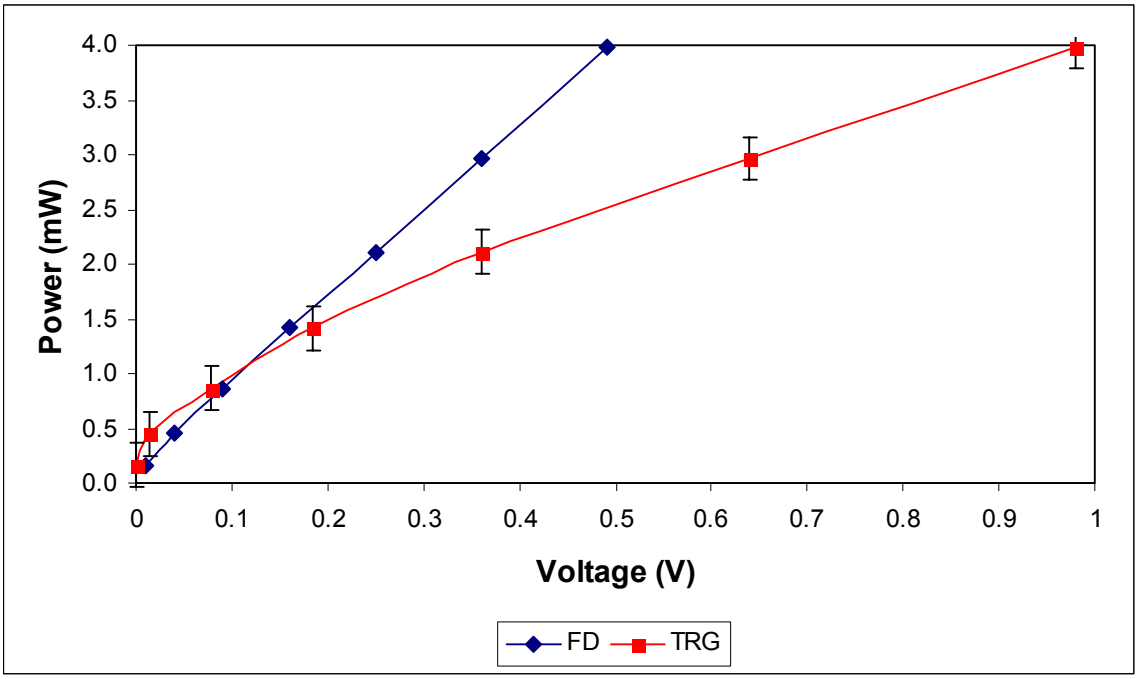

Figure 4-5: Microwave detector diode characteristics

The FD data was provided by the manufacturer, the TRG data was measured by constructing a simple microwave circuit: The klystron was attached to a water cooled load, a directional coupler was placed in line and used to direct a known fraction of the power to the TRG detector.

Clearly the TRG detector has a non-square-law response and therefore is used in position 1 to monitor the reflected signal. This is required to ensure that the system is well matched and that no unwanted reflections occur in the system, therefore the atypical response of the diode is not a problem. The FD detector has a relatively larger sensitivity and follows a square-law dependence on power and is used to capture the scattered signal. Due to the age of the TRG detector it has ceased functioning accurately with lower input powers. It is possible that the FD detector follows a square law relationship for higher powers, but 4 mW was the maximum power available to the manufacturer in the 140 GHz band. The manufacturer also hypothesized a maximum safe input power into the FD detector of about 10 mW. Throughout this experiment the incident power was kept below 4mW and therefore within the calibration data.

4.2.4 Over-Moded Waveguides

Although WR-8 waveguide is best suited to 140 GHz (see Section 3.1) and is used for the majority of the waveguide circuit components, it is not the most efficient size for transmission over distances of the order of a meter. Attenuation in a waveguide is mainly due to ohmic losses from image currents in the waveguide walls which have a finite surface resistance [33]:

$$\alpha_c\left(dB/m\right)=\frac{20\sqrt{\pi\varepsilon_0}\left(bc^2+2a^3f^2\right)}{a^2b\sqrt{f\sigma\left(4a^2f^2-c^2\right)}\ln\left(10\right)} \qquad \textbf{4-1}$$

where a and b are the waveguide width and height respectively, f is the frequency (140 GHz), σ = 5×10^7 S/m is the wall conductivity (standard coin silver[35]) and ε_0 is the usual permittivity of free space. WR-8 waveguide (0.08"×0.04") has α_c = 3.7 dB/m and WR-28 (0.28"×0.14") α_c = 0.7 dB/m. This means the 3.46m of WR-28 waveguide in the system causes a 2.4 dB attenuation, as opposed to WR-8 which would give an attenuation of 12.8 dB over the same distance.

Although these overmoded waveguides can allow different modes to propagate, the klystron is a very narrowband device (+/- 0.5 GHz) and so the activation of other modes is not expected. Furthermore, overmoding is only done on long straight segments and not for complicated components such as diodes, frequency meters, attenuators, etc… where excitation of extra modes is possible. Also, any extra excited modes will be attenuated when transitioning back to the WR-8 waveguide. In Figure 4-1, the waveguides are all WR-8 unless labeled specifically as WR-28.

4.2.5 Quartz Windows:

Each of the microwave components introduces a small insertion loss into the system which is specified on the relative specifications sheets. However, losses due to reflection off the quartz windows were unknown. This loss was calculated using the index of refraction and thickness of the quartz windows and is shown below for varying angles of incidence:

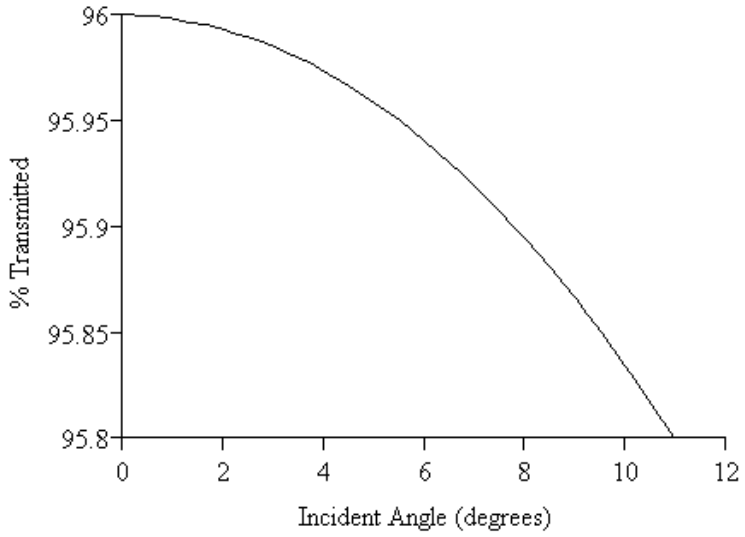

Figure 4-6: Transmission losses as the microwaves pass through the quartz port windows

Clearly the quartz windows do not cause large unwanted reflections or attenuation.

4.2.6 Grounding

The apparatus is operating in an electrically noisy environment (due to the large changing fields and currents generated by the tokamak discharge); therefore care must be taken to avoid grounding loops in the system. A loop in the grounding system provides an ideal source for an induced *emf* which results in a large noise pickup, and can also damage the sensitive diodes and diagnostic equipment. To avoid loops the system has only one grounding point through the klystron power supply (the cooling system has its own ground but is electrically insulated from the system). This means that all data acquisition and attached equipment is floating; power to other equipment is provided through isolation transformers.

4.2.7 Microwave Horns

The radiation patterns of the two horns are presented in Figure 4-7 and Figure 4-8.

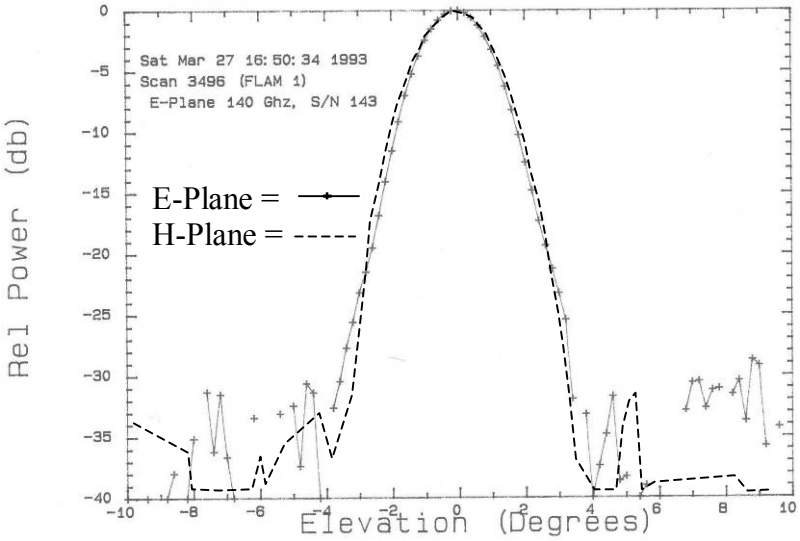

Figure 4-7: Gaussian Optics Lens Antenna (GOLA) radiation pattern

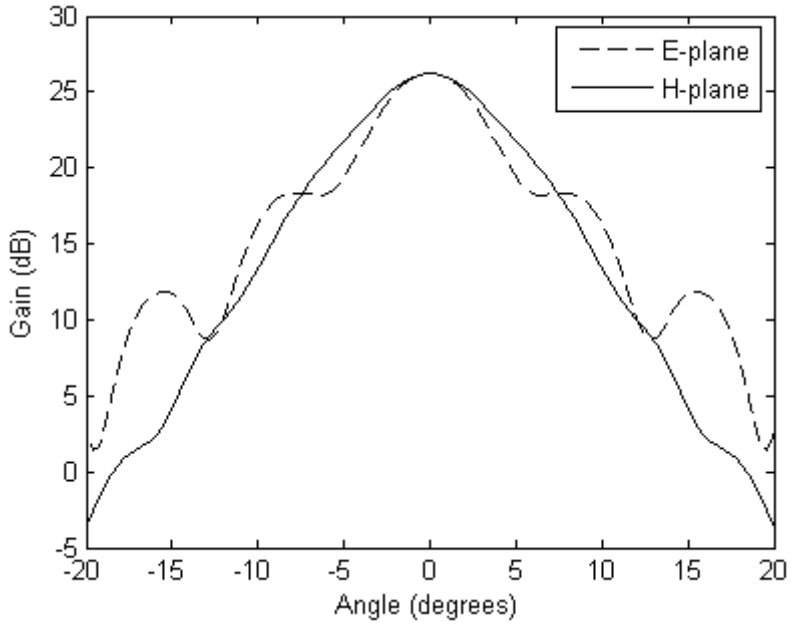

Figure 4-8: Standard gain horn radiation pattern

The radiation pattern for the GOLA lens was measured by the manufacturer [53]; the pattern for the Standard Gain Horn was calculated using the model from *Balanis* [54] written into a Matlab™ code. The Matlab™ code was checked for correctness against

models in *Balanis* and *Ghandi* [55]; furthermore, the only information available on the Standard Gain Horn was its gain of 25 dB, the Matlab™ code predicted 27 dB. Appendix 2 shows the full 3-dimensional radiation pattern of the horn calculated using Matlab™. Introducing random errors ($\pm 5\%$) through a Monte Carlo simulation in the Standard Gain Horn dimensions produced negligible changes in the radiation pattern. This is important as it means physical defects or measurement errors in the Horn will not drastically change the radiation pattern.

The GOLA Horn is used for the transmission signal as it produces a much narrower beam than the standard gain horn. Ideally more effective GOLA horns would be used for the transmission and reception of the signals; however, these devices are highly specialized and require 8 to 12 months to receive at considerable cost and therefore only the available GOLA was used.

4.2.8 Other Components:

- Directional Couplers (Alpha Series 561 and 559 [56]): These devices are used to divert fractions of RF power to secondary circuit branches. Two waveguides are attached parallel to each other with small holes connecting the two guides. The holes act as RF sources and are designed to transmit a certain fraction of the power in phase at the exit port of the device.
- Variable Attenuators (Alpha Series 520 [56]): A resistive film is lowered into the centre of the waveguide parallel with the electric field. The power absorbed by the film is proportional to the area of the film, therefore by raising and lowering the film, variable attenuation can be achieved.
- Ferrite Isolator (Alpha Series 112 [56]): These devices permit only unidirectional wave propagation and are typically placed after sources to prevent reflected signals from returning to the source and causing frequency pulling and damage. The non-isotropic ferrite used rotates the reflected signal by 90^{o} to align it with a resistive film that is parallel to the reflected electric field but perpendicular to the transmitted electric field.

- Phase Shifter (Alpha Series 525 [56]): Similar to the variable attenuator, but insert a dielectric film into the waveguide. This introduces a different medium into the waveguide and changes the TE_{10} wavelength, and thus alters the phase of the signal.
- Frequency Meter (Alpha Series 550 [56]): An adjustable resonant cavity is attached to the side of the waveguide. When resonance is achieved, a drop in the transmitted power can be measured. The size of the cavity at resonance determines the frequency.
- E-H Tuner (Alpha Series 620 [56]): Two plungers are attached to the waveguide, one parallel to the electric field the other parallel to the magnetic field. By adjusting the plunger height the series and parallel reactance of the tuner can be modified. Thus one can match the impedance on each side of the tuner and prevent unwanted signal reflections from the microwave circuit.
- Mirrors: The two mirrors are highly polished aluminum to provide a clean reflection. Polishing was done overnight on a precision rock polisher courtesy of the Geology department. This not only ensured a smooth surface but also guaranteed a flat surface.

4.3 Scattering Graphical User Interface (GUI)

From Figure 4-7 and Figure 4-8 the FWHM (Full Width Half Maximum) of the horns are approximately 2^{o} and 6^{o} respectively. Using this information and measurements taken from the system, a graphical user interface (GUI) was written in Matlab™ to calculate the scattering volume and scattering wavevector based on the mirror angles and positions; this information is essential in order to calculate absolute values of $S(\vec{k},\omega)$ (see section 5). A sample output from this program is shown in Figure 4-9.

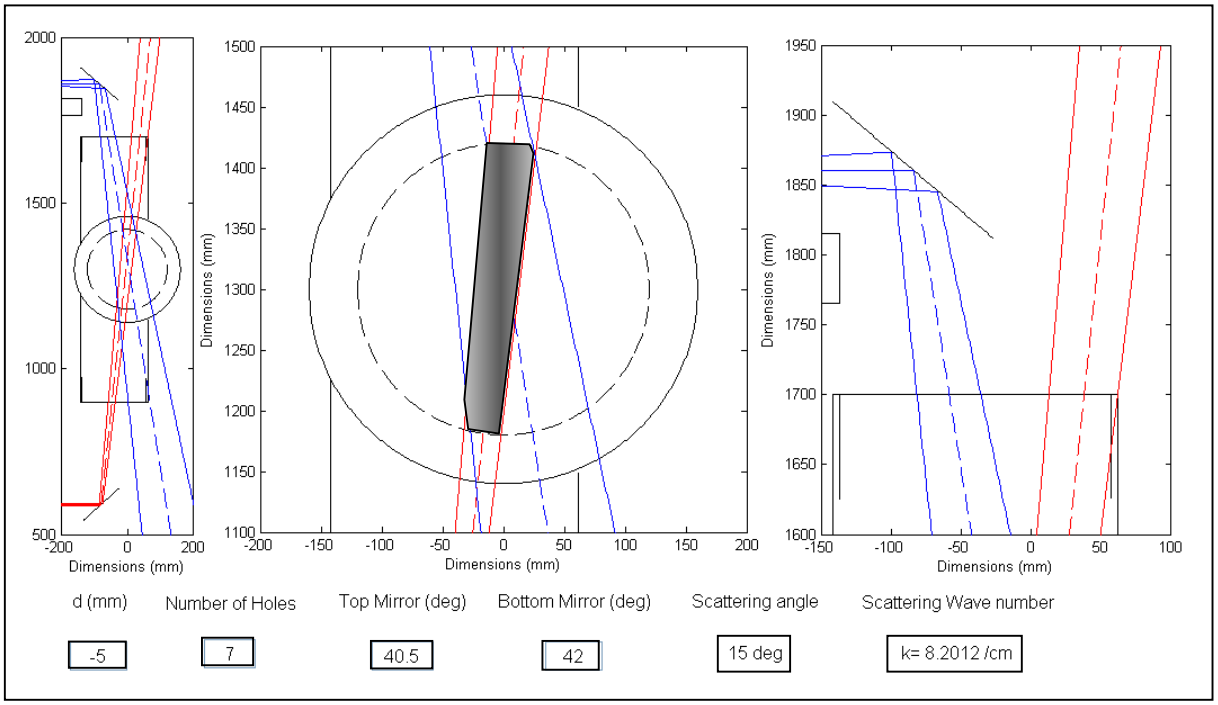

Figure 4-9: Scattering geometry GUI, shaded area is the scattering volume

Table 4-1 describes the variables in the GUI:

Quantity	Description
d (mm)	Horizontal displacement of the top mirror. 0mm is vertically aligned with the bottom mirror; -5mm is 5mm outboard.
Number of Holes	The entire system is on rails and can be slid horizontally outwards and locked in place through 13 evenly spaced holes with ½ hole resolution
Top Mirror (deg)	Angle between the mirror and horizontal, 45° creates a vertical reflected beam.
Bottom Mirror (deg)	Same as 'Top Mirror'

Table 4-1**:** Matlab™ GUI variables used to define the scattering volume geometry

The graph on the left in the GUI is a small scale cross section of the vertical port of the tokamak; the dotted circle represents the limiter radius, lines from the bottom define the transmitted beam and lines from the top represent the received beam. The graph in the middle is a magnified view displaying accurately the scattering volume (shaded area

added for reader emphasis). The right most graph is used to determine the location of a mask of RF absorbent to absorb the un-scattered signal and prevent unwanted reflections. The user can vary the mirror angles and positions and quickly view the resulting scattering geometry in order to determine optimum scattering volumes.

One must consider the importance of slight errors in the beam angles and positions. To examine this, a Monte Carlo simulation was run varying the input parameters that define the scattering volume and recording the change in $\left|\vec{k}\right|$. Normal distributions with $\pm 5\%$ error were used for all the parameters for an overestimate of the error:

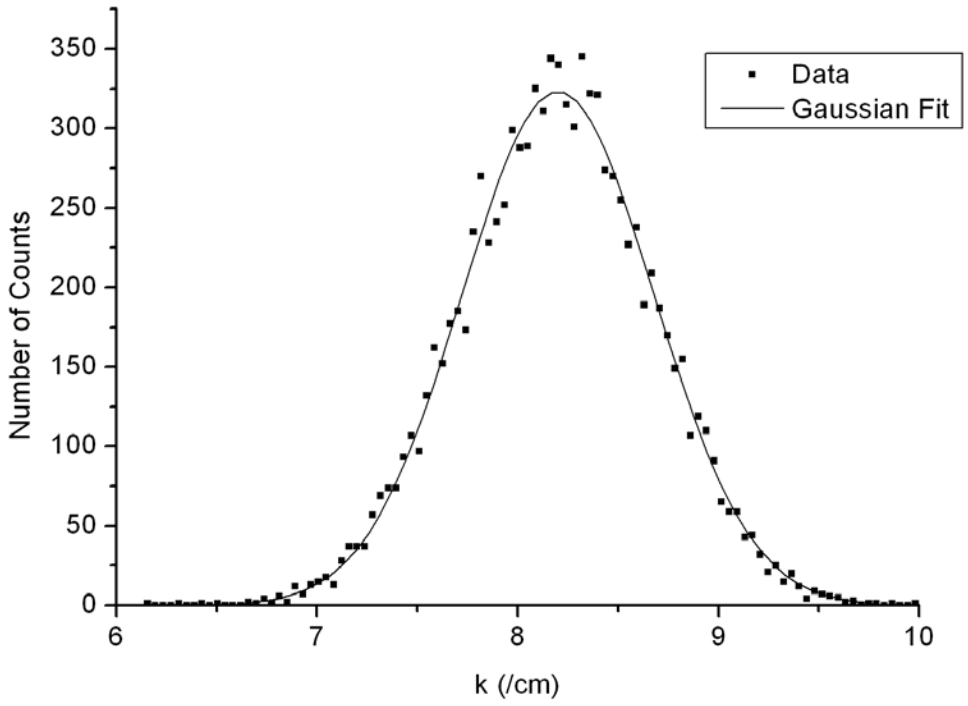

Figure 4-10: Monte Carlo simulation to determine errors in the scattering vector.

From the Gaussian fit $\left|\vec{k}\right| = 8.2 \pm 0.5$/cm with 5% errors in the scattering volume positioning, demonstrating that *k* is fairly insensitive to the physical setup. In practice, the mirror positioning was very precise ($\pm 1^{o}$ for the bottom and $\pm 0.5^{o}$ for the top) and a 1% error margin provides ± 0.1 /cm resolution in *k*-space.

A more important source of error is from the finite width of the scattering volume. This means that scattering from multiple $|\vec{k}|$ values within the volume is possible. An algorithm was implemented to calculate a $|\vec{k}|$ resolution assuming constant power within the -3 dB lines of the scattering and transmitted beams. It was found that the scattering volumes contain $|\vec{k}| \pm 1$/cm assuming scattering occurs along the -3 dB boundary lines. As the power in the beams is Gaussian, a Gaussian distribution of k acceptance gives $|\vec{k}| \pm 0.4$ /cm which is the k resolution of this system.

4.4 Initial Testing

4.4.1 Interferometer

The first experimental phase of this project was to run the scattering system as a single channel interferometer to test the general operation of the equipment. This requires arranging the mirrors at 45^{o} to launch the RF signal straight through the plasma. In this orientation the scattering system becomes a typical Mach-Zehnder [57] type interferometer with similar operating characteristics as the 4 mm density interferometer (see Section 2.2.5):

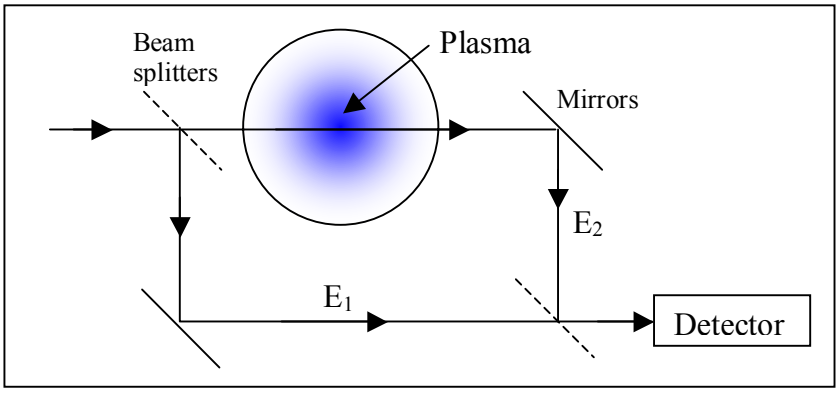

Figure 4-11: Generic Mach-Zehnder type interferometer

In this arrangement great care had to be made to ensure that the detector never experienced more than 4 mW of incident power (maximum recommended input power [58]). This was achieved by determining the total power at each stage of the circuit from

the insertion losses of each component as specified on the relative datasheet. Alignment was initially achieved by aiming a He-Ne laser down the lower overmoded waveguide section and aiming for a paper target covering the standard gain horn. Each mirror is on a rotating mount and has three spring loaded set screws that allow fine three-dimensional adjustment of the mirrors. These were adjusted until the laser beam was directed into the standard gain horn (the top mirror was positioned vertically above the bottom mirror). Final adjustment was made under low RF power; each mirror was carefully adjusted until maximum power was delivered to the detector.

In performing the interferometer measurements, it was discovered that the power transmitted through the tokamak (with and without a plasma discharge) was much lower than simulations predicted. After rigorous testing and consultation with external engineers [58] it was determined that a ferrite circulator (part of the original microwave circuit) was malfunctioning. A replacement circulator is a highly specialized component and would take 3 months or more to build at great expense; therefore the system was modified to remove the circulator using the components available and was used in the configuration shown in Figure 4-1. Using the same equations described for the 4mm system, this phase of the experiment was successfully completed. The results from a typical shot are shown:

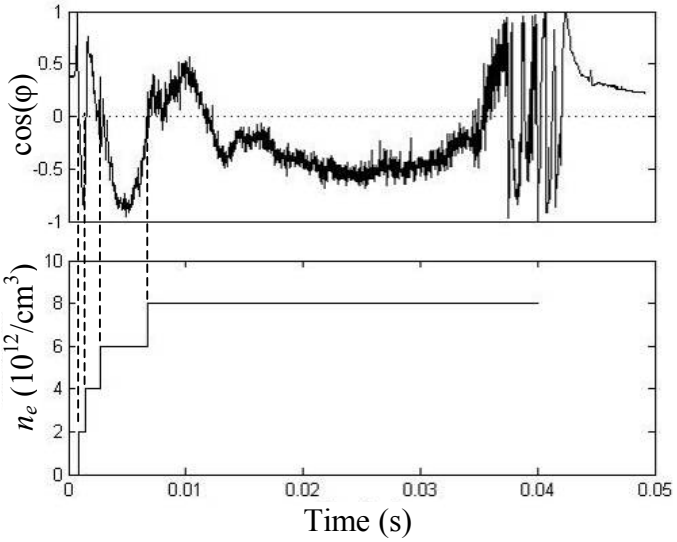

Figure 4-12: Results from a typical discharge showing the fringe signal and resultant density profile using the system as an interferometer

The step size in this case is exactly quadruple that of the 4 mm system, and is $2.32\times10^{12}/cm^3$ (frequency is doubled and phase resolution is doubled). Also, saddle points cannot be detected and therefore the sign of $d\varphi/dt$ (rate of change of the phase difference between E_1 and E_2 from Figure 4-11) must be assumed. Nevertheless, the fringe signal clearly shows correct operation of the equipment and electronics.

At first the 'noise' in the fringe signal was considered to be random. However, when the signal was collected at a higher sampling rate (1 MHz) and analyzed, there appeared to be a definitive global oscillation in the line averaged density:

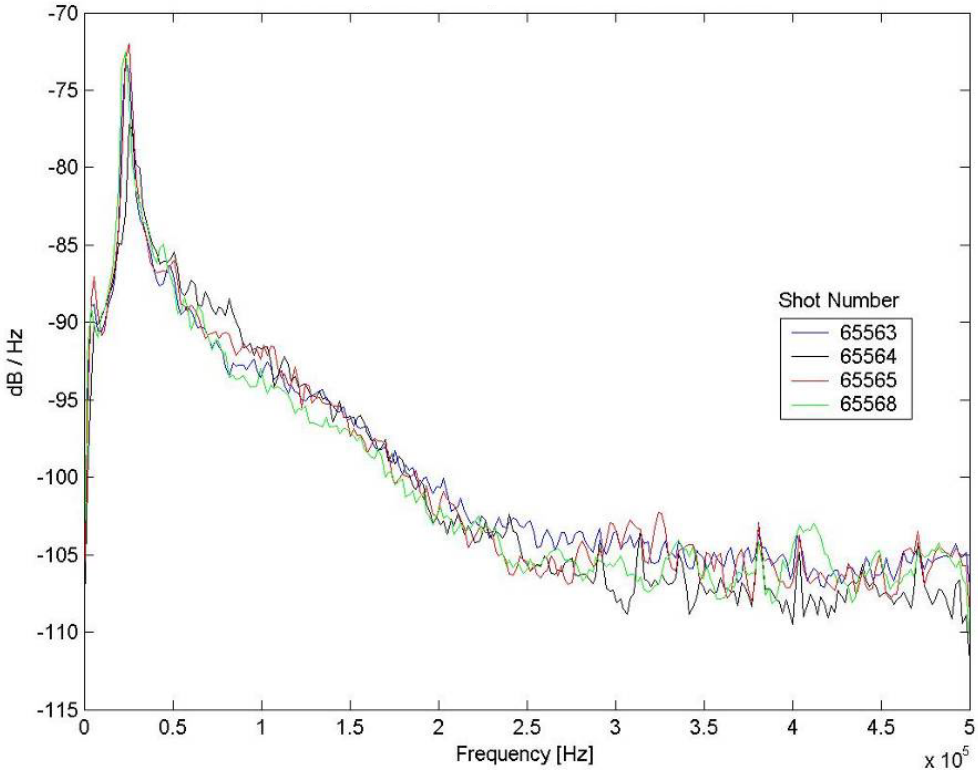

Figure 4-13: Global density oscillation observed in the fringe signal

Figure 4-13 shows a clear peak in the global oscillations at around 30 kHz. This spectral density function is comparable to recent measurements with Langmuir probes in the plasma edge region of the STOR-M [59], and could be related to macroscopic MHD instabilities in the plasma. Further investigation of this signal could be studied by scanning the plasma column with the interferometer beam and comparing to MHD

signals. Nevertheless, this data indicates correct operation of the experimental equipment with no evidence of excessive noise or incorrect operation of any of the electronics.

4.4.2 Scattering

The GUI interface was used to set the equipment for $\left|\vec{k}\right| \approx 8$ /cm as shown in Figure 4-9.

8 W of RF power was launched through the plasma and the frequency spectrum of the collected signal calculated:

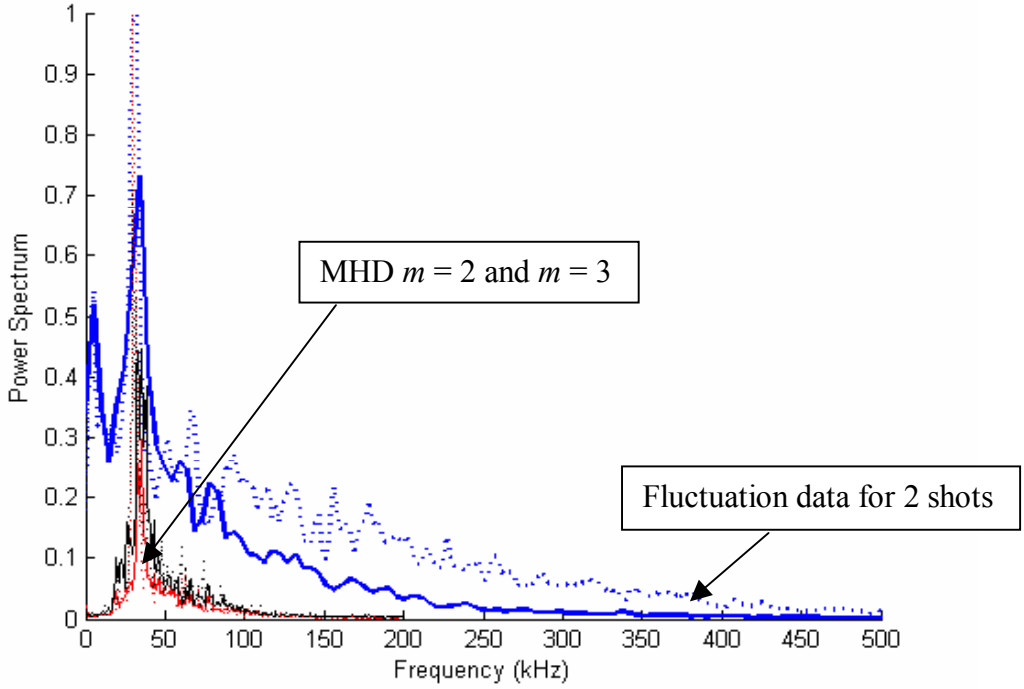

Figure 4-14: Initial spectral density fluctuation data showing a strong correlation with MHD signals

The frequency spectrums are calculated using Welch's method [64] (see Section 5.2). The MHD data is collected at 400 kHz over 10 ms and the scattering data is collected at 1 MHz for the same time period. The signals are then split into eight equal periods, each period is Fourier transformed, and then the average of the frequency spectra is displayed.

It was found that the scattering signal was inundated with low frequency coherent modes (≈ 30 kHz) that aligned exactly with the frequency spectrum of the MHD signals. It is hypothesized that the macroscopic MHD fluctuations were modulating the number of

electrons ($N_e \rightarrow N_e e^{i\omega_m t}$) inside the scattering volume, where ω_m is the MHD frequency. Therefore the detected scattering signal (Equation 3-16) is modified:

$$P_s\left(\vec{k}\right) = \frac{\gamma_e^2 P_i \Omega}{A}\left(N_e e^{i\omega_m t}\right)\left|\hat{s}\times\left(\hat{s}\times\hat{E}_{i0}\right)\right|^2 \int_{-\infty}^{\infty} S\left(\vec{k},\omega\right) d\omega \qquad \textbf{4-2}$$

This phenomena usually warrants a minor remark in the literature [16][17] as data is only collected during periods of 'lower MHD activity'. This effect is most likely emphasized in the STOR-M due to the relatively large size of the scattering volume compared to the plasma size. This hypothesis is supported by the chord averaged $\tilde{n}_e$ measurements shown in Figure 4-13.

Two possible techniques to separate this MHD contamination of the density fluctuations are: H-mode operation or filters. H-mode operation is when the plasma is temporarily placed in an improved confinement state, which can be achieved through electrode biasing [21] in the STOR-M, but is difficult to reproduce, especially for the relatively large number of shots required for scattering. As the frequency of interest is much higher then the 30kHz signature, a high-pass filter ($f_c \approx 130$ kHz) is a more effective solution. Furthermore, by restricting data analysis to the 5 ms of flat I_p ensures minimum MHD activity.

Once the signal filters were in place (see next Section), scattering data was collected at various launching and local oscillator powers and density levels to confirm the correct dependence of the scattering signal with theory. $S(\vec{k}, \omega) \propto 1 / n_e$ and $S(\vec{k}, \omega) \propto 1 / P_i$ was measured as expected.

4.5 Data Acquisition

The FD detector has a 50 Ω SMA connector (SubMiniature version A) output for measuring the diode voltage. Ideally this output would be matched with a 50 Ω load for measurement; however, the diode is unable to drive a 50 Ω load due to low current output limitations. Therefore the scattering signal must be collected over a high impedance load. To handle such a large impedance mismatch [60] requires $L \ll \lambda$, where L is the

transmission length and λ is the signal wavelength. A high input impedance buffer op-amp was connected to the SMA connector with transmission length $L \approx 7$cm, corresponding to $f \approx 3$ GHz (if $\lambda = 7$ cm), hence $L \ll \lambda$ is satisfied as long as the frequencies measured are below 3 GHz.

This block diagram represents the data acquisition system:

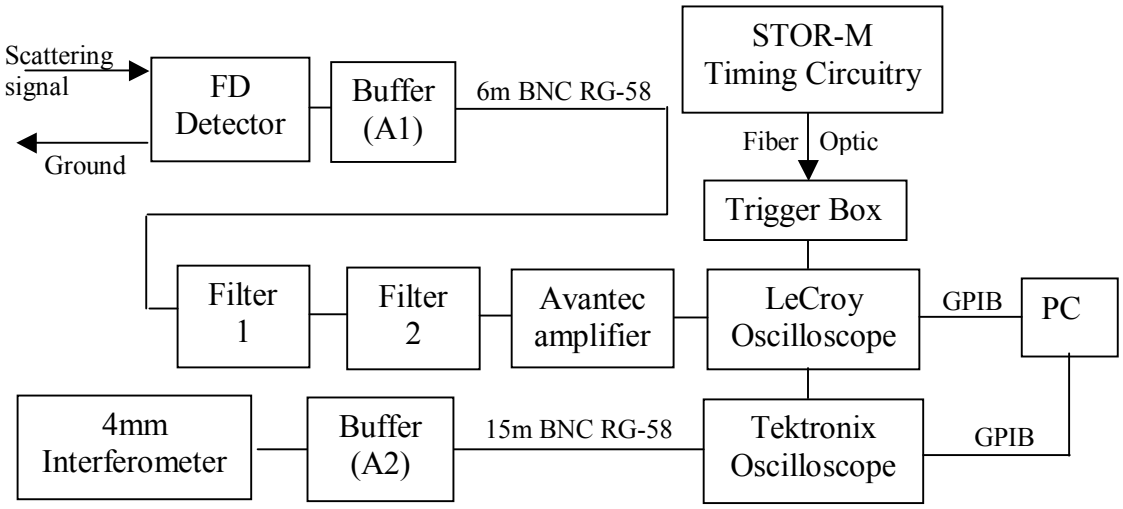

Figure 4-15: Block diagram depicting the data acquisition layout.

Buffer A1 is a custom built buffer (see section 4.5.1), Filter 1 is 28 nF in series and 50 Ω in parallel (f_c = 115 kHz), Filter 2 is 22 nF in series onto the 50 Ω input (f_c = 145 kHz) of the Avantec. The Avantec amplifier is a solid state Model AWL-500B amplifier with a band-width of 0.001 – 500 MHz and a nominal gain of 25 dB (measured). The LeCroy oscilloscope is a 9314M Quad channel 300 MHz digital oscilloscope (8-Bit) [61] with a 50 Ω adapter for impedance matching. The ground connected to the diode is through the waveguide walls, which are connected to the body of the klystron.

The 4 mm interferometer was designed as a floating system, and therefore also takes its ground from the klystron through the data acquisition system. Buffer A2 is a 4 channel unity gain buffer built in house with LM6161 operational amplifiers. The Tektronix oscilloscope is a TDS 2014 100 MHz 8-bit 4 channel digital scope and also is used in conjunction with a 50Ω adapter.

The scopes are triggered by the main timing system for the STOR-M at 41 ms (see Figure 2-2) through a fiber optic cable (necessary to separate the control system ground from the data acquisition ground). The trigger box converts the optical signal to an electrical impulse to externally trigger the scopes. A Matlab™ code was designed to simultaneously collect and display the data from the two oscilloscopes. Density calculation from the fringes was done immediately as the density signal is an important routine diagnostic for monitoring the discharge. The file names of the saved data follows a convention based on storage device, shot number and date.

4.5.1 Analogue Amplifier

The design requirements for the buffer amplifier are:

- Low power consumption (allows for battery operation to minimize noise and remove the need for power cables and a power supply)
- Broadband frequency response (0 → 500 kHz)
- Discreet variable gain (for predetermined amplification of the signal as required for varying scattering geometries)
- Adjustable null offset (to remove DC offset from local oscillator power, allows full range of operational amplifier to be utilized)

The biggest challenge was removing the DC offset as new high bandwidth operational amplifiers no longer have null offset attachments common with older IC's [62]. The technique used was to provide the amplifying operational amplifier with a virtual ground that could be floated to offset the local oscillator DC power input. A conventional voltage divider was considered, however this makes discrete variable gain very difficult, as the different gain settings require different resistors and variable resistors to correctly float the virtual ground. The solution was a novel design using a voltage follower in conjunction with a potential divider. The circuit diagram for the buffer is shown:

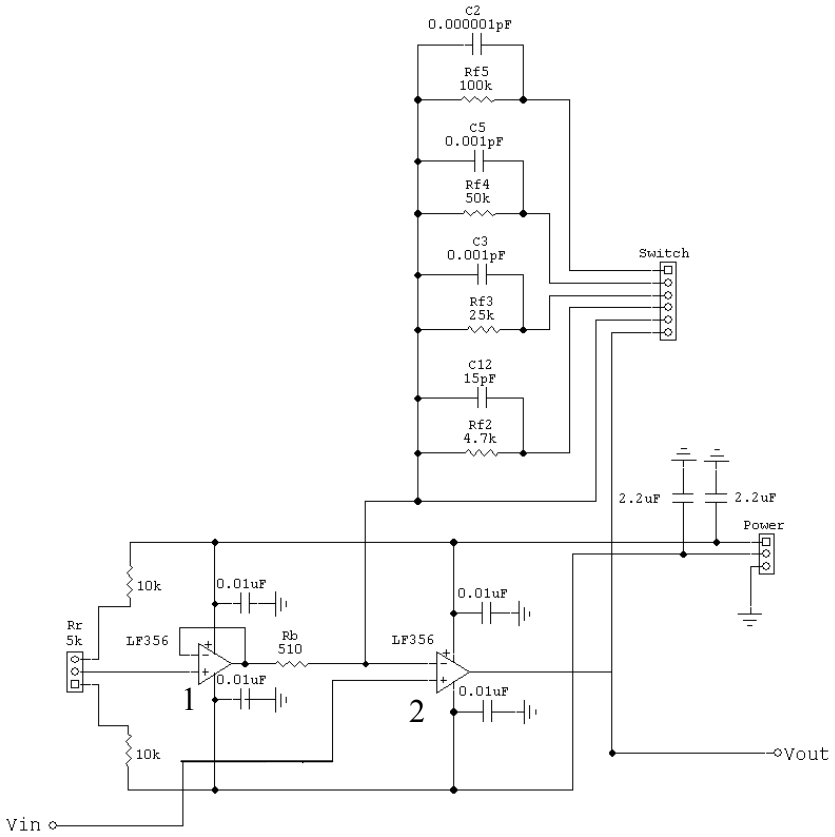

Figure 4-16: Buffer circuit used to amplify the signal from the detector to the data acquisition

'Rr' is a 5 kΩ 10-turn trimpot, 'Switch' is a multipole switch used to connect different capacitor and resistor combinations across the LF356 operational amplifier and 'Power' is ±9 V supplied by Ultralife® Lithium Power Cells. Operational amplifier '1' acts as a non-inverting voltage follower and can generate a stable floating ground for operational amplifier '2'. By using an operational amplifier, the voltage output is independent of the current drawn from '1'. Operational amplifier '2' is configured as a non-inverting amplifier with various gains achieved by varying the feedback resistance. The capacitors across the feedback resistors are necessary to maintain stable amplification [63]. National LF356 [63] operational amplifiers were used for their high input impedance (10^{12} Ω), low power consumption (~10mA) and high unity-gain bandwidth (LF356 = 5 MHz, LF357 = 20 MHz). The second operational amplifier had to be switched with a LF357 for higher gain operation (the LF356 bandwidth was too small and the LF357 was unstable at low gains).

The circuit of Figure 4-16 was designed and modeled in Circuit Maker 6 before being constructed on a printed circuit board (PCB). The PCB was then mounted in a small aluminum box for electrical shielding along with the 9V batteries. The system was tested according to Figure 4-15 with the diode replaced by a Hewlett-Packard 3312A Function Generator (0→13 MHz):

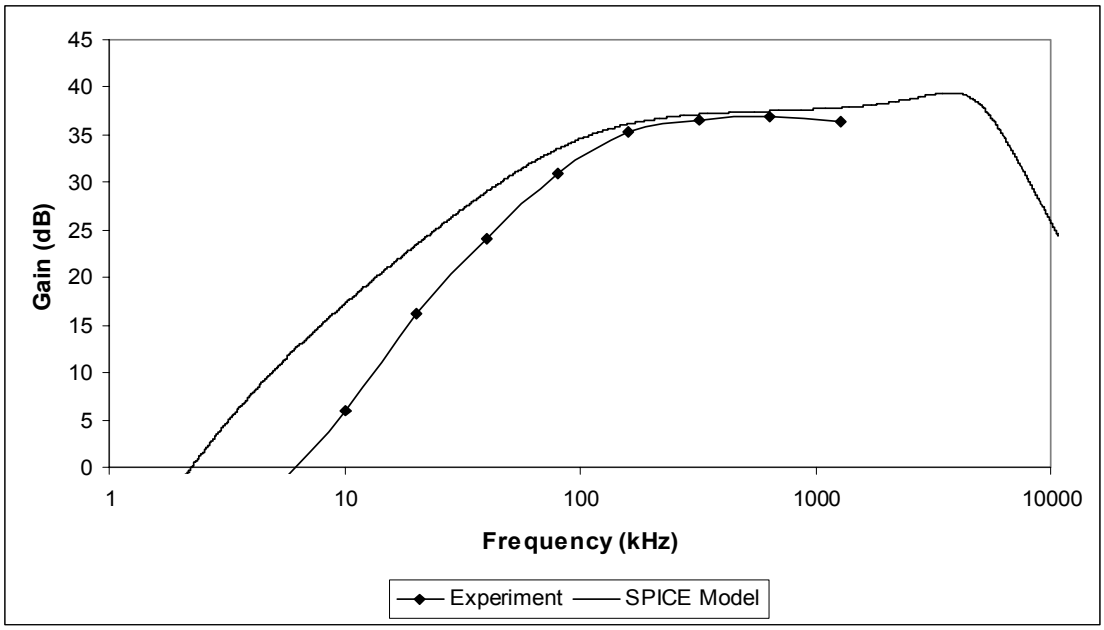

Figure 4-17: Operational amplifier characterization.

The SPICE (Simulation Program for Integrated Circuits Emphasis) model was calculated by recreating the data acquisition pipeline in Circuit Maker 6, modeling the Avantec amplifier as an ideal amplifier based on its measured performance. From Figure 4-17 one can see reasonable agreement between experiment and theory. The filter response is essential as convolution with the measured power spectrum allows retrieval of some of the low frequency data.

The original design used LM7171 operational amplifiers which have exceptional unity-gain bandwidths of 200 MHz. However, despite careful PCB construction the electronics were very unstable and prone to go into oscillation. It is believed that the diode capacitance was too great for these operational amplifiers and made them unstable. In comparison, the LF356/357 amplifiers are specifically tolerant of high capacitance inputs.

Chapter 5

Data Analysis

5.1 Introduction

The raw data collected from the experiment must be carefully analyzed before useful information can be extracted. The first step is to account for the experimental geometry and convert the data to the correct scaling and units. The data is then organized according to the varying operating regimes used throughout the experiment. Finally the data can be processed and organized for examination.

5.2 Measurements

Equation 3-16 can be rewritten to relate to the geometry of the experiment [17]

$$\frac{\alpha_S P_S\left(\vec{k},\omega\right)}{\alpha_T P_T}=\frac{\gamma_e^2}{4\pi w_T^2}\left(\frac{w_R^2}{D_T^2}\right)N_e S\left(\vec{k},\omega\right) \qquad \textbf{5-1}$$

where w_R is the width of the receiving beam in the scattering volume, w_T the width of the transmitted beam in the scattering volume and D_T is the distance from the scattering volume to the receiving horn. $\alpha_{S,T}$ are attenuation constants for $P_{S,T}$ respectively, that take into account losses from the microwave circuit (waveguide losses, component losses and transmission losses); $\alpha_S \approx$ -3.4 dB, $\alpha_T \approx$ -5 dB. Therefore $S(\vec{k},\omega)$ can be determined from:

$$S\left(\vec{k},\omega\right)=\frac{\alpha_S F\left(\omega\right)^{-1} P_S\left(\vec{k},\omega\right)}{\alpha_T P_T}\cdot\frac{4\pi w_T^2}{\gamma_e^2}\left(\frac{D_T^2}{w_R^2}\right)\frac{1}{\overline{n}_e\cdot\text{Volume}} \qquad \textbf{5-2}$$

$$\left|P_S\left(\vec{k},\omega\right)\right|^2=\text{Pwelch}\left[P_{FDS}\left(\vec{k},t\right)\right] \qquad \textbf{5-3}$$

Where $F(\omega)^{-1}$ is the inverse filter response, $\bar{n}_e$ is the chord averaged density, 'Volume' is the scattering volume ($N_e \approx \bar{n}_e \cdot \text{Volume}$), $P_{FDS}(\vec{k},t)$ is the raw scattering signal and 'Pwelch' calculates the power spectra density through Welch's method [64]. This technique involves sectioning the data into overlapping units. These individual sub-units are then Fourier transformed using a standard Hamming window. The collection of transforms are then averaged to produce a final Fourier transform of the original signal. Fourier transformation with this method was performed using the built-in 'Pwelch' function of Matlab™.

The scattering volume is determined from the intersection points between the transmitted and received beams, or their intersection with the limiter. Figure 5-1 shows the intersection points as circles for $|\vec{k}|$ = 8 /cm:

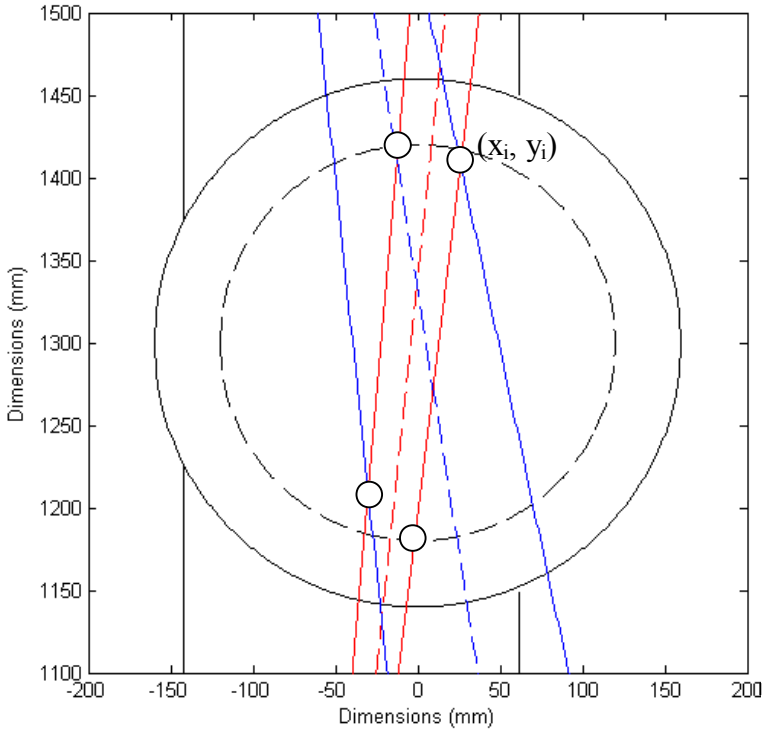

Figure 5-1: Scattering volume diagram depicting volume vertices.

The 2-dimensional area of the volume is determined from Gelder's method [65], a common technique in computer graphics

$$A = \frac{1}{2}\left[(x_2 - x_0)(y_3 - y_1) - (x_3 - x_1)(y_2 - y_0)\right] \quad \textbf{5-4}$$

'A' is the area and x_i, y_i are the Cartesian coordinates of the quadrilateral vertices. Gelder's method does not account for $x,y < 0$, therefore the vertices of the scattering volume are translated to ensure positive coordinates. The quadrilaterals chosen do not cover the entire area but are a close enough approximation. The volume can be approximated as:

$$Volume = \frac{1}{2}\pi\frac{w_T}{2}\cdot A \qquad \textbf{5-5}$$

where w_T and A are as shown in Figure 5-2. Equation 5-5 can be readily shown from simple geometric arguments. Consider a cylinder of length L with its axis in the z-direction. A vertical cut in the x-y plane creates the following projection:

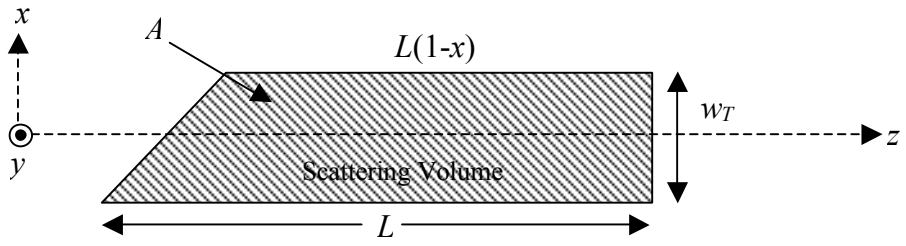

Figure 5-2: Measurements for cut cylindrical volume determination.

It can be easily shown that the volume of the truncated cylinder is identical to ½πr.A, where A is the projected area and r the radius of the cylinder.

The total scattering power can be determined by integrating over ω

$$P_s\left(\vec{k}\right) = \int\left|P'_{FDS}\left(\vec{k},t\right)\right|dt = \frac{\int\left|F(\omega)^{-1}P_s\left(\vec{k},\omega\right)\right|^2 d\omega}{2C} \qquad \textbf{5-6}$$

where $P'_{FDS}(\vec{k},t)$ is the actual signal produced by the diode and C is the Watts/V proportionality factor for the diode from the calibration data. The two integrals in 5-6 are identical through the use of Parseval's theorem [66]:

$$\int|f(t)|^2 dt = \int|g(\omega)|^2 d\omega \qquad \textbf{5-7 (Parseval's Theorem)}$$

Where $f(t)$ and $g(\omega)$ are a Fourier pair and are integrated over all space. Once $S(\vec{k},\omega)$ is determined from 5-2, integration over ω provides $S(\vec{k})$ for multiple values of $\vec{k}$,

integration over $\vec{k}$ allows determination of $\frac{\tilde{n}_e}{n_e}$ which is the density fluctuation level and is expected to be on the order of 0.1 – 1.

5.3 Experimental Operating Regimes

To determine the behavior of any modes detected, the STOR-M parameters were varied to change T_e and B_t in a controlled manner. Different plasma conditions were created by independently varying the plasma current (in order to change T_e) and toroidal magnetic field. The STOR-M has a narrow operating regime, therefore these parameters were varied as much as possible whilst still achieving a clean discharge and also not risking damage to the equipment. Table 5-1 and Table 5-2 below list the plasma parameters for the different regimes. The values quoted are the mean values for all shots at those settings, the values in the brackets are the standard deviation of the parameters.

Parameter	**Low I_p**	**Mid I_p**	**High I_p**
I_p (kA)	17.6(0.3)	22.6(0.4)	29.5(0.4)
T_e (eV)	150(7)	180(10)	210(10)
n_e (10^{18} /m^3)	4.2(0.6)	5(1)	6.5(0.8)
τ (ms)	1.0(0.1)	1.0(0.2)	1.1(0.2)
V_l (V)	2.6(0.2)	2.6(0.2)	2.9(0.2)
B_t (T)	0.518(0.003)	0.571(0.003)	0.612(0.003)

Table 5-1: List of routine parameters during I_p variation.

Parameter	Low B_t	Mid B_t	High B_t
B_t (T)	0.468(0.001)	0.568(0.003)	0.700(0.005)
I_p (kA)	20.1(0.4)	17.6(0.3)	19.5(0.3)
T_e (eV)	150(5)	160(6)	175(10)
n_e (10^{18}/m^3)	3.5(0.4)	4.2(0.6)	4.7(0.4)
τ (ms)	0.70(0.08)	1.0(0.1)	1.4(0.1)
V_l (V)	2.8(0.1)	2.6(0.2)	2.2(0.1)

Table 5-2: List of routine parameters during B_t variation.

Changing only I_p or B_t was not possible, but within each set, I_p or B_t is the largest change. The operating regimes overlap at 'Low I_p' and 'Mid B_t' and these data sets represent the exact same operating regime.

Within each operating regime, $\vec{k}$ was varied using the same equipment settings as determined from the GUI. At each setting the microwave mask was positioned so as to remove any unwanted signal. However at small scattering angles the side lobes from the standard gain horn would collect small signals directly from the GOLA. Similarly, at large scattering angles a signal was detected due to reflections (see Figure 6-3). Whether or not these unwanted signals are a problem depends on the relative magnitude of the scattered signal and will appear as inconsistent results.

5.4 Analysis Pipeline

The data collected daily was stored according to the date on the central data acquisition computer. A separate record was kept correlating the shot numbers recorded with the respective scattering vectors and operating regimes. These records allowed access to all the raw data collectively for data processing:

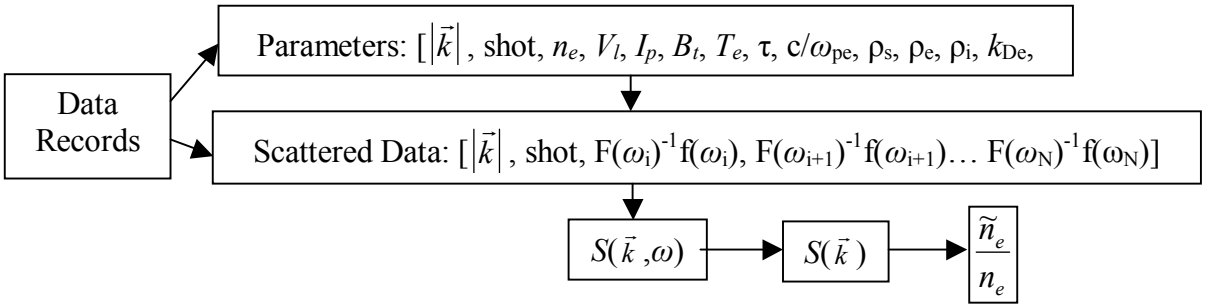

Figure 5-3: Data pipeline flowchart

where 'shot' is the shot number and the parameters are as described in Sections 2 and 3.5. The 'Parameters' and 'Scattered Data' are kept separately according to the operating regimes. $S(\vec{k}, \omega)$ is generated through Equation 5-2 and integrated over ω to determine $S(\vec{k})$, which is integrated over $\vec{k}$ to approximate the density fluctuation percentage.

To calculate the parameters and scattering data requires determining the flat-top regime for each shot and analyzing the data over that segment. The plasma current does not begin at the exact same time from shot to shot, and the data acquisition systems frequently miss-trigger from noise. Therefore the flat-top time in the scattering and housekeeping data is not known a priori and must be determined individually for each shot. Both data sets are then determined from 5ms of data in the flat-top regime, found by scanning the data from each shot.

Chapter 6

Analysis and Results

6.1 Introduction

A typical $S(\vec{k})$ spectrum is presented and discussed, illustrating the problems encountered from multiple reflections during larger scattering angle experiments. The data is then processed to determine a lower level on the density fluctuation level and compared with previous results from other tokamaks. The frequency spectra are then examined and show similar trends to that expected for drift wave type turbulence: similarly $S(\vec{k})$ is analyzed and exhibits drift type scaling. The fluctuation level is shown to be inversely proportional to the confinement time, consistent with the concept of turbulence driving anomalous losses. Finally the turbulence is related to the operating conditions to examine optimum STOR-M operating points.

6.2 Complete $S(\vec{k})$ Spectrum

The data was processed and a typical $S(\vec{k})$ spectrum is presented below:

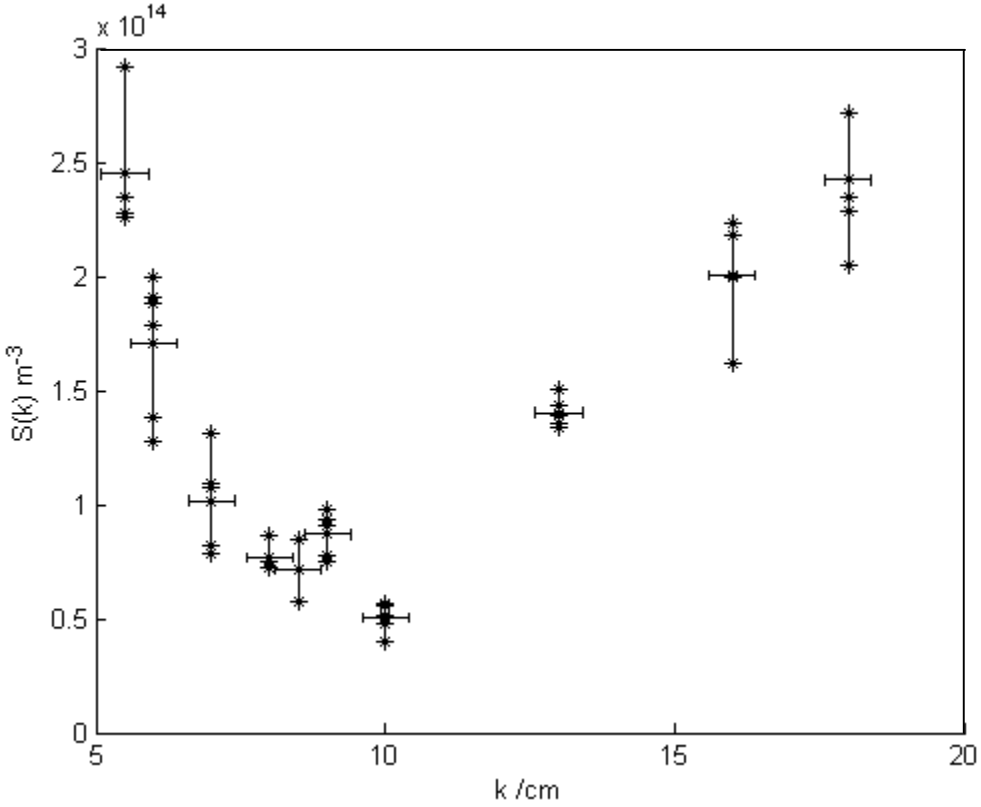

Figure 6-1: Spectral density function during a typical low plasma current discharge. Horizontal error bars are ± 0.4 /cm and vertical bars represent the range of the data.

The data in the low $|\vec{k}|$ range (5 – 10 /cm) shows the expected behavior for drift type modes and correct scaling as will be shown. However, the increase in S($\vec{k}$) at larger $|\vec{k}|$ is not correlated with variations in the plasma parameters and had a chaotic dependence on plasma parameters. At first it was hypothesized that the increase in S($\vec{k}$) could be due to a switch between measuring $\vec{k}_r$ and $\vec{k}_\theta$ at $|\vec{k}| \approx 10$ /cm. This change is due to the physical geometry of the scattering volumes required:

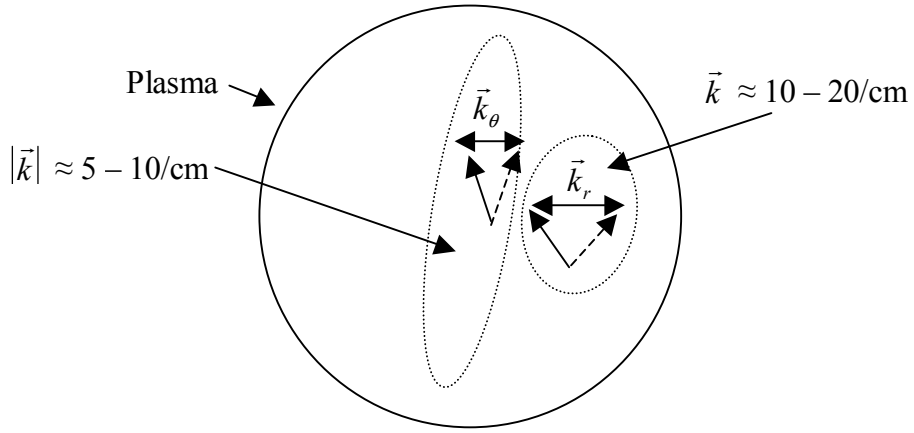

Figure 6-2: Different scattering volumes illustrating a possible shift from measuring $\vec{k}_\theta$ to $\vec{k}_r$ at larger scattering angles

The dotted areas describe the general location of the scattering volume for the respective scattering vectors. However, previous scattering experiments in the ATC Tokamak [67] and more recently on the TORE-SUPRA [68] demonstrated that the density fluctuations are not restricted primarily to the radial nor poloidal directions. In fact the work on the ATC Tokamak demonstrated similar spectra in the radial and poloidal directions, and since it has become common to neglect the $\vec{k}$ direction and instead refer to $\vec{k}_\perp$, which refers to vectors perpendicular to $\vec{B}_t$.

Another more likely explanation for the increase in $S(\vec{k})$ at large $|\vec{k}|$ is due to unwanted reflections leading to multiple scattering volumes, supported by the detection of unwanted scattered power in the absence of a plasma. For smaller scattering angles, the transmitted and received beams passed through the plasma and out of the chamber through the vertical ports (see Figure 4-9). However, at larger scattering angles the microwave beams impinge on the vacuum vessel which acts as a near perfect mirror (96% reflectance). This generates a complicated collection of reflected beams:

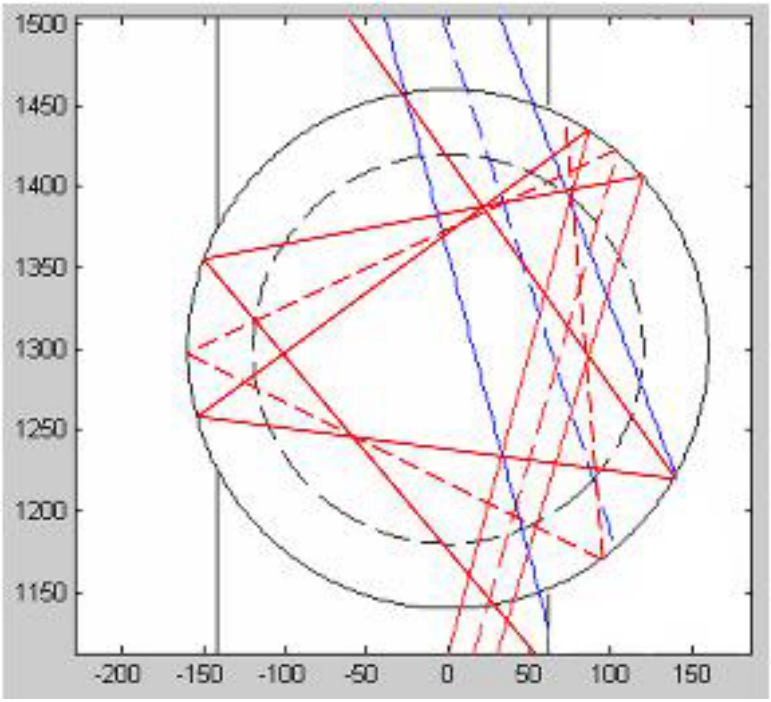

Figure 6-3: Multiple beam reflections caused by the vacuum vessel. Dimensions are in mm

Figure 6-3 uses the backdrop from the GUI interface, 3 reflections of the incident beam (incident from the bottom) are drawn, the reception beam (exiting at the top) also undergoes complicated reflections which are not drawn for clarity. Clearly these reflections result in multiple scattering volumes, with each volume representing a different scattering vector and electron count. Furthermore, in this orientation, low power levels of the transmitted beam could be detected directly by the diode in the absence of a plasma, supporting this scenario; in contrast smaller scattering angles provided no signal in the absence of a plasma. Although this signal was still much smaller than the scattering signal during a discharge, it confirms the possibility of multiple scattering volumes. Possible solutions to this problem require the placement of beam dumps inside the vacuum chamber to limit reflections from the walls. However, as 140 GHz is not a commercially used frequency, vacuum safe high power beam dumps are not readily available. Nevertheless, scattering in the range $\left|\vec{k}\right| \approx 5$ - 10 /cm does not have this problem and therefore this data is analyzed in detail in the following sections.

6.3 Density Fluctuation Level

The relative density fluctuation level $\frac{\tilde{n}_e}{n_e}$ is a common measure of the fluctuation level of the plasma. As discussed earlier, drift wave theories [69] and experimental data [70] suggest the following scaling law:

$$\frac{\tilde{n}_e}{n_e} \sim \frac{1}{\bar{k}_\perp L_n} \sim \frac{\rho_s}{L_n} \qquad \textbf{6-1}$$

$$\bar{k}_\perp \approx \frac{\sum_{k_\perp} k_\perp S(k_\perp)}{\sum_{k_\perp} S(k_\perp)} \qquad \textbf{6-2}$$

where $\bar{k}_\perp$ is the mean fluctuation wavelength and L_n is the density scale length. From the data, $\bar{k}_\perp$ is calculated by applying 6-2 to all the operating regimes and found to be approximately 7 ± 1.5 /cm. The gradient scale length is determined from a parabolic density distribution:

$$L_n \approx \frac{1}{2} \frac{\left(1 - \left(r/a\right)^2\right) a^2}{r} \qquad \textbf{6-3}$$

where a is the minor radius and r the radial position. Notice that this L_n approximation is independent of n_e. For low $\vec{k}$ measurements ($|\vec{k}| \approx$ 5-10 /cm) r covers the plasma column. Therefore the parabolic density and temperature is used to determine a weighted solution for $1/L_n \approx 10$ /m and $\rho_s \approx 0.0015$ m, giving an expected fluctuation level of the order $\sim 0.015 \pm 0.003$ for both definitions of the fluctuation level (Equation 6-1).

The above calculation only used the data for determining the mean wavelength and as such was independent of the scaling factors used to determine absolute values for the spectral density. Once the data was scaled correctly according to 5-2, integration across k-ω space revealed a minimum fluctuation level of $\tilde{n} / n \sim 0.07 - 0.1$. This is the first reported measurement of the density fluctuation level in the STOR-M and can be added to existing data:

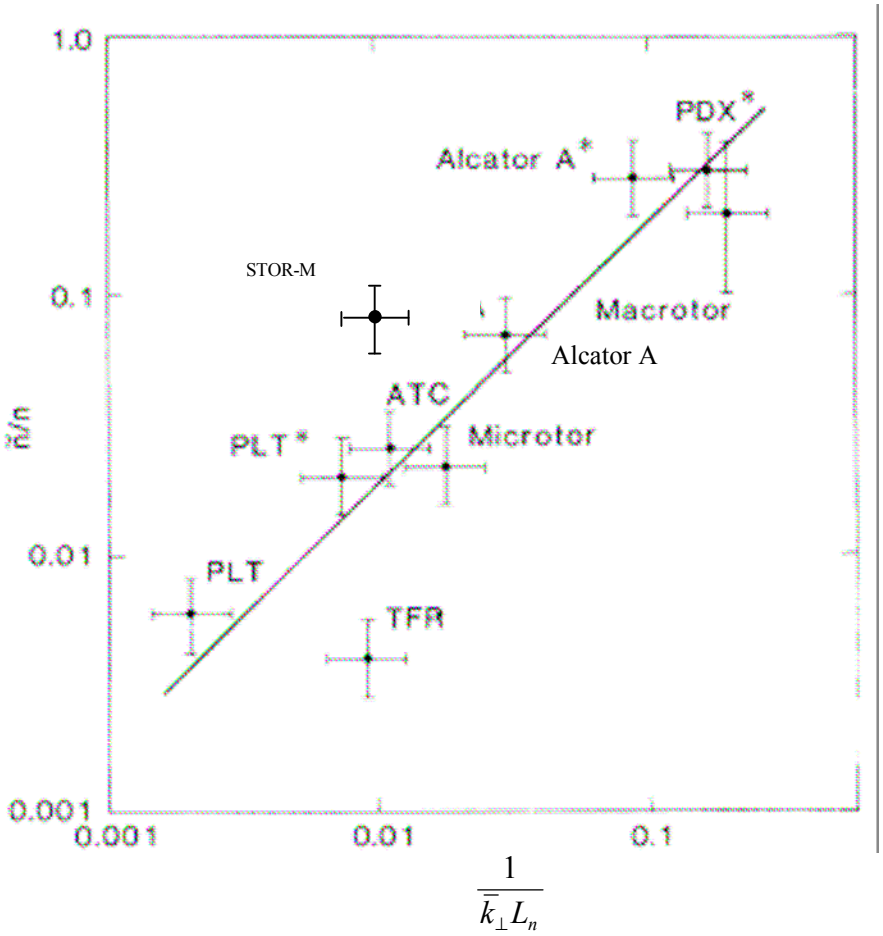

Figure 6-4: Density fluctuation levels for several tokamaks from scattering data. The asterisks indicate data from nearer the plasma edge. (adapted from Surko [70])

From Figure 6-4 one can see agreement between the value measured for the STOR-M and the measured values from numerous other experiments (the other data is also from scattering experiments). The solid line in the figure depicts $\frac{\tilde{n}}{n} = \frac{2}{L_n \bar{k}_\perp}$.

6.4 Frequency Spectra

Figure 6-5 the typical frequency spectra:

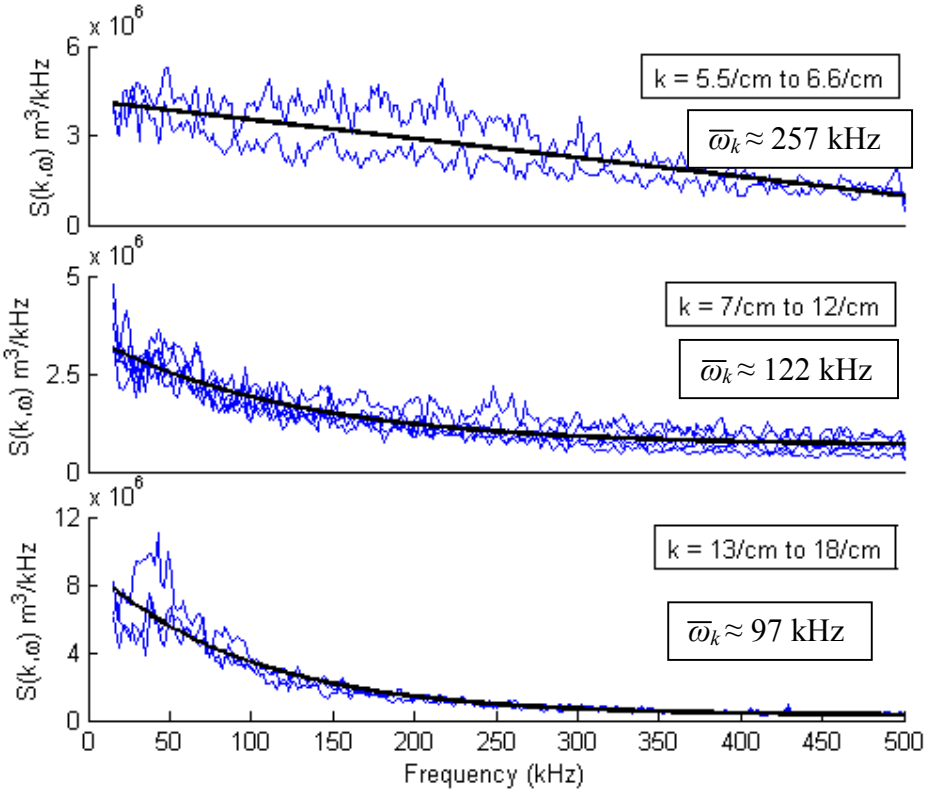

Figure 6-5: Typical frequency spectra. Multiple lines on each graph represent spectra for different scattering vectors within the range specified. $\bar{\omega}_k$ is the fit parameter to $S(\vec{k},\omega) = A(\vec{k})e^{-\frac{\omega}{\bar{\omega}_k}}$

The frequency spectra for different $|\vec{k}|$ ranges shown in Figure 6-5 depict the variation of the spectra with scattering angle. The solid lines are fits to $S(\vec{k},\omega) = A(\vec{k})e^{-\frac{\omega}{\bar{\omega}_k}}$ as described by Watterson *et al.* [71] where $\bar{\omega}_k$ is a fitting parameter. However, at low and high $|\vec{k}|$ one can clearly see the presence of strong low frequency signals that cause the spectra to deviate from a first order exponential decay. At high $|\vec{k}|$ this is a result of the multiple scattering volumes and perhaps some large volumes that cause a stronger influence of the macroscopic MHD turbulence.

The low $\left|\vec{k}\right|$ results also show strong low frequency signals and a much flatter frequency spectrum that does not fit an exponential decay. In this orientation it is feasible that the stray signals detected may have passed directly through the plasma, and therefore would have been phase shifted by the plasma creating the usual fringe signal as per density measurements.

The absence of specific coherent peaks does not preclude the possibility of a non-linear mix of multiple modes. One must also remember that the data is measured from a scattering volume that is relatively large and covers almost the entire radial locations. As the drift-waves and other instabilities tend to have frequencies dependent on spatial location, it is reasonable to assume that averaging over the volume would produce a broad spectrum. This hypothesis was specifically tested by Surko [67] by examining the frequency spread dependence on spatial location in the ATC tokamak using CO_2 scattering. It was discovered that the frequency spread was independent of location and vector direction (isotropic in $\vec{k}_r$ and $\vec{k}_\theta$ in the B_t plane). Therefore it is most likely that the spread is from saturation of several coupled non-linear modes.

As there is no specific coherent mode, various techniques have been developed to determine an approximate dispersion relation from the data. This means that a specific frequency must be extracted to represent the entire frequency spectrum. The first technique fits exponential decay functions to the data (Figure 6-5) and plots $\overline{\omega}_k$ vs $\vec{k}$ where $\overline{\omega}_k$ is the decay constant. Another commonly used technique for broadband spectra is to use

$$\overline{\omega}_k \approx \frac{\int S\left(\vec{k},\omega\right)\omega d\omega}{\int S\left(\vec{k},\omega\right)d\omega} \qquad \textbf{6-4}$$

which can generate $\overline{\omega}_k$ *vs* $\vec{k}$ in what is denoted as the 'statistical dispersion' [72]. There are other methods involving Gaussian fits to heterodyne data or simply using the 1/e or half-maximum value of the data. Using the first two techniques discussed, two dispersion relations were measured.

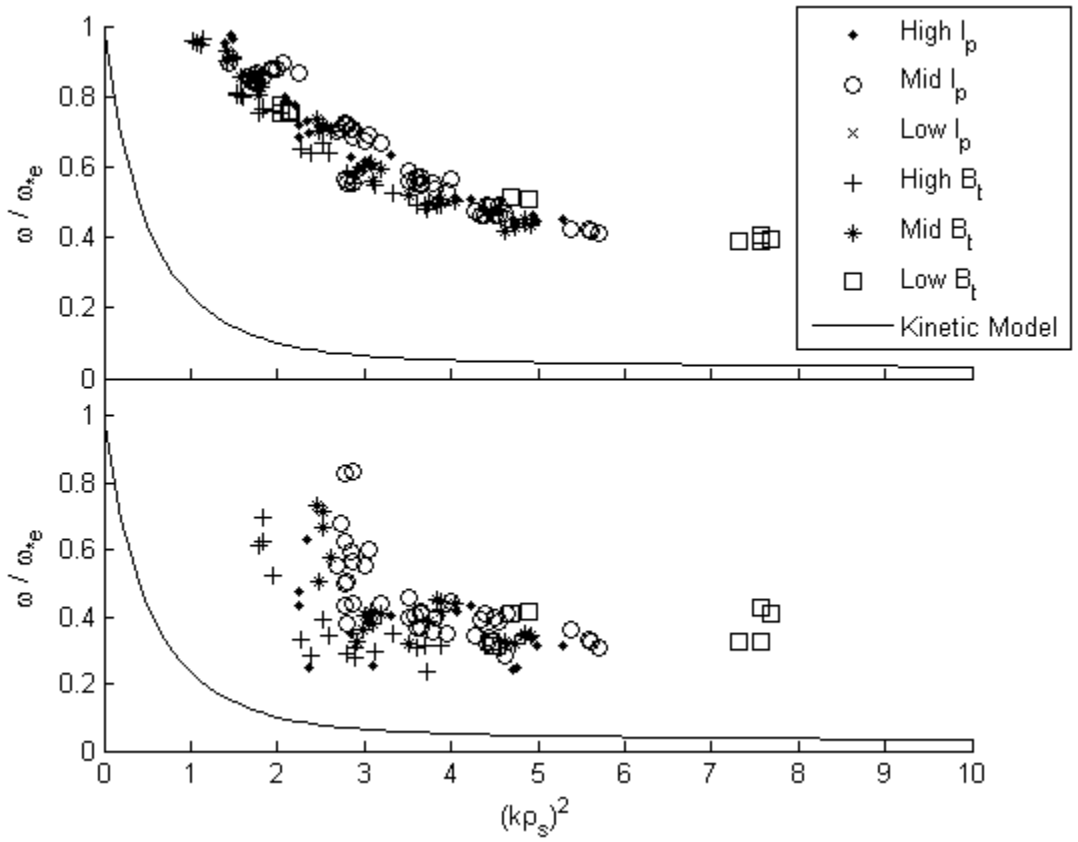

Figure 6-6: Dispersion relations; top graph is from the 'Statistical' method of Eq 6-4 and the bottom graph is using an 'Exponential' fit approach. The kinetic model of section 3.6 is also drawn.

The kinetic model drawn is described by Equation 3-39. Both the model and the data are normalized using the electron diamagnetic frequency (ω_{*e}) and plotted against $\left(k_\perp \rho_s\right)^2$. From Figure 6-6 one can see that the statistical dispersion relation generates a more precise curve than the exponential decay method. The exponential decay technique fails at low $\vec{k}$ values as the frequency spectra deviates from a simple decay in this regime. As the model and data both contain numerous approximations an exact comparison between the two is not possible. Nevertheless, Figure 6-6 does demonstrate that the density fluctuations measured do fall within the frequency regime expected for drift waves from the theoretical model, and also follow similar trends. It can also be seen that the varying plasma conditions seem to have no effect on the frequency spectra. This is confirmed by the model which is independent of B_t and only depends on the ratio T_e/T_i which remains relatively constant in all the discharges.

6.5 Spectral Density Function

The spectral density for the B_t and I_p variations are shown below:

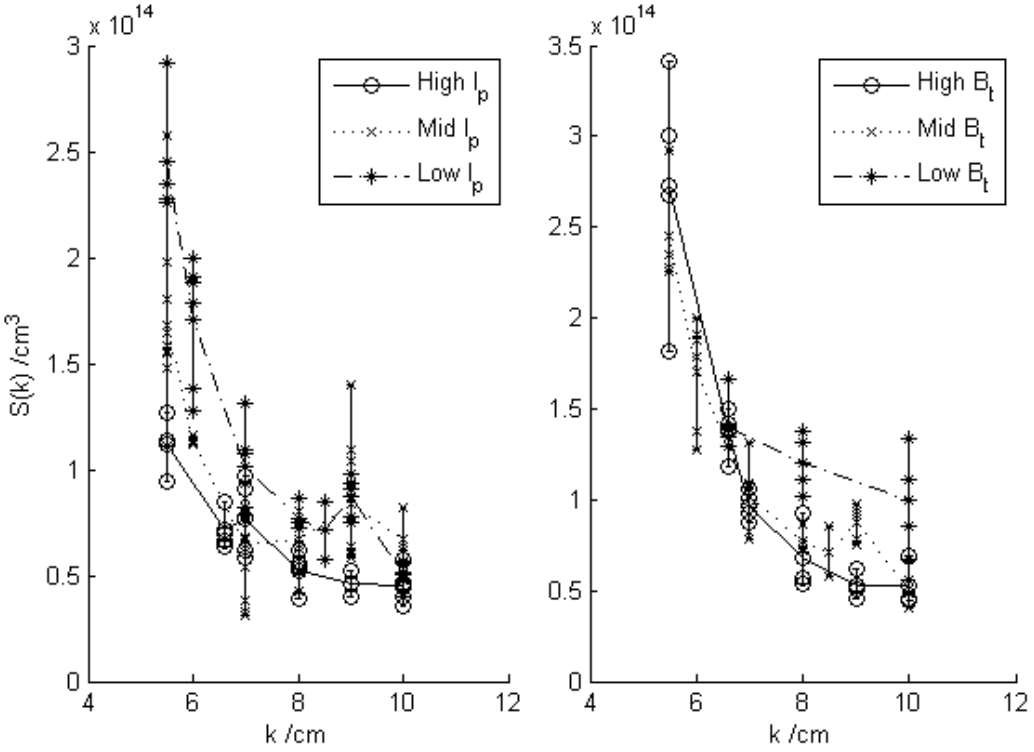

Figure 6-7: Spectral density functions for I_p and B_t variations respectively.

The graph on the left is from I_p variation and the one on the right from B_t variation (in each plot, the invariant variable is only loosely fixed). Work by Crowley *et al.* [73] showed that plots of $S(\vec{k})$ versus $\vec{k}_* = \vec{k} \cdot B_0 / B_t$ (B_0 represents the mean field) accurately scaled the data, indicating that $k_\perp \rho_s$ is the relevant parameter. Here that work is extended to include the temperature dependence of the data. To achieve this, $S(\vec{k})$ is plotted against the following normalization parameter:

$$\vec{k}_* = \vec{k}_0 \cdot \left(\frac{T_e}{T_0} \right)^{\alpha} \cdot \left(\frac{B_t}{B_0} \right)^{\beta} \qquad \textbf{6-5}$$

where B_0 and T_0 are the mean levels, and α and β are the two fitting parameters. The fitting of two fit parameters simultaneously is required as it was not possible to maintain

B_t whilst varying T_e nor vice versa within the STOR-M (see Table 5-1 and Table 5-2). The spectral density is modeled as a first order exponential decay and a second order polynomial. The values of α and β are then varied in α-β space and the resultant goodness of fit is recorded. The goodness of fit is determined using the standard multiple-correlation coefficient R^2 [74]. Two different models were chosen to determine the better fit to the data. Figure 6-8 below shows two contour plots of $R^2(\alpha,\beta)$:

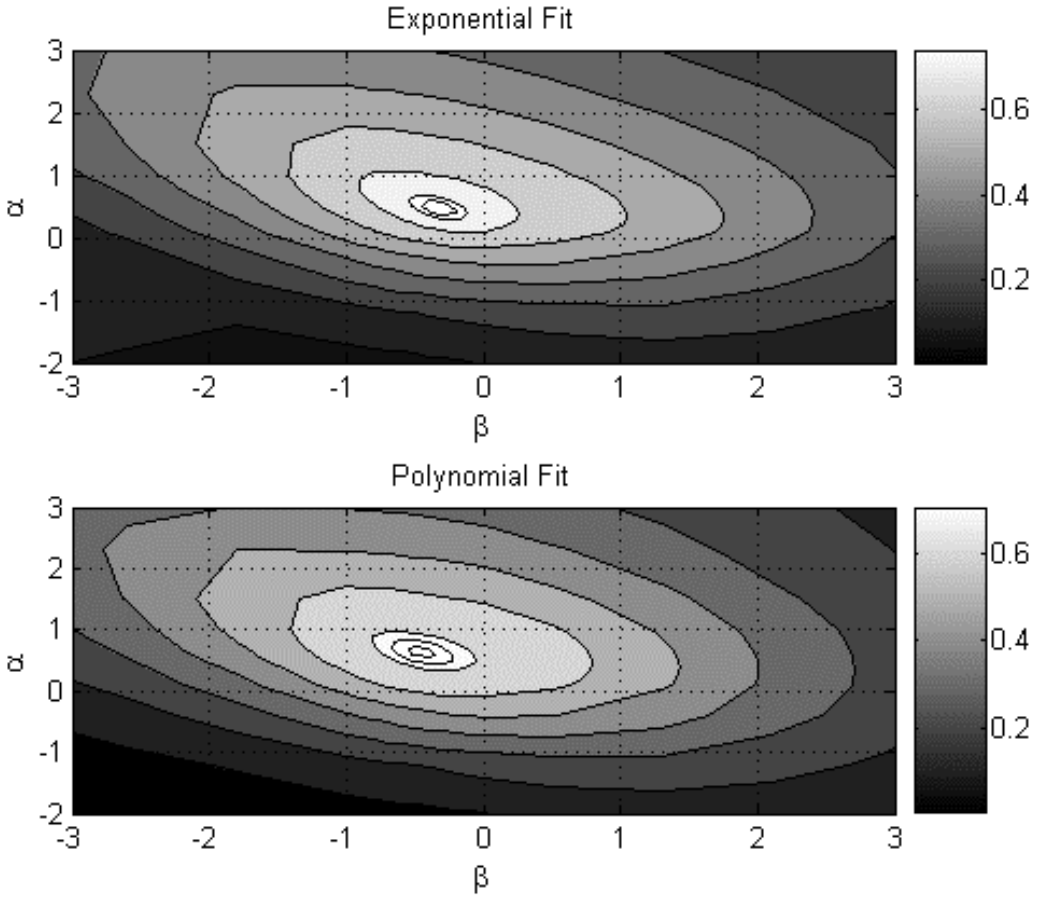

Figure 6-8: Contour plots of $R^2(\alpha,\beta)$ for the two separate fitting functions.

From Figure 6-8, R^2 maximizes at 0.74 and 0.71 for the exponential and polynomial fit respectively, this occurs at $\alpha = 0.4 \pm 0.3$ and 0.6 ± 0.4, and $\beta = -0.4 \pm 0.5$ and -0.4 ± 0.6 for both sets respectively. The error in these parameters was found by fitting Gaussian curves to lines of constant α and β passing through the maximum R^2 point in each graph, where the value at the FWHM was used to define the error margin. Combining these results gives $\alpha = 0.5 \pm 0.5$ and $\beta = -0.4 \pm 0.6$. If ρ_s was the correct scaling parameter then one expects $\alpha = 0.5$ ($\sqrt{T_e}$) and $\beta = -1$ (B^{-1}) which is within experimental error. For ETG type

fluctuations one expects scaling with the skin depth (c/ω_{pe}) or inverse Debye length ($1/k_{De}$) which indicate $(n/n_0)^{\gamma}$ scaling with γ = -0.5 for both cases. The raw data is scaled with $k_* = k_0 \cdot \left(\frac{T_e}{T_0}\right)^{0.5} \cdot \left(\frac{B_t}{B_0}\right)^{-0.4}$ and then scaled again with $k_{*2} = k_0 \left(\frac{n}{n_0}\right)^{\gamma}$, and γ is scanned to maximize R^2. Figure 6-9 below shows that the data appears to be independent of density as the best fit occurs for γ ≈ 0

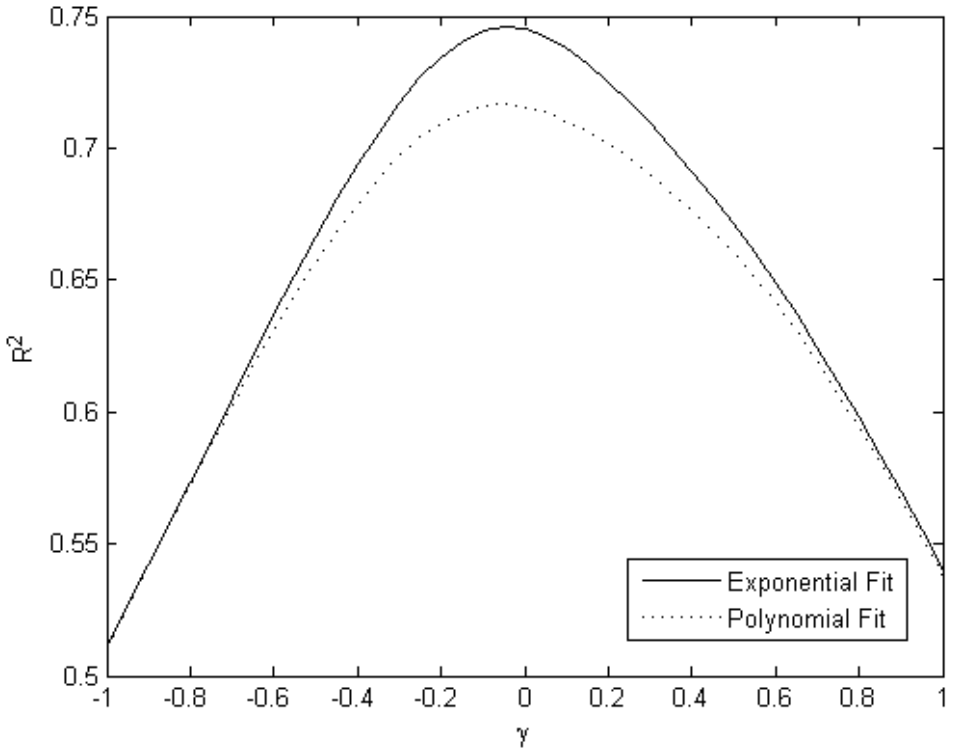

Figure 6-9: Density scaling of the spectral density function, which peaks near γ ≈ 0

Therefore scaling as $T_e^{0.5\pm0.5} B_t^{-0.4\pm0.6}$ seems most appropriate and agrees within error to the work by Brower *et al.* [72] who showed scaling as $T_e^{0.3} B_t^{-0.6}$ on the TEXT Tokamak. Furthermore this supports ρ_s scaling within error ($T_e^{0.5} B_t^{-1}$) as expected for drift-type fluctuations, and shows no signatures of ETG type modes. Figure 6-10 shows the data with and without normalization. $\vec{k}_*$ clearly represents a correct scaling factor as it removes trends in the data from T_e and B_t variations.

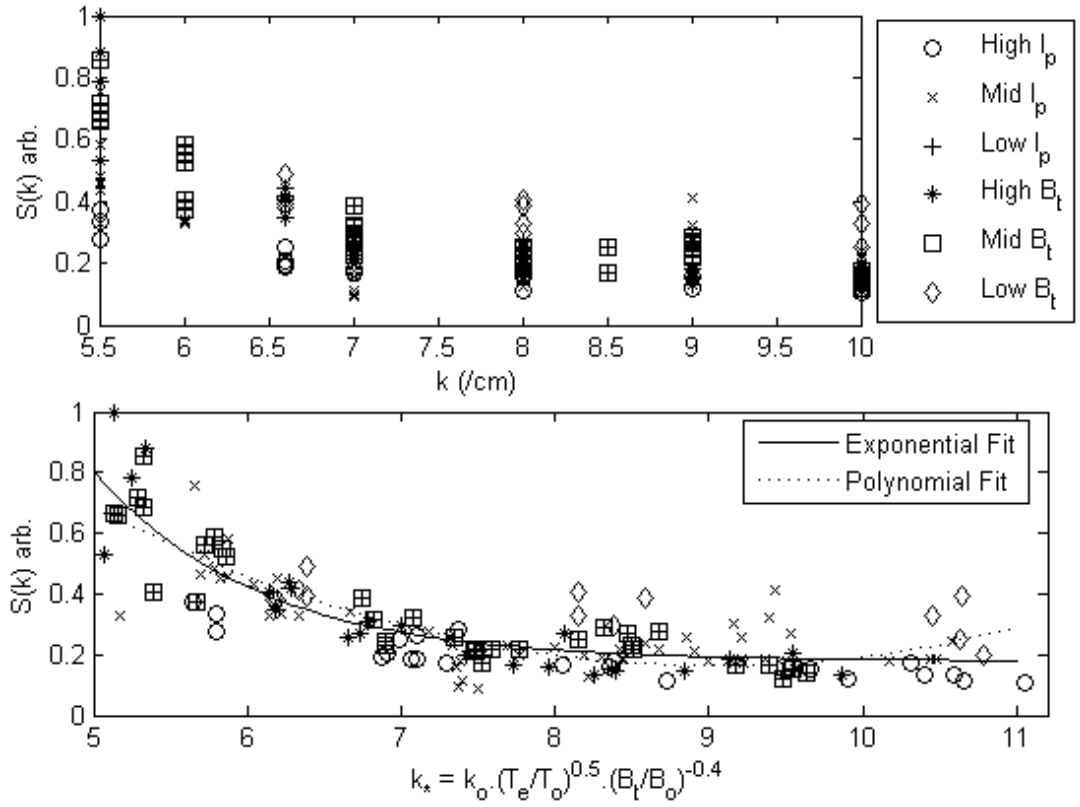

Figure 6-10: Raw spectral density function and normalized spectral density function indicating the application of the correct normalization parameters.

Correct scaling with $k_\perp \rho_s$ indicates that ion drift waves are dominating the density fluctuations as observed by this experiment. These results do not dismiss the existence of the ETG mode but suggest that during a normal ohmic discharge the ion drift waves are dominant in the STOR-M. Detection of ETG mode fluctuations may require suppression of ion drift wave turbulence through H-mode discharges. H-mode discharges are difficult to achieve on the STOR-M and were not used during this experiment, but may be essential for future scattering experiments. This hypothesis is supported by work on the NSTX [48] and DIII-D [75] tokamaks where scattering experiments similar to this work are being performed during advanced discharges with maximum fluctuation suppression to search for the ETG mode.

6.6 Fluctuation Level and Confinement Time

The measurement of anomalous losses is generally made by comparison between the measured confinement time (τ_m) and the calculated confinement time (τ_c). The calculated confinement time is a theoretically calculated value based on the machine parameters assuming neo-classical losses [69]. A substantially smaller τ_m then τ_c indicates the presence of unexplained losses from the system, which is the case in all tokamaks. The STOR-M does not have the capability to accurately determine τ_m (only a crude approximation can be measured as shown in section 2.2.4) nor has τ_c been completed calculated. However, from this experiment a weak correlation between $\tilde{n}_e / n_e$ and the approximate τ_m is observed.

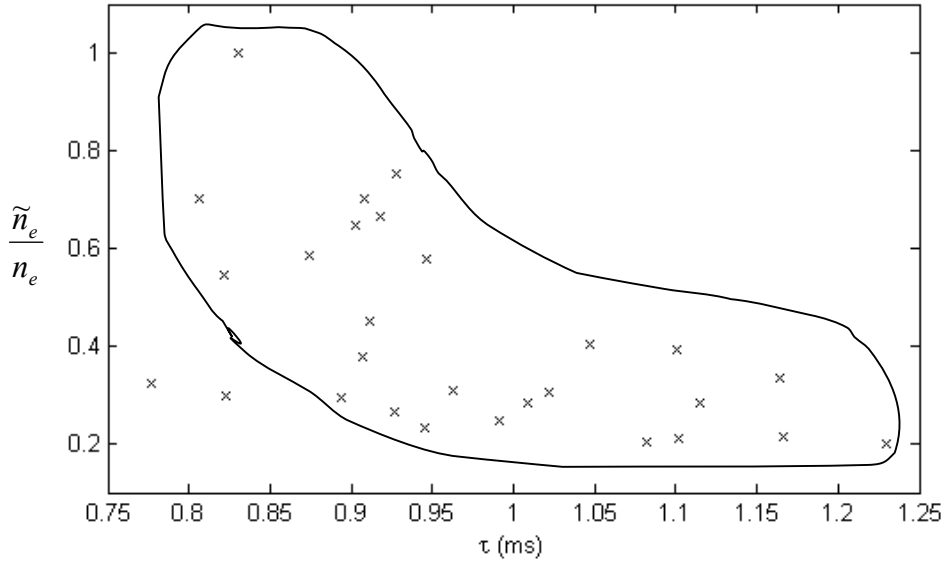

Figure 6-11: Inverse relationship between confinement time and $S(\vec{k})$ from the mid range I_p data.

In Figure 6-11, $S(\vec{k})$ is the values measured from the 'Mid I_p' regime and is from all $\vec{k}$ vectors. Figure 6-11 shows the first reported evidence of increased density fluctuations in the STOR-M plasma core causing a decrease in the global approximate confinement time. This supports the accepted theory that density fluctuations in a plasma drive anomalous losses out of the system.

6.7 STOR-M Operating Regimes

The different fluctuation levels measured in various operating regimes can be used to attempt to define an optimum operating condition for the STOR-M Tokamak. Specifically, five different settings were used to produce varying plasmas: High I_p, Mid I_p, Low I_p = Mid B_t, High B_t and Low B_t. The same method is used as per Figure 6-11, but now S($|\vec{k}|$ = 6 /cm to 7 /cm) is a function of both I_p and B_t and therefore a 3-dimensional plot is required.

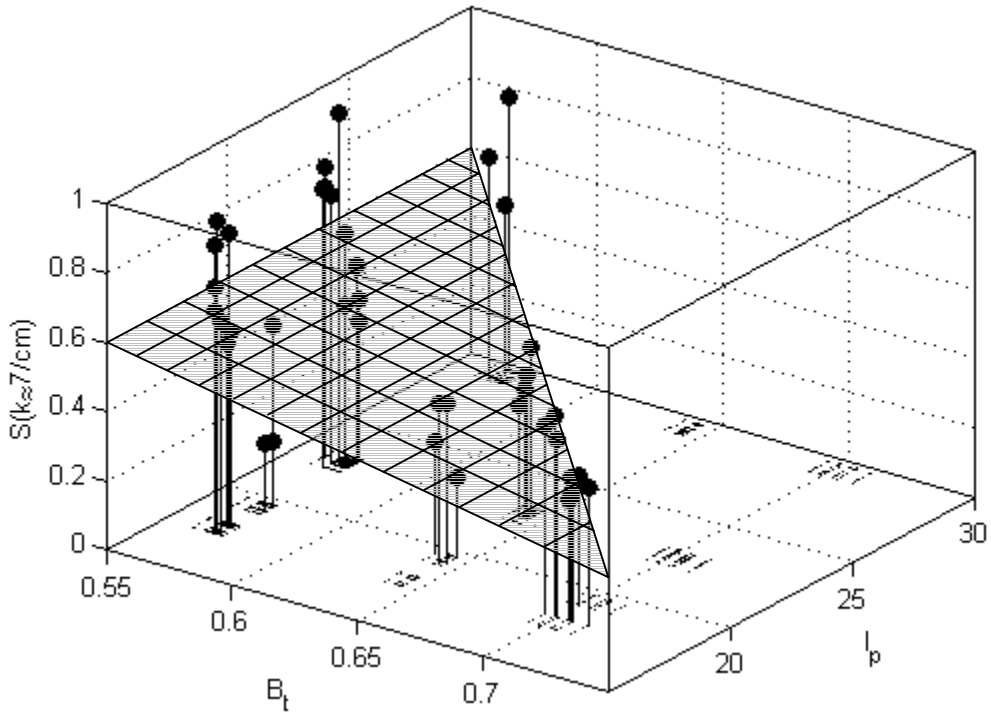

Figure 6-12: STOR-M fluctuation levels for various operating regimes. The surface is added to amplify the trends in the data.

From Figure 6-12 one can see a correlation between increasing magnetic field and decreased fluctuation levels, and an increased current seems to have little effect on the fluctuation level. This points to an optimum regime with high B_t and variable I_p. The normal operating condition of the STOR-M is at $B_t \approx 0.6$ T and $I_p \approx 22$ kA. This data shows that a more stable plasma is produced if B_t is increased substantially without necessarily varying I_p. High B_t and high I_p might produce the most stable plasma,

however it also places the most mechanical stress on the system and therefore such a regime is not possible without risk to the equipment. Therefore in future experiments it is recommended that I_p remain at approximately 22 kA but B_t be increased to 0.7 T (500 kV on the B_t capacitor banks)

Chapter 7

Summary and Conclusions

7.1 Summary of the Present Work

The elusive goal of research into thermonuclear fusion is to produce commercially viable sustainable energy. One of the central challenges preventing the construction of commercial fusion power plants today is the inability to successfully confine a plasma that is capable of sustaining fusion reactions in a steady state equilibrium. A major reason for this problem occurs through anomalous losses; which are energy and particle losses from the plasma that greatly exceed those predicted by theoretical calculations.

It is generally conjectured that these losses are driven by turbulence and micro-instabilities within the plasma [12]. Although modern advanced tokamaks can reduce ion losses to neo-classical levels [13], electron losses remain anomalously large. One possible candidate for these electron losses is the electron temperature gradient (ETG) mode. This project attempted to study these density fluctuations using a microwave scattering experiment. The scattering system was capable of measuring fluctuations in the range $\left|\vec{k}\right|$ = 5 – 10 /cm. This range of density fluctuations covers both ion drift waves and electron temperature gradient (ETG) modes, which are both expected to maximize on the order of $\left|\vec{k}\right|$ = 5 /cm in the STOR-M.

A kinetic model was derived for ion drift waves in a plasma slab geometry. The model suggested frequencies on the order of the electron diamagnetic frequency (ω_{*e}) with a scaling with $k\rho_s$, where ρ_s is the ion Larmor frequency with electron temperature. This

kinetic fluid model is consistent with other experimental data [67] and more involved theoretical works [43], which additionally indicate a maximum growth rate at $k\rho_s \sim 1$ (corresponding to $\left|\vec{k}\right| \sim 5$ /cm in the STOR-M).

The ETG mode is a much shorter wavelength, higher frequency mode and therefore also required a full kinetic approach. The perturbed density distribution function was substituted into Poisson's equation and the parallel Ampere's law to enable the derivation of a dispersion relation for this mode. The results of this calculation from Hirose [15] were presented indicating a scaling with $(k/k_{De})^2$ and a maximum transport occurring on the order of the skin depth $c/\omega_{pe} \sim 1/5$ cm. No experimental evidence of the behavior of this mode is available as it is yet to be detected directly.

The density fluctuations were measured using a 140 GHz microwave scattering system powered by a 13 W EIO Klystron (Extended Interaction Oscillator). The scattering theory behind this homodyne system is derived in full from first principles in this work. The system was originally built by Dr. Conway in 1993 as a prototype system but was never operated. All the components were rigorously tested and numerous modifications were made to the design before the system was operational.

The mechanical design was altered to allow modifications to the waveguide circuits as required. This was necessary as the waveguide circuit had to be reconstructed to remove malfunctioning components as well as for testing of new and existing equipment. Initial scattering results showed a strong correlation between magnetohydrodynamic (MHD) activity and the scattering signal due to the relatively large scattering volume. A new electronic amplifier and filter was designed and constructed to successfully limit the influence of MHD activity on the scattering data.

Scattering vectors from $\left|\vec{k}\right| = 5 - 18$ /cm were measured in discrete steps for 5 different plasma conditions. The STOR-M was operated in these various plasma conditions to alter the temperature and toroidal field such that the dependence of the density fluctuations on

these parameters could be studied. It was also found that a high launch power (~ 8 W) was creating several reflections and multiple scattering volumes at larger scattering angles due to geometrical constraints. Therefore the useful scattering data was restricted to $\left|\vec{k}\right|$ = 5 – 10 /cm.

From the data it was possible to extract the density fluctuation level of the plasma, which was $\tilde{n} / n \approx 0.1$ at an average wave number of $\bar{k} \approx 7$ /cm and is reported for the first time for the STOR-M. This is consistent with the approximation from mixing length theory and experiment [70] that points towards $\tilde{n} / n \sim 1/\bar{k} L_n \sim \rho_s/L_n \approx 0.015$. The density fluctuation level was also comparable with similar independent measurements on different tokamaks of varying sizes and configurations.

The density fluctuations were found to scale with $T_e^{0.5\pm0.5} B_t^{-0.4\pm0.6}$ consistent with ion drift-wave theory [44] and experiment [72] that suggests $T_e^{0.5}.B_t^{-1}$ and $T_e^{0.3}.B_t^{-0.6}$ respectively. Signatures of the elusive electron temperature (ETG) mode were not detected and have yet to be detected directly by any experiment. The ETG mode appeared to be hidden from the equipment by the dominant ion drift-waves. Furthermore, the spectral density function was shown to maximize for $(k_\perp \rho_s)^2 < 5$ consistent with the expected value for ion drift-wave turbulence which generally maximizes at $(k_\perp \rho_s)^2 \sim 1$.

The data also showed a weak inverse relationship between density fluctuations and the energy confinement time (τ_e). This provides evidence that within the STOR-M density fluctuations are causing losses from the plasma and reducing the plasma confinement.

7.2 Recommendations for Future Work

The scattering system is now fully operational for drift wave analysis in the $\left|\vec{k}\right|$ = 5 /cm to 10 /cm regime. The system can be used in its current configuration in conjunction with ongoing experiments on the STOR-M with Compact Torus (CT) injection [23]. The analysis of core plasma oscillations during CT injection has never been measured and

would be a novel set of results. Similarly, density fluctuation suppression during H-mode events (periods of induced improved plasma confinement) in the STOR-M have never been measured and this system could act as an independent assessment of the effectiveness of the H-mode trigger technique (electrode biasing [21], turbulent heating [19] and horizontal or vertical CT injection).

The range of scattering vectors could be improved by the placement of microwave absorbers inside the vacuum vessel to prevent unwanted reflections of the transmitted and received signals. Furthermore, replacement of the standard gain horn with a more effective Gaussian Optic Lens Antenna would refine the scattering volume. This coupled with improved gas puffing and H-mode triggered discharges would enable the system to move closer to measuring the ETG signatures. This method of drift wave suppression to measure ETG fluctuations is currently being employed on the NSTX [46] and DIII-D [75] tokamaks where microwave scattering experiments are being performed during advanced discharges. Both teams suggest that the suppression of ion turbulence during the discharge should allow for the detection of the persistent ETG mode that appears to drive anomalous electron losses. Direct measurement of this mode has yet to be achieved.

Appendix A – Scattering Formulae Derivation

This derivation is guided by the works of Sheffield [37], Jackson [34] and Surko and Slusher [71].

$$P_s(\vec{R},t)=R^2\Omega c\varepsilon_o\frac{1}{T}\int_{\frac{-T}{2}}^{\frac{T}{2}}dt\left|\vec{E}_s^{\,T}(t')\right|^2$$

As long as T is much greater then the coherence time of the fluctuations, the limit $T \rightarrow \infty$ can be taken. We now Fourier transform $\vec{E}_s^{\,T}(t)\rightarrow\vec{E}_s^{\,T}(\omega_s)$ to determine the variation of scattered power as a function of frequency. We then use Pareseval's theorem to convert back to $\vec{E}_s^{\,T}(t)$.

$$P_s\left(\vec{R},\omega_s\right)=R^2\Omega c\varepsilon_o\lim_{T\to\infty}\frac{1}{2\pi T}\int_{-\infty}^{\infty}d\omega_s\left|E_s^T(\omega_s)\right|^2$$

$$P_s\left(\vec{R},\omega_s\right)=R^2\Omega c\varepsilon_o\lim_{T\to\infty}\frac{1}{2\pi T}\int_{\omega_s-d\omega_s/2}^{\omega_s+d\omega_s/2}d\omega_s\left|\int_{-\infty}^{\infty}dtE_s^T(t')e^{-i\omega_s t'}\right|^2$$

The integration over ω_s is limited as the system can only detect signals near 140GHz. We take $\vec{E}_s$ from:

$$\vec{E}_{sj}\left(\vec{R},t\right)=\frac{q}{4\pi R}\eta\left[\hat{s}\times\left(\hat{s}\times\dot{\vec{\beta}}\right)\right]_{ret}$$

$$\dot{\vec{\beta}}=-\frac{e}{m}\cdot\vec{E}_i(t')=-\frac{e}{m}\cdot\vec{E}_{io}\cos\left(\vec{k}_i\cdot\vec{r}-w_i t'\right)$$

And insert it into our equation for P_s remembering that:

$$\vec{E}_s^{\,T}(\vec{R},t)=\int d\vec{r}\int d\vec{v}F_e(\vec{r},\vec{v},t')\vec{E}_{sj}(\vec{R},t')$$
$$=\int d\vec{r}\,n_e(\vec{r},t')\vec{E}_{sj}(\vec{R},t')$$

$$P_s(\vec{R},\omega_s)=R^2\Omega c\varepsilon_o\lim_{T\to\infty}\frac{1}{2\pi T}\int_{\omega_s-d\omega_s/2}^{\omega_s+d\omega_s/2}d\omega_s\left|\int d\vec{r}n_e(\vec{r},t')\int_{-\infty}^{\infty}dt\,\frac{\gamma_e}{R}\left[\hat{s}\times\left(\hat{s}\times\vec{E}_{io}\right)\right]e^{-i\omega_s t}\cos\left(\vec{k}_i\cdot\vec{r}-w_i t'\right)\right|^2$$

$$=\gamma_e^2\Omega c\varepsilon_o E_{io}^2\left[\hat{s}\times\left(\hat{s}\times\hat{E}_{io}\right)\right]\lim_{T\to\infty}\frac{1}{2\pi T}\left|\int d\vec{r}n_e(\vec{r},t')\int_{-\infty}^{\infty}dt\;e^{-i\omega_s\left(t'-\frac{\hat{s}\cdot\vec{r}}{c}+\frac{R}{c}\right)}\cos\left(\vec{k}_i\cdot\vec{r}-w_i t'\right)\right|^2$$

Remembering that $t'\cong t-\left(\frac{|R-\hat{s}\cdot\vec{r}|}{c}\right)\approx t-\frac{R}{c}+\frac{\hat{s}\cdot\vec{r}}{c}$. We now take the Fourier time and space transform of $n_e(\vec{r},t)$

$$n_e(\vec{r},t')=\int\frac{d\vec{k}}{(2\pi)^3}\int\frac{d\omega}{2\pi}n_e\left(\vec{k},\omega\right)e^{-i\left(\vec{k}\cdot\vec{r}-\omega t'\right)}$$

We also decompose the cosine term into ½($e^{-ia}+e^{ia}$):

$$P_s(\vec{k},\omega)=\gamma_e^2\Omega c\varepsilon_o E_{io}^2\left[\hat{s}\times\left(\hat{s}\times\hat{E}_{io}\right)\right]\lim_{T\to\infty}\frac{1}{2\pi T}\cdots$$

$$\left|\int d\vec{r}\int\frac{d\vec{k}}{(2\pi)^3}\int\frac{d\omega}{2\pi}n_e\left(\vec{k},\omega\right)e^{-i\left(\vec{k}\cdot\vec{r}-\omega t'\right)}\int_{-\infty}^{\infty}dt'\,e^{-i\omega_s\left(t'-\frac{\hat{s}\cdot\vec{r}}{c}+\frac{R}{c}\right)}\frac{1}{2}\left(e^{-i\left(\vec{k}_i\cdot\vec{r}-w_i t'\right)}+e^{i\left(\vec{k}_i\cdot\vec{r}-w_i t'\right)}\right)\right|^2$$

We can now split the integral into two components, below are written the two exponential terms

1) $$-i\left(\vec{k}_i\cdot\vec{r}-\omega_i t+\omega_s t'-\frac{\omega_s}{c}\hat{s}\cdot\vec{r}+\frac{\omega_s}{c}R+\vec{k}\cdot\vec{r}-\omega t'\right)$$
$$=i\left(\left(\omega-(\omega_s-\omega_i)\right)t-\left(\vec{k}-\left(\frac{\omega_s}{c}\hat{s}-\vec{k}_i\right)\right)\cdot\vec{r}-\frac{\omega_s}{c}R\right)$$

2) $$-i\left(-\vec{k}_i\cdot\vec{r}+\omega_i t+\omega_s t'-\frac{\omega_s}{c}\hat{s}\cdot\vec{r}+\frac{\omega_s}{c}R+\vec{k}\cdot\vec{r}-\omega t'\right)$$
$$=i\left(\left(\omega-(\omega_s+\omega_i)\right)t-\left(\vec{k}-\left(\frac{\omega_s}{c}\hat{s}+\vec{k}_i\right)\right)\cdot\vec{r}-\frac{\omega_s}{c}R\right)$$

Now using the following identity: $\delta(x-a)=\frac{1}{2\pi}\int_{-\infty}^{\infty}e^{-ik(x-a)}dk$ we can see various delta functions created through the exponential terms.

Term 1) integration over *t* produces $2\pi\delta(\omega-(\omega_s-\omega_i))$, over r gives $(2\pi)^3\delta(\vec{k}-(\vec{k}_s-\vec{k}_i))$.

Term 2) integration over *t* produces $2\pi\delta(\omega-(\omega_s+\omega_i))$, over r gives $(2\pi)^3\delta(\vec{k}-(\vec{k}_s-\vec{k}_i))$.

Therefore integration over ω and $\vec{k}$ becomes greatly simplified:

$$P_s(\vec{k},\omega)=\gamma_e^2\Omega c\varepsilon_o E_{io}^2\left[\hat{s}\times\left(\hat{s}\times\hat{E}_{io}\right)\right]^2\lim_{T\to\infty}\frac{1}{2\pi T}\ldots$$
$$\left|n_e\left(\vec{k}_s-\vec{k}_i,\omega_s-\omega_i\right)+n_e\left(\vec{k}_s+\vec{k}_i,\omega_s+\omega_i\right)\right|^2$$

Then using the identity: $|n_e(\vec{k},\omega)|^2=|n_e(-\vec{k},-\omega)|^2$ we combine the last two terms (now allowing ω_s to take on negative values) and finally we assume a stationary system and equate the time-average as the ensemble:

$$P_s(\vec{k},\omega)=\gamma_e^2\Omega c\varepsilon_o E_{io}^2\left[\hat{s}\times\left(\hat{s}\times\hat{E}_{io}\right)\right]^2\lim_{T\to\infty}\frac{1}{2\pi TV}\left|n_e(\vec{k},\omega)\right|^2$$
$$=\frac{\gamma_e^2E_{io}^2\Omega c\varepsilon_o}{2\pi}\left[\hat{s}\times\left(\hat{s}\times\hat{E}_{io}\right)\right]^2 n_{eo}\lim_{T\to\infty}\frac{1}{TV}\left\langle\frac{\left|n_e(\vec{k},\omega)\right|^2}{n_{eo}}\right\rangle$$

Then this can be simplified using the following identities:

$P_i=\frac{1}{2}c\varepsilon_o E_{io}^2A$ — A = Cross-sectional area of incident beam

L = Scattering length

$N=ALn_{eo}$ — N = Number of electrons in scattering volume V

n_{eo} = N/V = Mean electron density.

Which leads to the final equation:

$$P_s\left(\vec{k}\right)=\frac{\gamma_e^2 P_i \Omega}{A} N_e \left|\hat{s}\times\left(\hat{s}\times\hat{E}_{io}\right)\right|^2 \int_{-\infty}^{\infty} S\left(\vec{k},\omega\right)d\omega$$

$$S\left(\vec{k},\omega\right)\equiv \lim_{T\to\infty,V\to\infty}\frac{1}{TV}\left\langle\frac{\left|n_e\left(\vec{k},\omega\right)\right|^2}{n_{eo}}\right\rangle$$

Appendix B – Standard Gain Horn Radiation Pattern

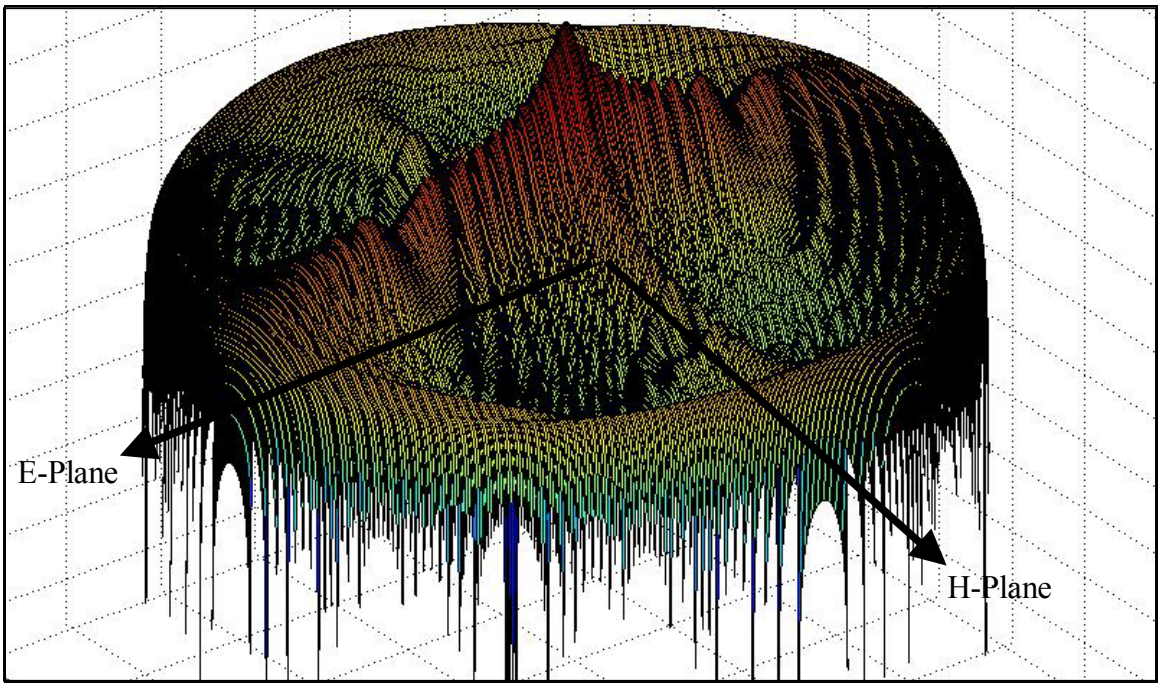

Figure B-1: Standard Gain Horn Radiation Pattern

Both axes for the above figure range from -180^{o} to 180^{o}.

The maximum gain is 27dB and the gain at the edges is approximately -40dB.

References

[1] A.L. Bezbatchenko, I.N. Golovin, P.I. Kozlov, A.S. Strelkov, and I. Yavlinsky, Plasma Physics and Problems of Controlled Fusion **1**, 116 (1955).

[2] B.B. Kadomtsev, *Tokamak Plasma: A Complex Physical System* (IOP Publishing, 1992).

[3] E. Teller, *Fusion: Magnetic Confinement* (Vol. 1, Academic Press, 1981).

[4] J.D. Lawson, Proc. Phys. Soc. **B70**, 6 (1957).

[5] U. Unterberg, S. Ulrich, *Overview of Tokamak Results* (JET Documents).

[6] JET (Joint European Torus) webpage: *http://www.jet.efda.org*

[7] JT-60U (Japanese Tokamak Upgrade) webpage: *http://www-jt60.naka.jaeri.go.jp*

[8] JET Team, Nucl. Fusion **32**, 187 (1992).

[9] P.R. Thomas *et al*., Phys. Rev. Let. **80**, 5548 (1998).

[10] JT-60U Experimental Report No. 46 (August 7, 1998).

[11] ITER Organization: *www.iter.org*

[12] J.W. Connor, and H.R. Wilson, Plasma Phys. Control. Fusion **36**, 719 (1994).

[13] C.M. Greenfield, D.P. Schissel, B.W Stallard *et al.*, Phys. Plasmas **4**, 1596 (1997).

[14] A. Hirose, D.Z. Liu, and S. Livingstone, Can. J. Phys. **82**, 167 (2004).

[15] A. Hirose, Phys. Rev. Lett. **92**, 2 (2004).

[16] R.E. Slusher, C.M. Surko, Phys. Fluids **23**, 3 (1980).

[17] M.G. Shats *et al*., Phys. Plasmas **2**, No. 2 (1995).

[18] A.J.H. Donne, C.J. Barth, B. Groot, N.J. Cardozo, H. Kluiver, G.J.J. Remkes, M. Emaami, A. Hirose, O. Mitarai, A. Sarkissian, H.M. Skarsgard, S.W Wolfe, and W. Zhang, Plasma Phys. and Control. Nucl. Fusion Research **1**, 323 (1988).

[19] W. Zhang, C. Xiao, G.G Conway, O. Mitarai, A. Sarkissian, H.M. Skarsgard, L. Zhang, and A. Hirose, Phys. Fluids B **4**, 3277 (1992).

[20] O. Mitarai, H.H. Skarsgard, and A. Hirose, Fusion Tech **20**, 285 (1991).

[21] W. Zhang, C. Xiao, and A. Hirose, Phys. Fluids **B 5**, 3961 (1993).

[22] A.K. Singh, R. Kaur, S.K. Matto, and A. Hirose, Phys. of Plasmas **11**, 23 (2004).

[23] D. Liu, C. Xiao, A.K. Singh, and A. Hirose, Nucl. Fusion, (accepted) (2005).

[24] L.A. Artsimovich, Nucl. Fusion **12**, 215 (1972).

[25] *Operating Instructions* (Veeco APC, PP316).

[26] I.H. Hutchinson, *Principles of Plasma Diagnostics* (2nd Ed, Cambridge University Press, 2002).

[27] F.F. Chen, *Introduction to Plasma Physics and Controlled Fusion* (2nd Ed, Plenum Press, 1984).

[28] J. Wesson, *Tokamaks* (3rd Ed, Clarendon Press, 2004).

[29] M. Emaami, O. Mitarai, and S.W. Wolfe, *Electron Density Measurements of Normal and AC Discharges in the STOR-1M Tokamak* (PPL-86, 1986)

[30] *Operating Instructions* (ELVA-1, PP328)

[31] G. Wentzel, Zeits. f. Phys. **38**, 518 (1926), H.A. Kramers, Zeits. f. Phys. **39**, 828 (1926), and L. Brillouin, Comptes Rendus **183**, 24 (1926).

[32] D.J. Griffiths, *Introduction to Electrodynamics* (3rd ed, Prentice-Hall Inc., 1999).

[33] D.M. Pozar, *Microwave Engineering* (2nd ed, John Wiley & Sons Inc., 1998).

[34] J.D. Jackson, *Classical Electrodynamics* (1st ed, John Wiley & Sons Inc., 1962).

[35] ASTM Standard B617, *Standard Specification for Coin Silver Electrical Contact Alloy* (2005)

[36] M. Mase, T. Yamamoto, T. Tsukishima, Jap. J. of App. Phys. **13**, 8 (1974).

[37] J. Sheffield, *Plasma Scattering of Electromagnetic Radiation* (Academic Press, 1975).

[38] F.F. Chen, *Introduction to Plasma Physics and Controlled Fusion* (1st ed, Plenum Press, 1974).

[39] K. Miyamoto, *Fundamentals of Plasma Physics and Controlled Fusion* (Iwanami Book Service Center, 1997).

[40] K.H. Burrell, Phys. Plasmas **41**, 1418 (1996).

[41] F. Wagner, Phys. Rev. Lett. **49**, 1407 (1982).

[42] A. Hirose, *Drift Instabilities in Magnetically Confined Plasmas: A Brief Overview* (Autumn College on Plasma Physics, Trieste Italy, 2005).

[43] A. Hirose, *Plasma Waves II Lecture Notes* (University of Saskatchewan, 2005).

[44] W.M. Tang, Nucl. Fusion **18**, 1089 (1978).

[45] A. Hirose, *Plasma Waves II Course Notes* (University of Saskatchewan, 2004).

[46] W. Horton, Rev. of Modern Phys. **71**, 3 (1999).

[47] M. Mazzucato, Phys. Rev. Lett. **48**, 1828 (1982).

[48] D.R. Smith *et al.*, Rev. Sci. Instrum. **75**, 3840 (2004).

[49] J.Q. Dong, H. Sanuki, K. Itoh, L. Chen, Phys. Plasmas **9**, 4699 (2002).

[50] *Operating Instructions* (Varian VKT2427N1 EIO Klystron, PPL315/1, 1990).

[51] B. Steer, *Klystron and EIK Theory* (Communications and Power Industries Presentation, 2003).

[52] *Operating Instructions* (Varian VPW2889E5 Power Supply, PPL315, 1990).

[53] Millitech, GOA-08-STP-03SP A3722 Calibration data (1990).

[54] C.A. Balanis, *Antenna Theory, Analysis and Design* (2nd ed, John Wiley & Sons Inc., 1997).

[55] O.P. Ghandi, *Microwave Engineering and Applications* (Pergamon Press, 1981).

[56] Alpha Industries, *Millimeter Wave Components & Subsystems* (Alpha Industries, 1987)

[57] P. Hariharan, *Basics of Interferometry* (Academic Press, 1992)

[58] Private correspondence with Alfred Hislop of Pacific Millimeter and Janet Stewart of Millitech (2004).

[59] A.K. Singh, J. Morelli, T. Asai, and A. Hirose, Phys. Plasmas **10**, 3451 (2003).

[60] M. Sayer, and A. Mansingh, *Measurement, Instrumentation and Experiment Design in Physics and Engineering* (Prentice Hall of India, 2000).

[61] *Operating Instructions* (LeCroy 9314M, PPL321).

[62] N. Storey, *Electronics A Systems Approach* (2nd Ed, Prentice Hall, 1998).

[63] National Semiconductor, LF155/LF156/LF256/LF257/LF355/LF356/LF357 JFET Input Operational Amplifiers: *http://www.national.com/pf/LF/LF356.html*

[64] P.D. Welch, *The Use of Fast Fourier Transform for the Estimation of Power Spectra: A Method Based on Time Averaging Over Short, Modified Periodgrams* (IEEE Transactions on Audio Electroacoustics, Volume AU-15, pages 70-73, June 1967).

[65] A.V. Gelder, *Efficient Computation of Polygon Area and Polyhedron Volume* (Graphic Gems V, 1995).

[66] M.L. Boas, *Mathematical Methods in the Physical Sciences* (2nd Ed, John Wiley & Sons, 1983).

[67] C.M. Surko, and R.E. Slusher, Phys. Rev. Lett. **37**, 1747 (1976).

[68] P. Devynck *et al*., Plasma Phys. Control. Fusion. **35**, 63 (1993).

[69] P.C. Liewer, Nucl. Fusion **25**, 5 (1985).

[70] C.M. Surko, and R.E. Slusher, Science **221**, N4613, p817 (1983).

[71] R.E. Slusher, and C.M. Surko, Phys. Fluids **28**, 9 (1985).

[72] D.L. Brower, W.A. Peebles, and G.A. Luhmann, Nucl. Fusion **27**, 12 (1987).

[73] T. Crowley, and E. Mazzucato, Nucl. Fusion **25**, 507 (1985).

[74] P.R. Bevington, and D.K. Robinson, *Data Reduction and Error Analysis for the Physical Sciences* (2nd Ed, McGraw-Hill, 1992).

[75] W.A. Peebles, T. Rhodes, (private correspondence, 2004).